FINITE ELEMENT FRACTURE ANALYSIS OF STEEL-CONCRETE BOND

By

Christian J. Brown

David Darwin

Steven L. McCabe

A Report on Research Sponsored by

THE CIVIL ENGINEERING RESEARCH FOUNDATION
Contract No. 91-N6002

THE NATIONAL SCIENCE FOUNDATION
Research Grant No. MSS-9021066

THE REINFORCED CONCRETE RESEARCH COUNCIL
Project 56

Structural Engineering and Engineering Materials
SM Report No. 36

UNIVERSITY OF KANSAS CENTER FOR RESEARCH, INC.
LAWRENCE, KANSAS
November 1993

LEGAL NOTICE

This report was prepared by the University of Kansas Center for Research, Inc. as an account of work sponsored by the Civil Engineering Research Foundation (CERF). Neither CERF, nor any persons acting on behalf of either:

a. Makes any warranty or representation, express or implied, with respect to the accuracy, completeness, or usefulness of the information contained in this report, or that the use of any apparatus, method, or process disclosed in this report may not infringe third party rights; or

b. Assumes any liability with respect to the use of, or for damages resulting from the use of, any information, apparatus, method, or process disclosed in this report.

c. Makes any endorsement, recommendation or preference of specific commercial products, commodities or services which may be referenced in this report.

Any opinions, findings, and conclusions or recommendations expressed in this material are those of the authors and do not necessarily reflect the views of the National Science Foundation.

FINITE ELEMENT FRACTURE ANALYSIS OF STEEL-CONCRETE BOND

ABSTRACT

The effect of deformation pattern on bond strength is studied using a finite element model of a beam-end specimen. The model includes concrete, steel, and transverse reinforcement substructures. A splitting crack is assumed to occur along the specimen center line, and only one-half of the specimen is modeled. Splitting concrete is modeled using the nonlinear fracture mechanics approach known as the "fictitious crack model" (Hillerborg et al. 1976). The steel-concrete interface is modeled using special link elements that follow a Mohr-Coulomb failure law. Bond strength is studied as a function of rib height, rib shape, concrete cover, lead length, embedded length, and transverse reinforcement. A 1 in. square bar with ribs heights of 0.06 in. or 0.09 in. is used. Models with 1, 2, and 3 in. covers and one-half in. and 2 in. lead lengths are studied. Embedded lengths range from 0.82 to 7.86 in.

The study shows that steel-concrete interaction can be accurately represented by placing interface elements only on the compression faces of the ribs. Under conditions of low cover and no transverse reinforcement, bond force is not dependent on rib height or rib shape; however, an increase in rib height produces an increase in the initial stiffness of the load-slip curves. Under conditions of increased concrete cover, bond force and the initial stiffness of the load-slip curves increase. Under conditions of increased bar confinement provided by additional lead length, bond strengths increase compared to bars with lower lead lengths. Bond force increases with an increase in embedded length. However, the amount of concrete that is split at failure is not proportional to the embedded length. The degree of splitting (lateral displacement at the front face of the specimen) up to the peak load is not dependent on rib height or shape but is dependent on concrete cover. Lateral displacements after the peak load increase with an increase in rib height. Under conditions of increased confinement provided by transverse reinforcement, bond strength increases compared to models without transverse reinforcement. A statical model of steel in contact with concrete provides a means of relating the clamping force provided by the concrete to the pull-out force of the reinforcing bar.

ACKNOWLEDGEMENTS

This report is based on a graduate project submitted by Christian J. Brown to the Department of Civil Engineering of the University of Kansas in partial fulfillment of the requirements for the M.S.C.E. degree.

Funding for this research was provided by the Civil Engineering Research Foundation under CERF Contract No. 91-N6002, the National Science Foundation under NSF Grant No. MSS-9021066, and the Reinforced Concrete Research Council under RCRC Project 56. Support was also provided by ABC Coating Company, Inc., Birmingham Steel Corporation, Chaparall Steel Company, Fletcher Coating Company, Florida Steel Corporation, Morton Powder Coatings, Inc., North Star Steel Company, and 3M Corporation.

TABLE OF CONTENTS

ABSTRACT i

ACKNOWLEDGEMENTS ii

LIST OF TABLES v

LIST OF FIGURES vi

CHAPTER 1 INTRODUCTION 1

1.1 General 1

1.2 Background 2

1.3 Fracture Mechanics and Bond 3

1.4 Finite Element Bond Analyses 4

1.5 Object and Scope 6

CHAPTER 2 FINITE ELEMENT MODEL 8

2.1 Introduction 8

2.2 Fracture Mechanics Model 8

2.3 Concrete-Steel Interface Representation 10

2.4 Concrete Substructure 14

2.5 Steel Substructure 15

2.6 Transverse Reinforcement 16

2.7 Boundary Conditions 16

2.8 Solution Procedure 17

CHAPTER 3 NUMERICAL RESULTS 19

3.1 Introduction 19

3.2 Load-Slip Response 20

3.3 Effect of Placing Interface Elements only on Compression Faces of Ribs 23

3.4 Effect of Rib Height 24

TABLE OF CONTENTS (continued)

3.5 Effect of Rib Shape 25

3.6 Effect of Concrete Cover 25

3.7 Effect of Lead Length 27

3.8 Effect of Embedded Length 28

3.9 Lateral Displacements 30

3.11 Effect of Transverse Reinforcement 32

3.10 Statical Model 33

CHAPTER 4 CONCLUSIONS 35

4.1 Summary 35

4.2 Observations and Conclusions 36

4.3 Recommendations for Future Study 37

REFERENCES 39

TABLES 44

FIGURES 49

LIST OF TABLES

Table No.		Page
2.1	Finite Element Model Sizes--1/2 in. Lead Lengths	44
2.2	Finite Element Model Sizes--Stepped Rib Face	45
2.3	Finite Element Model Sizes--2 in. Lead Lengths	46
3.1	Bond Force (Peak Load) and Corresponding Values of Loaded End Slip for the Finite Element Models in this study	47
3.2	Lateral Displacements at the Front Face of the Model Coinciding with the Peak Load for Finite Element Models in this study	48

LIST OF FIGURES

Figure No.		
1.1	Mode I Crack (after Barsom and Rolfe 1987)	49
2.1	Overall Finite Element Model (Model with 3 ribs and 1/2 in. Lead Length)	50
2.2	Portion of Experimental Beam-end Specimen Represented by Finite Element Model	51
2.3	Beam-end Specimen at Failure (Darwin and Graham 1993)	51
2.4	(a) Crack Opening Stress-displacement Relationship (Petersson 1979) (b) Straightline Approximation of Crack Opening Stress-displacement Relationship (Petersson 1979)	52
2.5	Crack Rod and Stirrup Element (after Lopez et al. 1992)	53
2.6	Connection of Crack Rods to Concrete Substructure (End View)	53
2.7	Stress-Strain Function for Crack Rod Elements	54
2.8	Three-dimensional Mohr-Coulomb Failure Surface (after Lopez et al. 1992)	55
2.9	Three-dimensional Link Element (after Lopez et al. 1992)	55
2.10	Normal Directions for Interface Link Elements	56
2.11	Schematic of Interface Element Material States (after Desai and Nagaraj 1988)	57
2.12	Interface Element Material States on Mohr-Coulomb Surface	58
2.13	Three-dimensional, 8-node, Linear, Isoparametric Brick Element (after Lopez et al. 1992)	58
2.14	Concrete Substructure (Model with 3 ribs, 1/2 in. Lead Length, and 2 in. Cover)	59

LIST OF FIGURES (continued)

Figure No.		
2.15	Dimensions of Deformation Patterns Analyzed (Plan View) (a) Rib Height = 0.06 in. (b) Rib Height = 0.09 in. (c) Multi-Angle Rib Face (d) Detail of Rib Height of 0.06 in. and 0.09 in. (e) Detail of Multi-Angle Rib Face	60
2.16	Reinforcing Steel Substructure (Model with 3 ribs and 1/2 in. Lead Length)	61
2.17	Location of Compressive Reaction on Experimental Beam-end Specimen	62
2.18	Boundary Conditions on Finite Element Models	63
2.19	Schematic of Secant Stiffness of Crack Rod Elements	64
2.20	Schematic of Stress Correction Back to Slip Surface (after Lopez et al. 1992)	65
3.1	Progressive Change of Interface Element Material State (Model with 6 ribs, 1/2 in. Lead Length, and 2 in. Cover)	66
3.2	Movement of Interface from Initial to Peak Load for Model with 6 ribs, 1/2 in. Lead Length, and 2 in. Cover (after Choi et al. 1990)	67
3.3	Bond Force-Loaded End Slip Curve for Model with 6 ribs, 1/2 in. Lead Length, and 2 in. Cover	68
3.4	Bond Force-Loaded End Slip and Bond Force-Unloaded End Slip Curves	69
3.5	Displacements Along Length of Bar from Initial to Peak Loading for 6 Rib Model (Embedded Length = 5.42 in.)	70
3.6	Stresses on Interface Element Closest to Imposed Displacement for Model with 6 ribs, 1/2 in. Lead Length, and 2 in. Cover	71
3.7	Bond Force-Loaded End Slip Curves for Models with Interface Elements on Compression Face of Rib and Interface Elements on Entire Rib Surface	72

LIST OF FIGURES (continued)

Figure No.		
3.8	Bond Force-Loaded End Slip Curves for Models with 1 in. Cover and Rib Heights of 0.06 in. and 0.09 in. (1/2 in. Lead Length).....	73
3.9	Bond Force-Loaded End Slip Curves for Models with 2 in. Cover and Rib Heights of 0.06 in. and 0.09 in. (1/2 in. Lead Length).....	74
3.10	Bond Force-Loaded End Slip Curves for Models with 3 in. Cover and Rib Heights of 0.06 in. and 0.09 in. (1/2 in. Lead Length).....	75
3.11	Bond Force-Loaded End Slip Curves for Models with 45° Ribs and Multi-angle Ribs (Rib Height = 0.06 in., 1 in. Cover, 1/2 in. Lead Length).....	76
3.12	Bond Force-Loaded End Slip Curves for Models with 45° Ribs and Multi-angle Ribs (Rib Height = 0.06 in., 2 in. Cover, 1/2 in. Lead Length).....	77
3.13	Bond Force-Loaded End Slip Curves for Models with 45° Ribs and Multi-angle Ribs (Rib Height = 0.06 in., 3 in. Cover, 1/2 in. Lead Length).....	78
3.14	Bond Force versus Cover for Models with 45° Ribs and Multi-angle Ribs (Rib Height = 0.06 in., 1/2 in. Lead Length).....	79
3.15	Bond Force versus Embedded Length for Models with 45° Ribs and Multi-angle Ribs (Rib Height = 0.06 in., 1/2 in. Lead Length).....	80
3.16	Bond Force-Loaded End Slip Curves for Models with 1, 2, and 3 in. Covers (45° Rib, Rib Height = 0.06 in., 1/2 in. Lead Length).....	81
3.17	Bond Force-Loaded End Slip Curves for Models with 1, 2, and 3 in. Covers (45° Rib, Rib Height = 0.09 in., 1/2 in. Lead Length).....	82
3.18	Bond Force-Loaded End Slip Curves for Models with 1, 2, and 3 in. Covers (Multi-Angle Rib Faces, 1/2 in. Lead Length).....	83
3.19	Bond Force versus Cover (1/2 in. Lead Length, Rib Heights = 0.06 in. and 0.09 in.).....	84

LIST OF FIGURES (continued)

Figure No.

3.20 Bond Force-Unloaded End Slip Curves for Models with 1, 2, and 3 in. Covers (45° Rib, Rib Height = 0.06 in., 1/2 in. Lead Length)..... 85

3.21 Bond Force-Unloaded End Slip Curves for Models with 1, 2, and 3 in. Covers (Multi-Angle Rib Faces, 1/2 in. Lead Length)..... 86

3.22 Bond Force-Loaded End Slip Curves for Models with 1/2 in. and 2 in. Lead Lengths (45° Ribs, Rib Height = 0.06 in., 2 in. Cover)..... 87

3.23 Bond Force versus Embedded Length Curves for Models with 1/2 in. and 2 in. Lead Lengths (45° Ribs, Rib Height = 0.06 in., 2 in. Cover)..... 88

3.24 Bond Force-Loaded End Slip Curves for Models with 2 in. Lead Lengths (45° Ribs, 2 in. cover)..... 89

3.25 Bond Force versus Embedment Length (45° Ribs, Rib Height = 0.06 in., 1/2 in. Lead Length)..... 90

3.26 Bond Force versus Embedment Length (45° Ribs, Rib Height = 0.09 in., 1/2 in. Lead Length)..... 91

3.27 Bond Force versus $l_d(C + 0.5d_b)$ for Models with 1/2 in. Lead Lengths (45° Ribs, Rib Height = 0.06 in.)..... 92

3.28 Bond Force versus $l_d(C + 0.05d_b)$ for Models with 6 and 12 ribs (1/2 in. Lead Length, 45° Ribs, Rib Height = 0.06 in,)..... 93

3.29 Amount of Split Concrete for Models with 1, 3, 6, and 12 ribs (Lead Length = 1/2 in., Rib Height = 0.06 in., Cover = 2.0 in.)..... 94

3.30 Bond Force-Lateral Displacement Curves at Locations Along Length of Specimen for Model with 6 ribs, 2 in. cover, 1/2 in. lead length, 0.09 in. rib height (y is measured from front face of specimen)..... 95

3.31 Bond Force-Lateral Displacement Curves for 6 Rib Models with 1, 2, and 3 in. Covers (45° Ribs, Rib Height = 0.06 in., 1/2 in. Lead Length)..... 96

3.32 Bond Force-Lateral Displacement Curves for Models with Rib Heights of 0.06 in. and 0.09 in. (6 ribs, 2 in. Cover)..... 97

LIST OF FIGURES (continued)

Figure No.		
3.33	Bond Force-Lateral Displacement Curves for Models with Multi-Angle Rib Faces and 45° Angle Rib Faces (2 ribs, 3 in. Cover).....	98
3.35	Bond Force-Loaded End Slip Curves for 2 Rib Models With and Without Transverse Reinforcement (45° Ribs, Heights of 0.06 in. and 0.09 in., 2 in. Cover, 1/2 in. Lead Length).....	99
3.34	Statical Model (after Choi et al. 1990).....	100

CHAPTER 1

INTRODUCTION

1.1 General

When loaded in tension, concrete exhibits brittle failure, yet its resistance to fracture is generally not considered in design. Rather, concrete members require the addition of tensile reinforcement, usually in the form of deformed steel bars. To resist the tensile forces, the bond between the steel and the concrete must be sufficiently strong to develop the bar. Traditionally, reinforced concrete design is based on the assumption that the strain in the concrete and the steel are the same at sections under the maximum load. Good bond between the steel and the concrete is required to ensure that the assumption of strain compatibility is reasonably accurate (however, relative displacements do occur between the steel and the surrounding concrete). Of even more importance, a loss in bond may lead to a premature failure of the member.

Ultimately, the ability of a deformed bar to bond with the surrounding concrete dictates its anchorage or development length. An increase in the length used to develop the design stresses in a bar reduces the economy of the design. However, if too little bar length is used, the safety of the structure will be inadequate. As a result, an understanding of the factors that control bond is needed to accurately determine the appropriate bar length needed to obtain the full capacity of the member.

Considerable experimental and analytical research has been conducted on the bond between deformed reinforcing bars and concrete. It is generally believed that many variables, including the concrete cover, concrete strength, steel bar deformation pattern, and the use of transverse reinforcement affect the bond performance of deformed bars (Menzel 1939; Clark 1946, 1949; Jimenez et al. 1978; Choi et al. 1990, 1991; Hadje-Ghaffari et al. 1991; Darwin et al. 1992a, 1992b; Kimura and Jirsa 1992; Darwin and Graham 1993, to name a few). A rational (i.e., nonempirical) procedure that combines these variables has yet to be developed.

Research underway at the University of Kansas (Darwin et al. 1992a, 1992b; Darwin and

Graham 1993) is aimed at improving the development characteristics of reinforcing bars. The program centers on studying the effect of reinforcing bar deformation pattern on the bond of reinforcing steel to concrete. The results of this program will help develop guidelines to improve the development characteristics of reinforcing bars used in design. The overall program involves the use of both experimental and analytical techniques to evaluate and improve the bond performance of bars with various deformation patterns. This report describes the application of finite element analyses in the study to determine how reinforcing steel deformation geometry effects the bond to concrete.

1.2 Background

Reinforcing bars with deformations have not always been used in concrete construction. Prior to the use of deformed bars, smooth steel bars with hooked ends were used to develop the steel; the hooks were needed to provide adequate bond. With the introduction of deformed bars, the need for end-hooks was reduced. Abrams (1913) was one of the first to study the bond strength of both smooth and deformed bars. From his tests, Abrams concluded that higher bond strengths can be obtained with deformed bars than with smooth bars.

Menzel (1939) used pull-out tests to study the bond performance of bars with longitudinal and transverse ribs as a function of embedded length, concrete cover, type of bar surface, and the position of the bar during concrete placement. He concluded that bars with transverse ribs provide greater bond strengths than bars with longitudinal ribs. These results indicate that transverse ribs provide a bearing area at the bar-concrete interface to limit the amount of steel bar slip in the direction of an applied load.

Many of the deformation patterns in use today were studied by Clark (1946, 1949). Clark examined the bond behavior of 17 deformation patterns as a function of the position of the bar during concrete placement, bar size, concrete strength, and bonded length. Using pull-out specimens and beams, Clark found that top-cast bars, because of their exposure to excess bleed water during concrete placement, develop less bond strength than bottom-cast bars. He also

showed that the ratio of the shearing area (the area of the bar-concrete interface measured between the ribs along the bar axis) to the rib bearing area (measured as the projected area of the ribs) is an important parameter in providing slip resistance, and suggested that ratios not greater than 10 be used. Based on his findings, Clark also made recommendations for rib spacing and height, and the current specifications for bar geometry found in ASTM A 615 reflect his studies, although his recommendation on the ratio of shearing area to bearing area has not been adopted.

Lutz, Gergely, and Winter (1966) and Lutz (1970) studied the fundamental mechanisms in which a deformed bar bonds to concrete and concluded that chemical adhesion, friction, and mechanical interaction all contribute to bond. Chemical adhesion is produced by the cement paste in concrete being closely attached to the steel. At low levels of relative displacement between steel and concrete, adhesion breaks down and no longer contributes to the bond. Once adhesion is lost, friction and mechanical interaction between the bar and the concrete act together to resist any relative movement. Friction is produced as the steel in contact with the concrete slides. The mechanical interaction is mostly influenced by the geometry of the ribs (deformations) on the bar. It is generally believed that mechanical interaction of a deformed bar with the surrounding concrete is the primary contributor to bond (Menzel 1939; Lutz et al. 1966; Lutz and Gergely 1967). However, studies by Rehm (1957, 1961); Ferguson and Thompson (1965); Lutz, Gergely, and Winter (1966, 1967); Wilhelm, Kemp, and Lee (1971); Skorobogatov and Edwards (1979); Losberg and Olsson (1979); Soretz and Holzenbein (1979); and Kimura and Jirsa (1992) offer conflicting opinions of how mechanical interlock is influenced by the rib spacing and height found on a deformed reinforcing bar.

1.3 Fracture Mechanics and Bond

Lutz et al. (1966, 1967), studied the ways in which a deformed steel bar slips in concrete, leading to loss of bond (bond-slip). According to these studies, two failure modes are possible when a reinforcing steel bar moves relative to the surrounding concrete. Bond failure can either result when the ribs push the concrete away from the bar through a wedging action as the bar

moves through the concrete, producing a concrete splitting failure, or the concrete is crushed in front of the ribs as the bar moves relative to the concrete, causing a "pull-out" failure. Other studies of steel-concrete bond have revealed that, in typical structural members, a loss of bond results from a concrete splitting failure (Clark 1949; Menzel 1952; Chinn et al. 1955; Ferguson and Thompson 1962; Rehm 1957, 1961; Goto 1971; Losberg and Olsson 1979; Johnston and Zia 1982; Treece and Jirsa 1989; Choi et al. 1990, 1991; Hadje-Ghaffari et al. 1991; and Darwin and Graham 1993). Because of the splitting nature of a bond failure, fracture mechanics can be used to study the problem of splitting concrete leading to a loss of bond in reinforced concrete members (Rots 1989).

Research by Saouma (1980), Ingraffea et al. (1984), Bazant and Sener (1988), Rots (1988, 1989), Gylltoft (1989), Mazars et al. (1989), and Gerstle and Xie (1992) studied bond by using fracture mechanics to model splitting concrete. The majority of these analyses used the principles of fracture mechanics to model splitting concrete through secondary cracking, with no representation of longitudinal cracking. In their experimental study relating splitting concrete to bond-slip, Kemp and Wilhelm (1979) showed that a loss in bond is the direct result of longitudinal splitting, and suggested that longitudinal cracks must be considered to accurately address the problem of bond-slip.

The work in the current study involves modeling the longitudinal cracking that occurs in actual flexural members leading to a loss of bond (Choi et al. 1990, 1991; Hadje-Ghaffari et a. 1991; Darwin and Graham 1993). Splitting concrete is represented using fracture mechanics in conjunction with the finite element method (Hillerborg et al. 1976) to study bond behavior and explain aspects of the experimental research underway at the University of Kansas (Darwin and Graham 1993).

1.4 Finite Element Bond Analyses

A number of previous studies have used the finite element method to address bond behavior. In these studies, a variety of methods are used to study bond and steel bar slip.

Ingraffea et al. (1984) investigated bond behavior of tension-pull specimens by applying nonlinear, mixed-mode fracture mechanics with the finite element method. These finite element models took into account the effects of both tension and shear softening in the fracture process zone. Gylltoft (1989) applied fracture mechanics in a finite element model to study bond failure in pull-out tests. Gylltoft's models studied bond between a smooth bar and concrete while including constitutive relations for the fracture process zone in both the shear and normal directions. Mazars et al. (1989) applied contiuous damage mechanics in a finite element model to study the steel-concrete bond mechanism. Mazars et al. address the strain-softening response of concrete due to contiuous cracking and its effects on the steel-concrete interface. Rots (1989) analyzed bond-slip in a finite element model using a smeared crack approach. The individual contributions to bond-slip in the models were studied in detail to consider cracking, crushing, and softening of the concrete. Gerstle and Xie (1992) studied discrete cracking in tension pull models through the application of a fictiticious crack method (Hillerborg 1976).

Bond and bond-slip behavior are difficult to study analytically because of the nonlinear, inelastic behavior of splitting concrete and steel bar slip. Keuser and Melhorn (1987) concluded that the behavior of finite element models of bond are influenced mainly by the properties of the steel-concrete interface elements, the density of the finite element mesh, and assumed bond stress-slip relations. They concluded that detailed finite element studies of bond cannot be undertaken without special consideration given to transverse pressure, secondary cracks in the concrete, and the deterioration of bond near primary cracks.

Choi et at. (1990, 1991) studied the bond of reinforcing steel to concrete using a three-dimensional finite element model of a beam-end specimen. Beam-end specimens have been used in a number of studies at the University of Kansas as the principle technique to experimentally measure bond strength (Brettman et al. 1984, 1986; Choi et al. 1990, 1991; Hadje-Ghaffari et al. 1991; Darwin and Graham 1993). These specimens are designed to simulate the stress conditions that occur in actual flexural members, where both the reinforcing steel and adjacent concrete are placed in tension. In tests conducted using beam-end specimens, a concrete splitting failure

results from the wedging action produced by the bar as it is pulled out. Prior finite element studies of steel-concrete bond at the University of Kansas (Choi et al. 1990, 1991; Hadje-Ghaffari et al. 1991) have used models of the beam-end specimens to explain observed bond behavior.

The models used by Choi et al. (1990, 1991) represent an experimental beam-end specimen consisting of concrete and reinforcing steel substructures. A nonlinear fracture mechanics method is used to represent splitting concrete and special link elements are employed to model the interface between the steel and concrete. To determine the bond force of a particular model, Choi et al. (1990, 1991) used a two-step process. In the first step, a three-dimensional representation of concrete that splits along a predefined crack surface is used to determine the clamping force of the concrete on the steel as a function of lateral (splitting) displacement. In the second step, the results of the first step are used with interface link elements to model slipping of the bar. The models used by Choi et al. (1990, 1991) were later refined by Hadje-Ghaffari et al. (1991). These refinements included analyses of models with different bar sizes as well as improvements in the boundary conditions to better match those in the experimental specimens.

1.5 Object and Scope

The finite element models used in this study are based on the analytical models first developed by Choi et al. (1990) to study bond. In the current study, single three-dimensional finite element models of the beam-end specimen is used. Unlike the previous work at the University of Kansas (Choi et al. 1991; Hadje-Ghaffari et al. 1991), both concrete splitting and steel bar slip are represented in the same model. The model includes concrete and steel substructures, along with representations for the crack plane and the interface between the concrete and the reinforcing steel. Several models also contain elements representing transverse reinforcement (stirrups). The concrete and steel are modeled using three-dimensional, linear isoparametric brick elements. Assuming a Mode I crack in the specimen (Fig. 1.1), splitting of the concrete is modeled using the nonlinear fracture mechanics approach developed by Hillerborg et

al. (1976), known as the fictitious crack model. To model the interface, link elements that follow a Mohr-Coulomb failure law are used to connect the reinforcing steel substructure to the concrete substructure.

Analyses are carried out using finite element models to evaluate steel-concrete bond performance. Bond behavior is analyzed by displacing the reinforcing steel substructure with respect to the concrete substructure. The load-slip response of the models is obtained by imposing small displacements on the nodes at the front end of the reinforcing steel substructure. The analytical study addresses the effects of deformation height and face angle, concrete cover, lead length (the distance from the front of the specimen to the first rib), embedded length (the length of the bonded region measured from the front of the specimen), and confinement provided by stirrups on bond performance.

The initial goal of the analysis is to study the behavior of the three-dimensional model and assess its ability to match the behavior of the beam-end specimens. This goal is accomplished by incorporating the key aspects of beam-end specimen behavior using as simple a representation as possible. The ultimate goal of the study is to determine the role that deformation geometry plays in steel-concrete bond.

CHAPTER 2

FINITE ELEMENT MODEL

2.1 Introduction

The finite element model used in the study was selected to represent, in a relatively simple fashion, the key elements of concrete-steel bond interaction. The model represents one-half of a reinforced concrete beam-end specimen with a 1 in. square reinforcing bar. The square bar simplified the modeling while providing a good representation of bar-concrete interaction (see Sections 2.5 and 3.8). The overall finite element model is shown in Fig. 2.1. The specimen height ranges from 7 in. to 9 in.: 5 in. of concrete below the bar, 1 in. of concrete for the bar depth, and 1 to 3 in. of concrete (cover) above the bar. The length of the model is 12 in., representing one-half of the length of a beam-end specimen used in experimental analysis (Choi et al. 1990, 1991; Hadje-Ghaffari et al. 1991; Darwin and Graham 1993). Ribs on the bar are placed in contact with the concrete along the surface parallel to the yz-plane (Fig. 2.1). Based on symmetry, only one-half of the 9 in. wide specimen is represented (Fig. 2.2). The plane of symmetry corresponds to the surface on which the failure crack forms. The model dimensions remain constant as the embedded length is increased.

The concrete and steel finite element substructures are generated using the PATRAN-II software system, version 2.4 (1990). To optimize the solution procedure, nodal and element renumbering is also performed by PATRAN-II to minimize the band width, using the minimum wave front criteria method (Gibbs, Poole, and Stockmeyer 1976). The models are analyzed using the POLO-FINITE general purpose finite element analysis software system (Lopez et al. 1992). The number of nodes and elements for the models used in the analyses is summarized in Tables 2.1-2.3. The specific aspects of the finite element model are discussed in the following sections.

2.2 Fracture Mechanics Model

Failure of beam-end specimens is characterized by a dominant fracture surface that runs

longitudinally, above and below the test bar (Fig. 2.3). The fracture results from the formation of a Mode I crack, where the fracture surfaces are displaced symmetrically perpendicular to one another in opposite directions (Barsom and Rolfe 1987). Because of the nature of this splitting behavior, failure can be modeled using fracture mechanics concepts. A nonlinear fracture mechanics approach (as opposed to linear elastic fracture mechanics) is used because the nonlinear region at the tip of the crack, known as the fracture process zone (FPZ), is relatively large in relation to the size of the structure (ACI 446 1989).

Hillerborg et al. (1976) developed the "fictitious crack model" to represent the nonlinear fracture behavior of concrete. The model accounts for the observed response that stress continues to be transferred across a developing crack after the material's tensile strength has been reached. The transfer region is the FPZ. Using the fictitious crack model, the FPZ is defined as the region in which the strain corresponding to the tensile strength, f'_t, has been exceeded (resulting in the formation of a physical crack) but the material can carry a tensile stress. As the crack continues to open, the ability of the concrete to resist the tensile stress decreases, finally reaching zero at a crack width of w_o. Petersson (1979) represented this stress transfer ability with a stress-displacement curve, such as the two shown in Fig. 2.4. Energy is absorbed as displacements across the crack increase from 0 to w_o. The area under the stress-displacement curve represents the total energy absorbed per unit area of the crack surface, known as the fracture energy, G_c. G_c is calculated as:

$$G_c = \int_0^{w_o} \sigma \, dw \tag{2.1}$$

in which σ is tensile stress at the crack, w is the crack width, and w_o is the displacement at which the tensile stress in the concrete becomes zero. The applicability of the expression for G_c to accurately represent the fracture behavior of concrete has been firmly established on a theoretical

basis (Petersson 1981; Bazant and Oh 1983; Leibengood et al. 1984, 1986).

In this study, the fictitious crack model is used in the finite element analysis to represent the crack that forms along the center line of the beam-end specimen. In the model, the crack is predefined along the specimen center line, and only one-half of the specimen needs to be modeled. Stress across the crack, σ, is transferred using rod elements oriented perpendicular to the crack plane. The rod elements have two nodes, with each node having one degree of freedom parallel to the element (Fig. 2.5). The two nodes (one connected to the concrete and one connected to the adjacent boundary plane) are initially coincident. The node connected directly to the boundary is constrained from moving perpendicular to the splitting surface (Fig. 2.6). This keeps the tip of the crack at the specimen center line throughout the analysis. The rod elements have a unit-length and total area equal to the tributary area of the concrete elements attached to the same node.

The stress-displacement properties of the rod elements are based on Petersson's straight-line representation (Fig. 2.4b). In the analysis, this stress-crack opening displacement relationship is represented as a stress-strain curve (Fig. 2.7). The area under the curve represents one-half of the total fracture energy since the rod elements have a unit length but represent only one-half of the crack width. Prior to cracking, the rod elements are very stiff, with an elastic modulus of 400,000 ksi. Upon reaching the tensile strength of the concrete, f'_t, the stresses in the rod elements are determined based on the descending branch of the stress-strain function. The tensile strength, f'_t, is set at 0.4 ksi, corresponding to a compressive strength of about 6 ksi. The fracture energy is set at 0.57 lb/in., which translates into a total fracture energy of 1.14 lb/in. The corresponding full crack width resulting in zero stress, w_o, is 0.0057 in.

2.3 Concrete-Steel Interface Representation

In interface contact problems, forces are transferred from one body to another by normal and tangential (shear) stresses. In the finite element model of a beam-end specimen, the interface of interest is the slip surface between the concrete and the steel at the bar surface. At the surface, normal and shearing stresses act at contact points, resulting in sliding of the two materials relative

to each other. In this study, the response of the concrete-steel interface is governed by a Mohr-Coulomb failure surface, shown in Fig. 2.8. In three-dimensional stress space, the Mohr-Coulomb failure surface is a circular cone. The axis of revolution of the cone is the normal stress axis. The failure surface relates the normal stress, σ_n, to the shearing stress, σ_s, at which failure occurs at the interface:

$$|\sigma_s| = c - \sigma_n \tan\phi \tag{2.2}$$

in which c and ϕ are the cohesion (shear stress intercept) and angle of friction ($\tan\phi = \mu$ = coefficient of friction), respectively.

The contact surface between the concrete and the steel is modeled using three-dimensional interface link elements (Fig. 2.9). These link elements are springs of unit length with an effective area equal to the contact (tributary) area of the elements at each set of nodes along the interface. The contact area remains constant throughout the analysis. The link elements have one degree of freedom normal to the interface and two mutually perpendicular degrees of freedom tangent to the interface. To define the position and orientation of the elements, three nodes are required. Nodes 1 and 2 (Fig. 2.9) are attached on opposite sides of the interface and are used to describe displacements. Node number 3 is a coordinate point, not a part of the structure, used to define the orientation of the interface surface defined by the element.

While the interface material model has the ability to have a specified thickness, the links used in this study are defined as having initially coincident node points, resulting in an interface of zero thickness. As the model is loaded, the forces in the link elements are based on the relative displacements between nodes 1 and 2 (Fig. 2.9). The link elements are placed on the slip plane along the reinforcing bar in contact with the concrete (Fig. 2.10). Because the bar is square, no interaction between the steel and concrete is represented on the top or bottom of the bar. The results section of this report (Chapter 3) will show that placing interface elements only on the compressive face of the deformations accurately models the concrete-steel interface surface.

The behavior of the interface can be described by three possible modes or states relating to the Mohr-Coulomb surface. These modes include the contact/stick or no-slip state, the contact/slip state, and the separation state (Fig. 2.11). The state that the interface elements are in depends on the magnitudes of the normal and shearing stresses, c, and μ. Fig. 2.12 shows the position of the three material states with respect to the Mohr-Coulomb surface. In the contact/stick state, there is no relative movement between the steel and concrete at a point, as the shearing stress is lower than the stress on the Mohr-Coulomb surface corresponding to the current normal (compressive) stress. In the contact/slip state, there is relative movement parallel to the interface between steel and concrete, as the shearing stress corresponding to the current normal (compressive) stress exceeds the shearing stress on the Mohr-Coulomb surface. In the separation state, no force is transferred between the steel and concrete, as tension in the interface elements moves the connected materials apart.

The contact/stick mode is defined as (Lopez et al. 1992):

$$|\sigma_s| \leq c - \sigma_n \tan\phi \tag{2.3}$$

Stress conditions of

$$|\sigma_s| > c - \sigma_n \tan\phi \text{ and } \sigma_n \leq \beta \tag{2.4}$$

and

$$|\sigma_s| > c - \sigma_n \tan\phi \text{ and } \sigma_n > \beta \tag{2.5}$$

result in a change of interface element material state to the contact/slip or separation mode, respectively. β is a small tensile stress used to insure that Eq. 2.5 is selected only when tension exists at the interface. $\beta = 0.01$ ksi in this study. In all cases,

$$|\sigma_s| = (\sigma_{sy}^2 + \sigma_{sz}^2)^{1/2} \tag{2.6}$$

in which σ_{sy} and σ_{sz} are the mutually perpendicular shearing stresses in local coordinates, and the local x-axis is normal to the interface (Figs. 2.9 and 2.10). While in the stick state, the interface properties, c and $\mu=\tan\phi$, represent adhesion and friction between the concrete and steel surfaces. In the slip state, the value for cohesion, c, is set equal to zero (representing the loss of adhesion with slip), causing the intercept of the slip surface to collapse to the origin. The contact area in the slip state contains only frictional forces, and stresses in the interface elements are corrected to the new slip surface. In the separation state, all interface element stresses are zero.

A constitutive matrix for the interface elements is defined for each of the three material states. In this study, it is assumed that shearing strains do not effect the volume of the interface elements because of the relatively smooth surface between the steel and the concrete. Therefore, the normal and tangential components of the interface deformation are uncoupled. The stiffness matrices for the contact/stick, contact/slip, and separation state are defined as (Lopez et al. 1992):

Contact/stick

$$K_{stick}=\begin{bmatrix} k_n & 0 & 0 \\ 0 & k_{sy} & 0 \\ 0 & 0 & k_{sz} \end{bmatrix} \tag{2.7}$$

Contact/slip

$$K_{slip}=\begin{bmatrix} k_n & 0 & 0 \\ 0 & \mu k_{sy} & 0 \\ 0 & 0 & \mu k_{sz} \end{bmatrix} \tag{2.8}$$

Separation

$$K_{sep}=\begin{bmatrix} \alpha k_n & 0 & 0 \\ 0 & \alpha k_{sy} & 0 \\ 0 & 0 & \alpha k_{sz} \end{bmatrix} \quad (2.9)$$

in which k_n and k_s ($= k_{sy} = k_{sz}$), set at 40000 ksi, are the normal and the tangent stiffness per unit contact area in the contact/stick state, respectively. The large value of stiffness (40000 ksi) given to the interface elements is used to limit the relative movement between steel and concrete prior to reaching the failure surface. The parameter α maintains numerical stability of the model by producing a non-singular stiffness in the interface elements as they progress to the separation state. A value of 0.001 is used for α.

While the stiffness values are used to limit the relative displacements between the steel and the concrete, the coefficient of friction, μ, and the cohesion, c, define the failure surface. The values for c and μ are 0.25 ksi and 0.3, respectively. In the absence of experimental data for these properties, values used in other finite element studies of bond at the University of Kansas (Choi et al. 1990, 1991; Hadje-Ghaffari et al. 1991; McCabe et al. 1992) were chosen. Recent (unpublished) work at the University of Kansas shows that a higher value of μ would be more appropriate. Therefore, the strengths produced in this study may be conservative.

2.4 Concrete Substructure

The concrete substructure is modeled using linear 8-node, 3-dimensional isoparametric brick elements (Fig. 2.13). The elements do not contain a midside node, producing a linear shape function. Throughout the analysis, the concrete elements in the model are treated as linear elastic, and concrete crushing in front of the deformations is not modeled. The material properties for these elements include a modulus of elasticity of 4000 ksi, corresponding to a compressive

strength of approximately 6 ksi and a Poisson's ratio of 0.20. Fig. 2.14 shows the concrete substructure of the finite element model (in this case for a model with 3 ribs). Each concrete substructure is modeled with notches to allow the ribs to be embedded in concrete.

2.5 Reinforcing Steel Substructure

8-node elements (Fig. 2.13) are also used to model the steel. The shape and spacing of the deformations are selected to match typical reinforcing bars (Choi et al. 1990). Two deformation heights, 0.06 in. and 0.09 in. (0.09 in. is about 50 percent higher than ribs on most 1 in. diameter bars), are analyzed (Fig. 2.15). A center to center spacing of 0.64 in. is used for both deformation heights. One-half in. and 2 in. lead lengths (distance from the front of the specimen to the first rib) are investigated. The majority of the analyses involve ribs with face angles of 45° (relative to the longitudinal bar axis). To better approximate the face angles found on standard reinforcing bars, additional analyses are carried out on ribs with a multi-angled face. These ribs have a rib face angle of 45° for the first 1/4 of the rib height, 60° for the next 1/2 of the rib height, and 45° for the final 1/4 of the rib height. The rib dimensions, along with the rib face angles, are shown in Fig. 2.15. The embedded length of the models is increased by adding deformations to the steel substructure; the number of notches in the concrete substructure is adjusted accordingly. Models consisting of 1, 2, 3, 6, and 12 ribs are evaluated. The embedded lengths of these models range from 0.82 in. to 7.86 in., increasing 0.64 in. with each additional rib.

To simplify the representation, a square bar is used, with deformations placed on the vertical face of the bar (normal to the crack surface) (Fig. 2.16). While this is a crude representation of round bars, the square bar accurately models the mechanical interlock between the steel and the concrete produced by the deformations (Lutz and Gergely 1967) and causes splitting of the type observed in beam-end test specimens. Like the concrete, the reinforcing steel is modeled as linear elastic throughout the analysis. The material properties of the steel elements include a modulus of elasticity of 29000 ksi and a Poisson's ratio of 0.30.

2.6 Transverse Reinforcement

Transverse reinforcement is modeled as a series of rod elements (Fig. 2.5) placed directly above the reinforcing bar and extending into the model perpendicular to the crack plane. The rods are connected end to end to give the stirrup an overall length of 3.5 in. Each rod element has a cross-sectional area of 0.11 in., corresponding to the area of a No. 3 bar. In the current study, confinement provided by two stirrups is investigated. The stirrup spacing is 3 in., with the first stirrup placed 1.0 in. from the front face of the specimen. One node point of the stirrup is located at the crack plane of the specimen and is constrained from movement in the x-direction (Fig. 2.18). The remaining stirrup node points are shared by the concrete elements that lie along the stirrup length; the stirrups and the adjacent concrete are assumed to be perfectly bonded. The stirrup elements are modeled as elastic-perfectly plastic, with a modulus of elasticity of 29000 ksi, a Poisson's ratio of 0.30, and a yield stress of 60 ksi.

2.7 Boundary Conditions

In finite element studies of beam-end specimens modeled at the University of Kansas (Niwa 1991), stress conditions near the reinforcing bar were found to match those found in flexural members when the compressive zone (location of compressive reaction) was placed 13 in. or more below the bar (Fig. 2.17). The boundary conditions used in this study provide similar stress conditions in the smaller model, while realistically simulating the constraints on the beam-end specimen. The boundary conditions constrain the bottom surface of the model (x-y plane) against vertical movement and the center line of the x-y plane (oriented in the x-direction) against (horizontal) movement in the y direction (Fig. 2.18). These constraints place the compressive zone in the concrete far below the test bar. To insure that no eccentricity is introduced as the bar is displaced, the nodes on the edge of the reinforcing bar along the crack plane are constrained to move only in the direction of the imposed displacement.

2.8 Solution Procedure

Because of the nonlinear nature of the problem resulting from splitting of the concrete and slip along the steel-concrete interface, the analysis is accomplished using an incremental, iterative Newton-Raphson procedure. In a nonlinear finite element analysis, loads are applied by imposing small displacements (load steps) on the structure (in this case, displacements are applied in the negative y direction on the nodes at the front end of the reinforcing steel substructure, as shown in Fig. 2.18) to obtain a stable solution with a minimum number of iterations. In the first ten load steps, displacements are applied in 0.0001 in. increments, as the bar begins to slip along the interface surface. Once all of the interface elements have reached the contact/slip state, the step size is increased to 0.0005 in. up to the point of the peak load.

The initial material properties of the elements are used to form the global stiffness matrix for the first load application. As the load is applied, the strains and stresses in the crack rod and interface elements are computed based on the calculated nodal displacements and initial material properties. Only one iteration is required for a load step if the stress-strain behavior of the elements remains linear. "Unbalanced forces" are possible if the stress-strain behavior of the elements becomes nonlinear, requiring an iterative solution. The unbalanced forces, or residual loads, represent the difference between the total nodal loads applied to the structure and the nodal loads required to keep the structure in the equilibrium based on material properties corresponding to the current state of strain in the elements. With each successive iteration (for a given load step), the element properties are updated to take into account the nonlinear response of the elements, and the only loads applied to the structure are the residual loads.

For the crack rods, element stiffness is set equal to the secant stiffness once "cracking" has occurred (the stress-strain response is on the descending branch of the stress-strain curve). The secant stiffness is the slope of a line in stress and strain space from the origin to the point on the stress-strain curve corresponding to the current strain (Fig. 2.19). The difference between the calculated stress based on the material properties assumed prior to the iteration step and the stress based on the total strain at the end of the iteration step is the residual stress, which is used, in

turn, to calculate the residual load.

For the interface elements, the procedure is somewhat different. In this case, the failure surface is modified by reducing the cohesion, c, to zero once slip (Eq. 2.4) takes place. The residual stress vector is equal to the difference in shear between the values on the original and new slip surfaces (Fig. 2.20). In this case, the normal stiffness is held constant and the shear stiffness is multiplied by μ (Eq. 2.8). As the analysis proceeds, the interface elements in the contact/slip mode remain in this state, and the stresses in these elements are related to the modified contact/slip surface.

The iterative solution continues until the ratio of the Euclidean norm (square root of the sum of the squares) of the residual load vector to the Euclidean norm of the applied load vector is less than a prescribed error, known as the convergence parameter. In the current study, the convergence parameter is 0.5 percent, less stringent than the value of 0.1 percent used in earlier studies at the University of Kansas (Choi et al. 1990, 1991; Hadje-Ghaffari et al. 1991; McCabe et al. 1992). No problems were encountered using a convergence parameter of 0.5 percent, and the solution time was reduced compared to the earlier work.

The time required to complete an analysis (reach a model's peak load) is controlled by how often the stiffness matrix is updated and triangularized and how rapidly the solution converges. If, as done in this study, stiffness matrix updates are performed before each iteration, the number of stiffness matrix triangularizations increases, but the residual loads are distributed throughout the entire structure more accurately, reducing the total number of iterations within a load step (Cedolin and Dei Poli 1977).

In the current study, convergence is generally obtained within 10 iterations for each of the first 5 load steps. The convergence rate greatly improves in the remaining load steps, since all of the interface elements have advanced from the stick to the slip state and no further change of state results. While approaching the peak load, the number of iterations again increases as more crack rods reach w_o, and the confining force provided by the concrete decreases. The end of the analysis is typically marked by a load step not converging as the specimen crack is fully opened.

CHAPTER 3

NUMERICAL RESULTS

3.1 Introduction

Finite element analyses were carried out to evaluate the effects of deformation height, deformation face angle, concrete cover, lead length, embedded length, and confining reinforcement on the bond performance of reinforcing steel to concrete. All analyses were performed on models of a beam-end specimen using the material properties and the solution procedure discussed in Chapter 2.

The main emphasis of this study deals with the role that deformation pattern plays in the bond process. In the finite element models, the deformation pattern of the steel bar is changed by increasing the rib height from 0.06 in. to 0.09 in. The majority of the models have ribs with face angles of 45°. Additional analyses on models with multi-angle rib faces (see Fig. 2.16) were conducted to study the effects of rib face angle on bond.

The experimental results show trends of increasing bond strength when the confinement provided by the concrete is increased (Darwin and Graham 1993). The additional confinement can be improved by increasing the concrete cover above the bar, increasing the lead length, or adding transverse reinforcement to the specimen. To study the effect of additional confinement, models with 1, 2, and 3 in. covers, one-half in. and 2 in. lead lengths, and models with stirrups are investigated. Finally, the effects of the embedded length on bond force are studied. Models with 1, 2, 3, 6, and 12 ribs are evaluated. In the cases involving a multi-angle rib face, models with up to 3 ribs were considered.

This chapter describes the numerical results from the finite element analyses of the beam-end specimens. Bond performance is evaluated using load-slip, load-cover, and load-embedded length plots for the models. The results for models with different deformation heights, deformation face angles, covers, lead lengths, embedded lengths, and stirrups are presented and compared with the experimental behavior observed by Darwin and Graham (1993).

3.2 Load-Slip Response

Load-slip curves are generated for each model by calculating the load required to give the bar a specified displacement. The total load for the model is obtained by multiplying these results by two since only one-half of the specimen is modeled. The bond force for a particular model is defined as the peak load obtained by the bar; this occurs at the imposed displacement causing the splitting failure of the concrete substructure. In this section, unless otherwise noted, the load-slip response discussed is that of a model with 6 ribs, 2 in. cover, and 1/2 in. lead length. The general characteristics described can be applied to all of the models. The bond forces and the corresponding values of bar slip are summarized for all models in Table 3.1.

Within the first ten load steps (generally, a loaded end slip of 0.0009 in. or less), progressive material state changes in the interface elements between the steel and concrete occur along the length of the bar. At the beginning of an analysis, all interface elements are in the contact/stick state. As displacements are applied to the loaded end of the reinforcing bar, the interface elements begin to change state according to their position along the length of the bar. Fig. 3.1 shows the typical pattern of interface element material state changes. For the cases in which the rib face angle is a constant 45°, the slip state is first reached in the interface elements located on the rib closest to the applied displacement. As the displacement increases, the interface elements on each successive rib change to the contact/slip state (within a single load step), until all of the interface elements along the interface have advanced to this state. For the models with multi-angle rib faces, the change of material state in the interface elements on a rib usually occurs over the course of two load steps. During the first of these load steps, the interface elements on the bottom and top of the rib (Fig. 2.10) reach the contact/slip state, followed by the interface elements on the center portion of the rib in the second load step. In all cases, the interface elements on the compression faces of the ribs remained in the contact/slip state for the balance of the analysis.

When, as used in this study, interface elements are placed only on the compression face of each rib (see Section 3.3), no additional changes in material state occur at the bar surface once all

of the interface elements have advanced to the contact/slip state. In this state, displacements at the interface consist of three components: sliding of the steel parallel to the direction of the applied load, offset or overlap due to compression of the interface element, and normal displacement due to compression of the concrete (Choi et al. 1990). Fig. 3.2 illustrates the movement of the interface at one rib location from the initial load to the peak load. The sliding and normal displacements are illustrated by the movement of the steel and concrete nodes, respectively, from their initial positions to the positions at the peak load. Fig. 3.2 also shows a small amount of overlap (offset) as the steel moves relative to the concrete. In practice, the offset is, of course, zero. In the current study, the offset is minimized using a link element with a large value of stiffness normal to the interface, as discussed in Chapter 2. Typical results from the study show that the value for offset at the peak load, 0.00046 in., is relatively small compared to the corresponding normal and sliding components, 0.0065 in. and 0.0094 in., respectively.

As the bar slides relative to the concrete, a splitting failure of the specimen results from the wedging action produced by the ribs moving through the concrete substructure. In experimental tests of beam-end specimens, a sudden failure is observed (Darwin and Graham, 1993). In the finite element analysis, the models also exhibit a sudden, brittle failure, as seen in Fig. 3.3. The sudden failure results from both the characteristics of a wedging failure and the brittle behavior of concrete when placed in tension. As the displacement corresponding to the peak load is attained, the ability of the concrete to apply a clamping force on the steel bar decreases, leading to specimen failure. This decrease in clamping force is clearly illustrated by the response of the specimen.

Differences between the loaded end and the unloaded end slips reveal the reduction in the clamping force as the peak load is reached. Fig. 3.4 shows typical load versus loaded end slip and load versus unloaded end slip responses. Initially, the stiffness of the load-loaded end slip curve is lower than that of the load-unloaded end slip curve; the concrete is able to clamp down on the bar, limiting the slip at the unloaded end. However, as seen in Fig. 3.4, after the peak load is reached, the "softer" concrete can no longer provide as great a clamping force to the bar and the

unloaded end displacements "catch up" with the displacements at the loaded end as the crack is fully open.

A reduction in the clamping force provided by the concrete is also illustrated in Fig. 3.5, which shows the typical displacement patterns along the length of the bar as the imposed displacement is increased. Over the embedded length (lead length plus bonded length) of the bar (5.42 in.), slip decreases as the distance from the point of load (location = 0) increases. With each successive load step prior to the peak load, the difference in the slip from the front (near the applied load) to the back (at the location of the last rib) of the embedded length increases, as the concrete is able to resist the movement of the bar. In load step 20, for example, there is a 0.00248 in. difference in slip between the front and the back of the 6.02 in. embedded length. In load step 30 (prior to the peak load), a 0.00416 in. difference in slip is seen. When the crack is fully open (load step 31), the amount of slip along the embedded length of the bar has flattened out, and only a 0.0020 in. difference in slip exists over the embedded length. At the peak load, the concrete provides little clamping force to the bar and the ribs provide only a small amount of resistance to further movement.

Stresses in the interface elements show the loss in the ability of the concrete substructure to resist steel bar slip at the peak load. Fig. 3.6 shows the magnitudes of the stresses in an interface element on the compression side of the rib closest to the loaded end of the bar. The increases in the normal and shear stresses are nearly linear as load is applied. Once the peak load is attained, a sharp decrease in the normal and shear stresses occurs. The decrease in the normal stress is due to the loss of the clamping force provided by the concrete.

Experimental studies of steel-concrete bond have shown that concrete surrounding the loaded side of the ribs is crushed as the bar moves through the concrete (Rehm 1961; Lutz et al. 1966, 1967; Choi et al. 1990, 1991; Hadje-Ghaffari et al. 1991; Darwin and Graham 1993). However, recent observations at the University of Kansas (Darwin et al. 1993) suggest that only a small amount of crushing occurs until after the peak load is attained. In the current study, all concrete elements remain linear elastic throughout the analysis, and no provision is included in the

finite element models to account for crushed concrete. Whether or not crushing occurs prior to the peak load, the relatively coarse finite element mesh used in this study (coarse for studying stresses around ribs) means that it is not possible to obtain completely accurate values of concrete element and interface element stresses. At the peak load, stresses in the concrete elements near the interface range from 7 ksi to 12 ksi, considerably higher than the 5 ksi compressive strength assumed for the concrete. A finer finite element mesh might have revealed higher stresses. Despite being in a triaxial state of stress, portions of the concrete represented by these elements could very well have been crushed. If so, the values of both interface stress and bond force would have been somewhat lower than obtained in this study.

3.3 Effect of Placing Interface Elements only on Compression Faces of Ribs

Each finite element model has a specified bonded region in which the ribs of the steel bar are connected to the surrounding concrete using interface elements. In the finite element models, the only interaction between the steel and concrete occurs within this region. Originally, it was assumed that the entire bonded region would require interface elements to accurately define the steel-concrete contact surface. To do this, interface elements were placed at every node point along the interface. Seven interface elements were required for each rib (on models with 45° face angles) within the bonded region (see Fig. 2.10). When interface elements are placed along the entire bonded length, convergence for the first 10 load steps is slow (requiring as many as 20 iterations within a load step), as all of the interface elements change material states. At low levels of displacement, the link elements not on the compression side of the deformation reach the separation state and no longer contribute to the bond strength.

Modifications in modeling the steel-concrete interface were made as the study progressed. In an effort to reduce the analysis time, the behavior of models with interface elements placed only on the compression side of a rib were investigated. In Fig. 3.7, the load-slip behavior of models with interface elements placed on the compression faces of the ribs and models with interface elements placed on all rib faces is compared. As shown in Fig. 3.7, placing the interface elements

only on the compression face of the ribs has a minimal effect on the bond strength, with the mechanical interaction between the steel and concrete primarily contributing to bond (Menzel 1939; Lutz and Gergely 1967). As well as reducing the overall analysis time, placing interface elements only on the compression faces of the ribs gives a good match with the load-slip behavior when interface elements are placed on all rib faces. The bond strengths discussed in this report are based on models with interface elements placed only on the compression faces of the ribs.

3.4 Effect of Rib Height

Load-slip curves for models with deformation heights of 0.06 in. and 0.09 in. are shown in Figs. 3.8, 3.9, and 3.10 for bars with covers of 1, 2, and 3 in., respectively. These figures show that an increase in rib height results in an increase in stiffness of the load-slip curves, but little change in the peak load (See also Table 3.1). This behavior has also been seen in experimental beam-end specimens without transverse reinforcement (Darwin and Graham 1993). On 1.0 in. diameter bars with rib heights of 0.05 in., 0.075 in., and 0.10 in, Darwin and Graham (1993) observed that changes in rib height have no effect on bond strength, if the bars are not confined by transverse steel.

Increasing the rib height results, in most cases, in a small decrease in the slip at which the peak load is attained. With a rib height of 0.09 in., a greater amount of rib area is in contact with the concrete than with a rib height of 0.06 in. As the bar is displaced, the wedging action produced by the increase in rib bearing area (resulting from increasing the rib height to 0.09 in.) is increased, causing the concrete to split at displacements as much as 15% lower than the cases with the rib height of 0.06 in.

With an increase in rib height, the decrease in slip at the peak load is not accomplished at the expense of bond strength. Little or no change in bond strength is observed as the rib height is increased from 0.06 in to 0.09 in. (Figs. 3.8, 3.9, and 3.10). Generally, differences in bond strengths resulting from an increase in rib height are less than 1.5%. For certain cases (1 rib, 3 in. cover; 3 ribs, 1 in. cover; and 6 ribs, 3 in. cover), the differences in bond strengths range from

2.0-3.5%. Also, except for the cases with 1 rib, bond strength increases with an increase in rib height. Overall, there appears to be little change in the wedging action or bond strength produced by ribs of different heights for models not confined with transverse reinforcement.

3.5 Effect of Rib Shape

Figs. 3.11, 3.12, and 3.13 offer a comparison of bond force-slip relationships as a function of rib shape. In each case, a lower load-slip stiffness is obtained with multi-angled ribs than with the 45° ribs. However, the models exhibit little or no difference in bond force. The bond force versus cover plots in Fig. 3.14 and the bond force versus embedded length plots in Fig. 3.15 show that the change in the shape of the ribs results in no more than a 1% change in bond strength. These results show that there is little difference in the wedging effect of the two rib shapes studied.

The greater slip at the peak load exhibited by the bars with the multi-angle rib faces appears to be tied to the behavior of the finite element model. As discussed in Section 3.2, under load, the steel nodes slightly overlap the concrete nodes on the compression faces of the ribs. Throughout the analysis of a model with multi-angle rib faces, no interface elements reach the separation state, and the stresses in the interface elements on the 60° portion of the ribs are approximately 50% higher than those in the interface elements on the 45° ribs. The increase in interface stress produces an increase in an amount of steel and concrete overlap that is nearly equal to the difference in slip between the two types of bars. For example, the overlaps for 2-rib models with multi-angle rib faces and a 45° rib face are 0.00926 in. and 0.00765 in., respectively. The difference in the two values of offset, 0.00161 in., explains the 0.0016 in. difference in slip at the peak load between the two cases.

3.6 Effect of Concrete Cover

In experimental work using beam-end specimens (Darwin and Graham 1993), bond strengths increase as the confinement provided by the concrete to the reinforcing bar is increased.

One method of increasing this confinement is to increase the concrete cover above the bar. With increased cover, the clamping force provided by the concrete to the bar is increased, producing an increase in bond strength.

In this study, the effect of concrete cover on bond strength is evaluated using the finite element models. The load-slip curves in Figs. 3.16 through 3.18 and the bond force-cover curves in Fig. 3.19 show that bond strength and stiffness increase as the concrete cover increases. Also, Figs. 3.16, 3.17, and 3.18 show that, with one exception (0.06 in. rib, 1 in. cover, 1 rib, Fig. 3.16), a higher bar displacement is required to split the models as the cover is increased. Figs. 3.20 to 3.21 compare load-unloaded end slip curves for the 45° rib and multi-angle rib face models, respectively, as a function of cover. The stiffness of the load-unloaded end slip curves increases with increasing cover.

Increasing the concrete cover significantly increases bond force, since the steel bar must split the additional concrete above the bar. The load-slip behavior of the models undergoes definite changes when the amount of cover is increased, as shown in Fig. 3.16. Using the 6 rib cases in Fig. 3.16 as an example, the amount of cover appears to have little effect on bond strength for a bar slip under approximately 0.002 in. Below this slip, the slopes for all 3 covers are virtually the same, and the amount of bond strength relies mainly on the interface properties and mechanical interlock. As the slip increases above 0.002 in., the relative stiffness of the load-slip curves increases with increasing cover.

The comparisons of bond force versus cover in Fig. 3.19 show how changes in concrete cover affect the bond force for a particular model. For models with 1, 2, 3, and 6 ribs, the increase in bond strength is nearly linear with an increase in cover (Fig. 3.19). This description does not apply, however, to the models with 12 ribs. In these cases, the increase in bond strength that results from increasing the cover is not linear; the bond strength produced by models with 1 in. cover is slightly less than would be expected for a linear relationship. Overall, these results illustrate the strong relationship between increasing bond strength and additional cover observed in practice for beam-end specimens (Choi et al. 1990, 1991).

Darwin and Graham (1993) observed that deformation pattern has no effect on bond strength when strength is governed by a concrete splitting failure. Under these conditions, the ability of a bar to act as a wedge is not dependent on the deformation pattern. Splitting failures occurred in all finite element models, and the results from the current study match the experimental observations. Darwin and Graham did show, however, that bond strength is sensitive to deformation pattern, as represented by the relative rib area of a bar, R_r, if the bar is confined by transverse reinforcement and, under some conditions, by concrete. The relative rib area, R_r, is the ratio of the projected rib area normal to the bar axis to the nominal bar perimeter multiplied by the center-to-center rib spacing. Darwin and Graham also showed that the initial stiffness of the load-slip curves increases with an increase in R_r under all conditions.

Based on this definition of relative rib area, an increase in rib height may also be considered an increase in R_r since the center-to-center spacing of the ribs is constant (0.64 in.) in the finite element models. Therefore, the 0.09 in. rib height used in the current study has a greater R_r than the 0.06 in. rib height. Darwin and Graham's observation that the initial stiffness of the load-slip curve increases with an increase in R_r is supported by the current study, as seen in Figs. 3.8, 3.9, and 3.10.

The effects of R_r on bond strength under conditions of increased confinement of the bar were demonstrated using a simultaneous increase in cover (from 2 in. to 3 in.) and an increase in lead length from 1/2 in. to 4 in. This comparison was beyond the scope of this study, but remains an interesting comparison for future studies.

3.7 Effect of Lead Length

In experimental studies on bond using beam-end specimens (Choi et al. 1990, 1991; Hadje-Ghaffari et al. 1991; Darwin and Graham 1993), precautions were taken to prevent a cone-type pullout failure that would lead to an inaccurate measure of the bond force developed along the length of the steel-concrete interface. A splitting failure is desired in these specimens and is achieved by moving the bonded region away from the front face of the specimen. The lead length,

the length of the unbonded bar near the front of the specimen, reduces the stress field ahead of the bonded region and cuts down on the chances of a cone-type failure (Choi et al. 1990). The bond force-slip behavior of bars with 0.06 in. ribs and lead lengths of 1/2 in. and 2 in. are compared in Fig. 3.22. From these curves, it is evident that the bond strength increases as the lead length increases, consistent with the experimental findings (Choi et al. 1990, 1991; Hadje-Ghaffari et al. 1991, Darwin and Graham 1993). Fig. 3.23 compares the bond strengths of bars with two different lead lengths as a function of the total embedded length (the length from the front of the specimen to the end of the bonded region). In both cases, an increase in embedded length produces a nearly linear increase in bond strength, but, for equal embedment, the bars with the higher lead length exhibit a higher bond strength.

These results show that an unbonded region of bar can play an important part in the bond strength measured using a beam-end specimen. The increase in bond force for the models with 2 in. lead lengths is the result of the additional energy needed to drive the crack through a greater volume of concrete ahead of the bonded region. The higher strength, at the same embedded length, of the bars with 2 in. lead length may be due to higher confinement provided to the first ribs as compared to the first ribs in the bars with the 1/2 in. lead length.

3.8 Effect of Embedded Length

The length of the bar directly in contact with the concrete is known as the bonded length. The sum of the lead length and the bonded length is known as the embedded length. Increasing the embedded length does not change the overall length of the model. The effects of increasing the embedded length of a model are shown in Figs. 3.24 and Figs. 3.8-3.11.

The load-slip curves in Fig. 3.24 and 3.9 reveal two trends resulting from an increase in embedded length. First, an increase in embedded length produces an increase in bond force. Second, by increasing the embedded length from 0.82 in. (1 rib) to 4.02 in. (6 ribs), the amount of steel bar displacement required to split the concrete decreases. For an increase in embedded

length to 7.84 in. (12 ribs) (Fig. 3.8-3.10), the amount of slip at the peak load increases (approximately 0.0005 in.).

Bond force is compared as a function of embedded length for bars with 1, 2, 3, 6 and 12 ribs (45°) with heights of 0.06 in. and 0.09 in. in Figs. 3.25 and 3.26, respectively. The figures show that, for models with 2 and 3 in. covers, bond force increases nearly linearly with increasing embedded length. This observation does not hold for models with 1 in. cover, as the bond force provided by the model with 12 ribs is less than would be expected for a linear relationship. This behavior suggests that an increase in embedded length is not as effective at low covers as it is at higher covers. For all covers, the bond forces for models with 1 and 2 ribs are slightly higher than would be expected for a truly linear relationship.

In Fig. 3.27, the bond force values from Fig. 3.25 are plotted as a function of $l_d(C + 0.5d_b)$, in which l_d is the embedded length, C is the concrete cover, and d_b is the bar height. The $l_d(C + 0.5d_b)$ term represents an area of fractured concrete along the embedded length measured from the top of the specimen to the center of the bar. Fig. 3.27 clearly shows that, as observed in practice (Orangun et al. 1975; Darwin et al. 1992a, 1992b), bond force does not drop to zero for short embedded lengths. For short embedded lengths (models with 1, 2, and 3 ribs), a large amount of scatter is observed in the data. In Fig. 3.28, only bond strengths for models with 6 and 12 ribs are plotted as a function of $l_d(C + 0.5d_b)$. In this case, a nearly linear increase in bond strength with an increase in $l_d(C + 0.5d_b)$ is observed.

In Fig. 3.29, the area of concrete along the crack surface that is split during the analysis of models with 1, 3, 6, and 12 0.06 in., 45° ribs is presented. Each curve in Fig. 3.29 represents the rear boundary of the crack rod elements that have reached the descending branch of the stress-strain curve (Fig. 2.7) when the peak load is attained. The total area of concrete that is split is calculated from the summation of the tributary areas of these crack rods. Not including the area of the bar, the total area of concrete on the potential crack plane in the models with 2 in. cover is 84 $in.^2$ The results show that the amount of split concrete is not proportional to the embedded length.

The greatest increase in the area of split concrete is observed when the embedded length is increased from 0.82 in. (1 rib) to 2.10 in. (3 ribs). Increases in the area of split concrete are less significant as the embedded length is increased from 2.10 in. to 4.02 in. (6 ribs) and from 4.02 in. to 7.86 in. (12 ribs). For the 1 rib case, 33.9 in.^{2} (40% of the total area) of concrete is split. When the embedded length is increased to 2.10 in., 38.625 in.^{2} (46% of the total area) is involved in splitting; by increasing the embedded length by 156%, the amount of split concrete has increased by only 13%. A further 91% increase in embedded length (from 2.10 in. to 4.02 in.) produces only a 3.8% increase in the amount of split concrete. Finally, another 95% increase in embedded length (from 4.02 in. to 7.86 in.) produces only a 4% increase in the amount of split concrete at the peak load. These observations provide a clue as to why bars with very low values of l_d can have substantial bond strength and why bond strength does not increase linearly with embedded length (Darwin et al. 1992a, 1992b).

3.9 Lateral Displacements

A measure of the degree of concrete splitting at the peak load is provided by the lateral displacement of the model. The displacements (perpendicular to the length of the bar) are measured at the top of the cover along the outside surface (parallel to the splitting crack plane) to avoid possible elastic deformation near the steel-concrete interface. The lateral displacements at the front face of the models coinciding with the peak load are summarized in Table 3.2 for the models used in this study.

Fig. 3.30 contains a set of bond force-lateral displacement curves for a model with 6 ribs (0.09 in.) and 2 in. cover. The curves represent bond force-lateral displacement behavior at points 0.0, 1.24, 3.8, 6.0, and 12.0 in. from the front face of the specimen. The lateral displacement at the front face of the specimen is the greatest. At a given value of bond force, the lateral displacements decrease along the length of the specimen. As discussed earlier in Section 3.8, the crack does not propagate along the entire length of the model. Behind the crack, negative values

of lateral displacement are observed, indicating that bending perpendicular to the crack plane is present.

In Fig. 3.31, bond force-lateral displacement (at the front face of model) curves are plotted for 0.06 in. 45° rib models with 1, 2, and 3 in. covers. At every value of bond force, an increase in cover causes a decrease in the amount of lateral displacement at the peak load. At failure, the values of lateral displacement at the peak load increase 42% when the cover is reduced from 3 in. to 1 in. It appears from these results that the amount of lateral displacement is dependent on the amount of cover.

Engineers are often concerned with the possibility of premature longitudinal splitting along the length of a bar that might be caused by ribs that are too high, and some researchers have pointed out that the degree of splitting is a function of the rib deformation pattern. Losberg and Olsson (1979) showed that the distance between the ribs is not as important as the rib height in causing splitting failures; the possibility of a splitting failure increases with an increase in rib height. Soretz and Holzenbein (1979) showed that bars with rib heights of $0.10d_b$, $0.05d_b$, and $0.025d_b$ produced nearly identical bond strengths. However, like Losberg and Olsson (1979), they observed that the tendency of concrete to split increases with increasing rib height. The findings of the current study agree with these observations, but only for displacements after the peak load has been attained. Fig. 3.32 shows the bond force-lateral displacement curves for bars with rib heights of 0.06 in. and 0.09 in. Up to the peak load, the lateral displacement is virtually identical for the two models. After the peak load, the maximum lateral displacement produced by the bar with 0.09 in. rib height is 23% greater than the lateral displacement caused by the 0.06 in. rib height. It is this greater amount of lateral displacement, after the peak load, that is normally associated with the effect of rib height on splitting.

Rather than the lateral displacement after failure, it is the lateral displacement of coinciding with the peak load that provides the more accurate measure of the tendency of a reinforcing bar to cause splitting. In Fig. 3.32, at the peak load, the lateral displacements produced by the 0.09 in. and 0.06 in. rib heights are 0.002873 in. and 0.002808 in., respectively; a 50% increase in rib

height produces only a 2% increase in lateral displacement at the peak load. These results show that the lateral displacement up to the peak load is essentially independent of rib height, matching the findings of recent experimental work at the University of Kansas (Darwin et al. 1993).

The effect of rib shape on the degree of splitting is shown in the bond force-lateral displacement curves in Fig. 3.33. For 2 rib models, the lateral displacements at the peak load for multi-angle and 45° angle rib faces are 0.002649 in. and 0.002647 in., respectively. The 1% difference in lateral displacement coinciding with the peak load suggests that the degree of splitting is also independent of rib shape.

3.10 Effect of Transverse Reinforcement

In their beam-end specimen tests, Darwin and Graham (1993) observed that under conditions of increased confinement provided by transverse reinforcement, bond strength increases compared to bond strength of bars with no confinement. They also observed that the magnitude of the increase in bond strength increases with an increase in relative rib area.

In the finite element analysis, the effects of transverse reinforcement on bond strength are evaluated using models having 2 ribs, 2 inch cover, and 1/2 in. lead length. For these models, 2 No. 3 stirrups (area = 0.11 in.^{2}) are added, with the stirrups placed 1 and 4 in. from the front face of the model. Both stirrups are placed directly above the reinforcing bar. Fig. 3.34 compares the load-slip behavior of models with rib heights of 0.06 in. and 0.09 in. with and without transverse reinforcement. Fig. 3.34 shows that the bond strengths nearly double with the addition of transverse reinforcement. This percentage increase is greater than might be expected in practice due to the presence of the stirrups; however, it should not be unexpected in this case since the model has high stirrup confinement for a very short embedded length.

Darwin et al. (1993) have observed that specimens with stirrups exhibit a greater lateral displacement at failure than specimens without stirrups. In the current study, the two rib models with stirrups had a lateral displacement at the peak load of 0.006133 in. for a rib height of 0.06 in.

and 0.006242 in. for a rib height of 0.09 in., representing an increase of nearly 81% and 78% over the same models without stirrups (See Table 3.2).

The confined bars with 0.09 in. ribs provide 2.2% more bond strength than the confined bars with 0.06 in. ribs, qualitatively (but not quantitatively) consistent with the experimental findings that bars with higher R_r provide more bond strength under conditions of additional confinement (Darwin and Graham 1993). The work by Darwin and Graham (1993) indicates that a 50% increase in R_r should have a much larger effect on the bond strength of a confined bar. For both models with transverse reinforcement, the maximum strength is attained when the first stirrup yields. This behavior contrasts the findings by Maeda et al. (1991) which show that stirrups usually do not yield at specimen failure. It appears that stirrup yielding, as well as the great increase in bond strength, are the direct result of the concrete surrounding the ribs remaining linear elastic throughout the analysis. The inclusion of concrete crushing would allow a more accurate representation of load-slip behavior under conditions of additional bar confinement and should be addressed in future finite element bond analyses. The likely outcome would be a reduction in the predicted bond strength and an increase in the effect of R_r, since an increase in rib area would delay the onset of concrete crushing.

3.11 Statical Model

Choi et al. (1990) and Hadje-Ghaffari et al. (1991) developed a simple statical model (Fig 3.35) of two rigid bodies in contact to represent the relationship between the pull-out force for a reinforcing bar and the clamping force provided by the concrete. In Fig. 3.35, the upper rigid body represents the concrete. It is constrained in the horizontal direction and the compressive force, P, represents the clamping force provided by the concrete. The lower rigid body represents the reinforcing steel. This rigid body is constrained in the vertical direction, and the pull-out force, H, represents the bond force between the bar and concrete. The face angle between the two bodies, γ, represents the face angle of the ribs on the steel bar.

To maintain equilibrium,

$$H = P\frac{(\tan\gamma + \mu)}{(1 - \mu\tan\gamma)} + \frac{AC}{\cos\gamma(1 - \mu\tan\gamma)} \qquad (3.1)$$

in which A and C represent the contact area and cohesion, respectively (Hadje-Ghaffari et al. 1991). For ribs with face angles of 45° that are sliding, Eq. 3.1 can be simplified to

$$H = P\frac{(1 + \mu)}{(1 - \mu)} \qquad (3.2)$$

since the cohesion, C, goes to zero at low levels of displacement (see Section 2.3).

Eq. 3.2 is used in the current study to show how the pull-out force relates to the clamping force provided by the concrete. The pull-out force, H, is calculated as the sum of the forces on the bar at the peak displacement, as discussed in Section 3.2. The clamping force, P, is the sum of the components of the interface element shear and normal stresses that act normal to the longitudinal axis of the bar multiplied by the interface contact area.

Using the 6 rib case with 2 in. cover as an example, the average shear and normal components of interface stress are 8.79 ksi and 29.32 ksi, respectively. The sum of the normal forces acting on the bar is 7.38 kips, representing the clamping force on one side of the bar. Substituting P = 7.38 and μ = 0.3 into Eq. 3.2, the resulting pull-out force is 13.7 kips for one-half of the bar or 27.4 kips for the full bar. The actual pull-out force resulting from the finite element analysis is 27.7 kips, corresponding to a 1% difference between the two cases. From this simple comparison, it appears that, even for a bar with multiple ribs, the pull-out force can be related to the total clamping force along the length of a splitting crack without the use of a complex finite element model. This observation is likely to be quite useful in the development of a simple, rational design approach for developing and splicing reinforcement. The key task appears to be the formulation of the peak clamping force for a given configuration of reinforcing bars.

CHAPTER 4

CONCLUSIONS

4.1 Summary

Research is underway at the University of Kansas to improve the development characteristics of reinforcing bars. Through experimental and analytical work, the effects of deformation pattern on bond strength are investigated. The work summarized in this report uses finite element analysis to determine how the deformation pattern affects the bond of reinforcing bars to concrete.

In the initial portion of the experimental work (Darwin and Graham 1993), beam-end specimens were the primary means of investigating steel-concrete bond. These specimens are designed to provide a measure of the bond force developed at the steel-concrete interface by duplicating the stress conditions in an actual beam, where both the concrete and the reinforcing steel are placed in tension. A splitting-type failure caused by the wedging action of the bars is observed in these specimens (Choi et al. 1990, 1991; Hadje-Ghaffari 1991; Darwin and Graham 1993). The finite element analyses in the current study are intended to model the splitting behavior of beam-end specimens and explain the observed experimental trends.

A nonlinear finite element analysis is employed to study the bond mechanism. The finite element model of a beam-end specimen includes representations of the deformed bar, the concrete, the splitting crack plane, and the steel-concrete interface. Three-dimensional, eight-node, linear, isoparametric elements are used to model the steel and the concrete. Rod elements and a nonlinear fracture mechanics scheme, known as the fictitious crack model (Hillerborg et al. 1976) are used to model the longitudinal splitting crack. The steel-concrete interface is modeled using special link elements that follow a Mohr-Coulomb failure law.

The analyses are performed on a model of the upper portion of a beam-end specimen. The height of the model varies depending on the amount of concrete cover above the bar. The splitting crack in the model is assumed to occur along the specimen center line, and only one-half

of the specimen width is modeled. The embedded lengths of the models are increased by adding additional ribs to the steel bar. While the embedded length is increased, the overall specimen length remains constant. The model of the beam-end specimen is used to study the effects of deformation height, deformation face angle, concrete cover, lead length (unbonded portion of the embedded length), embedded length, and confinement provided by stirrups on steel-concrete bond.

4.2 Observations and Conclusions

The results of the finite element studies outlined in this report support the following conclusions.

1). Steel-concrete interaction can be accurately represented by placing interface elements only on the compression faces of the ribs.

2). Under conditions in which the rib height is increased, the slip at the peak load decreases while little or no change in the peak load is observed.

3). Bars with multi-angle rib faces and bars with 45° rib faces provide nearly identical bond strength. The amount of slip at the peak load for the bars with multi-angle rib faces, however, is greater compared to the bars with 45° rib faces. This increase in slip appears to be caused by compression of the interface elements.

4). Under conditions of increased cover, bond force and slip at the peak load increase in all cases.

5). Under conditions of increased lead length, an increase in bond force is observed. The increase in bond strength results from the additional concrete through which the splitting crack must be driven in order to fail the specimen.

6). Under conditions of increased embedded length, bond force at the peak load increases.

7). The amount of concrete that is split at the peak load is not proportional to the embedded length. By doubling the embedded length, the amount of concrete that is split at the peak load does not double. This observation may help explain why bars with low embedded

lengths can have substantial bond strength and why bond strength does not increase proportionally with embedded length.

8). Lateral displacements measured at the front face of the specimen are not dependent on rib height or rib shape up to the peak load, consistent with the recent findings at the University of Kansas (Darwin et al. 1993). Lateral displacements are, however, dependent on concrete cover. Once the peak load has been reached, lateral displacements increase with an increase in rib height.

9). Using a statical model of steel-concrete bond, the clamping force provided by the concrete can be easily related to the pull-out force of the reinforcing bar.

10). Under conditions in which bar confinement is provided by transverse reinforcement, bond strength increases compared to the bond strength of bars with no transverse reinforcement. The increase in bond strength is greater for bars with greater rib height. However, in the models with transverse reinforcement, a provision for allowing concrete near the ribs to crush under load should provide a more accurate representation of the load-slip behavior.

4.3 Recommendations for Further Study

This report describes the application of the finite element method to model the behavior of experimental beam-end specimens. While the current finite element study has addressed several important points associated with steel-concrete bond, this analysis does not answer all questions of how deformation pattern affects bond strength. The following list offers suggestions related to the bond of reinforcing steel to concrete that were not addressed in this study, but could be applied in future finite element studies.

1). The current models use a value for the coefficient of friction for reinforcing bars used in earlier finite element studies at the University of Kansas (Choi et al. 1990, 1991; Hadje-Ghaffari et al. 1991). The model may be modified by using a more realistic (higher) value for μ.

2). The fracture energy used in this study is high compared to most test data. Additional studies using lower values of fracture energy should be considered.

3). The steel bar in the current study appears to provide the necessary wedging action required to split the concrete, despite the fact that the bar is square. However, the square bar may not provide the same mechanical interaction produced by a round bar. In future studies, the model may be modified to include a round bar.

4). Currently, the finite element mesh is too coarse to accurately study the stresses in the concrete near the ribs. Also, the concrete in the study remains linear elastic throughout the analysis. Provisions need to be included to allow for crushed concrete surrounding the ribs, especially in those cases involving transverse reinforcement.

5). The center-to-center spacing of the deformations in the current model was constant for all analyses. To provide a better picture of the effects of deformation pattern on bond, the model should be changed to include rib spacings as a variable.

6). Darwin and Graham (1993) investigated the effects of relative rib area, R_r, on bond strength under conditions of increased confinement of the bar using a simultaneous increase in cover and lead length. A similar comparison involving the finite element model would be helpful in studying how R_r effects bond strength.

7). Splitting concrete in the current model is constrained to occur only along the specimen center line. However, in experimental tests (Darwin and Graham 1993), other cracking patterns are observed. Additional crack rod elements can be added to allow a wider range of cracking patterns to be represented by the model.

8). Experimental tests have shown that the effect of deformation pattern is more pronounced when the specimen is confined with transverse reinforcement (Darwin and Graham 1993). The current study involves minimal use of transverse reinforcement. Additional variables that need to be studied in cases with transverse reinforcement include the effects of concrete cover, rib shape, lead length, and especially amount of transverse reinforcement and embedded length.

REFERENCES

Abrams, D.A. (1913). "Tests of Bond between Concrete and Steel," *Bulletin* No. 71, Engineering Experiment Station, University of Illinois, Urbana, IL, 105 pp.

ACI Committee 446. (1991). "Fracture Mechanics of Concrete: Concepts, Models and Determination of Material Properties (ACI 446.1R-91)," American Concrete Institute, Detroit, MI, 145 pp.

ASTM A 615-90. "Standard Specification for Deformed and Plain Billet-Steel Bars for Concrete Reinforcement," *1992 Annual Book of ASTM Standards*, Vol. 1.04, American Society for Testing and Materials, Philadelphia, PA, pp. 389-392.

Barsom, John and Rolfe, Stanley. (1987). *Fracture and Fatigue Control in Structures*, 2nd Edition, Prentice-Hall, pp. 30-38.

Bazant, Z.P. and Oh, Byung H. (1983). "Crack Band Theory for Fracture of Concrete," *Materiaux et Constructions*, Vol. 16, No. 93, May-June, pp. 155-177.

Bazant, Z.P. and Sener, S. (1988). "Size Effect in Pull-out Tests," *ACI Materials Journal*, Vol. 85, No. 6, Sep.-Oct., pp. 347-351.

Brettmann, Barrie B; Darwin, David; and Donahey, Rex C. (1984). "Effect of Superplasticizers on Concrete-Steel Bond Strength," *SL Report* 84-1, University of Kansas Center for Research, Lawrence, Kansas, April, 32 pp.

Brettman, Barrie B; Darwin, David; and Donahey, Rex C. (1986). "Bond of Reinforcement to Superplasticized Concrete, " ACI Journal, *Proceedings* Vol. 83, No. 1, Jan.-Feb., pp. 98-107.

Cedolin, Luigi and Dei Poli, Sandro. (1977). "Finite Element Studies of Shear-Critical R/C Beams," *Journal of Engineering Mechanics Division*, ASCE, Vol. 103, No. EM-3, June, pp. 395-410.

Chinn, J.; Ferguson, P.M.; and Thompson, J.N. (1955). "Lapped Splices in Reinforced Concrete Beams," ACI Journal, *Proceedings* Vol. 52, No. 2, October, pp. 201-214.

Choi, Oan Chul; Darwin, David; and McCabe, Steven L. (1990). "Bond Strength of Epoxy-Coated Reinforcement to Concrete," *SM Report* No. 25, University of Kansas Center for Research, Lawrence, Kansas, July, 217 pp.

Choi, Oan Chul; Hadje-Ghaffari, Hossain; Darwin, David; and McCabe, Steven L. (1991). "Bond of Epoxy-coated Reinforcement: Bar Parameters," *ACI Materials Journal*, Vol. 88, No. 2, March-April, pp. 207-217.

Clark, A. P. (1946). "Comparative Bond Efficiency of Deformed Concrete Reinforcing Bars," ACI Journal, *Proceedings* Vol. 43, No. 4, December, pp. 381-400.

Clark, A. P. (1949). "Bond of Concrete Reinforcing Bars," ACI Journal, *Proceedings* Vol. 46, No. 3, November, pp. 161-184.

Darwin, David; McCabe, Steven L.; Idun, Emmanuel K.; and Tholen, Michael. (1993). Unpublished experimental study of beam-end specimens. University of Kansas.

Darwin, David and Graham, Ebenezer. (1993). "Effects of Deformation Height and Spacing on Bond Strength of Reinforcing Bars," *SL Report* No. 93-1, University of Kansas Center for Research, Inc., Lawrence, Kansas, January, 68 pp.

Darwin, D.; McCabe, S. L.; Idun, E. K.; and Schoenekase, S. P. (1992a). "Development Length Criteria: Bars without Transverse Reinforcement," *SL Report* 92-1, University of Kansas Center for Research, Inc., Lawrence, Kansas, April, 62 pp.

Darwin, D.; McCabe, S. L.; Idun, E. K.; and Schoenekase, S. P. (1992b). "Development Length Criteria: Bars Not Confined by Transverse Reinforcement," *ACI Structural Journal*, Vol. 89, No. 6, Nov.-Dec., pp. 709-720.

Desai, C.S. and Nagaraj, B.K. (1988). "Modeling for Cyclic Normal and Shear Behavior of Interfaces," *Journal of Engineering Mechanics*, ASCE, Vol. 114, No. 7, July, pp. 1198-1217.

Ferguson, Phil M. and Thompson, J. Neils. (1962). "Development Length of High Strength Reinforcing Bars in Bond," ACI Journal, *Proceedings* Vol. 59, No. 7, July, pp. 887-927.

Ferguson, P.M. and Thompson, J. Neils. (1965). "Lapped Splices for High Strength Reinforcing Bars," ACI Journal, *Proceedings* Vol. 62, No. 9, September, pp. 1063-1078.

Gerstle, Walter H. and Xie, Ming. (1992). "FEM Modeling of Fictitious Crack Propagation in Concrete," *Journal of Engineering Mechanics*, ASCE, Vol. 118, No. 2, February, pp. 416-434.

Gibbs, N.E.; Poole, W.G.; and Stockmeyer, P.K. (1976). "An Algorithm for Reducing the Bandwidth of Matrices," *Sparce Matrices and Their Applications; SIAM Journal of Numerical Analysis*, Vol. 13, No. 2, pp. 236-250.

Goto, Y. (1971). "Cracks Formed in Concrete Around Deformed Tension Bars," ACI Journal, *Proceedings*, Vol. 68, No. 4, April, pp. 244-251.

Gylltoft, K. (1989). "Fracture Mechanics Applied to Bond Failure in Pull-out Tests," *RILEM-Fracture Mechanics of Concrete Structures--From Theory to Applications*, Stockholm, pp. 258-262.

Hadje-Ghaffari, Hossain; Darwin, David; and McCabe, Steven L. (1991). "Effects of Epoxy Coating on Bond of Reinforcement to Concrete," *SM Report* No. 28, University of Kansas Center for Research, Inc., Lawrence, Kansas, July, 288 pp.

Hillerborg, A.; Modeer, M.; and Petersson, P. E. (1976). "Analysis of Crack Formation and Crack Growth in Concrete by Means of Fracture Mechanics and Finite Elements," *Cement and Concrete Research*, Vol. 6, No. 6, Nov., pp. 773-782.

Ingraffea, A.R.; Gerstle, W.H.; Gergely, P.; and Saouma, V. (1984). "Fracture Mechanics of Bond in Reinforced Concrete," *Journal of Structural Engineering*, ASCE, Vol. 110, No. 4, April, pp. 871-890.

Jimenez, Rafael; Gergely, Peter; and White, Richard N. (1978). "Shear Transfer Across Cracks in Reinforced Concrete," Department of Structural Engineering, Cornell University, Ithaca, NY, August, 35 pp.

Johnston, David W., and Zia, Paul. (1982). "Bond Characteristics of Epoxy Coated Reinforcing Bars," *Report* No. FHWA-NC-82-002, Federal Highway Administration, Washington, DC, 163 pp.

Kemp, E.L. and Wilhelm, W.J. (1979). "Investigation of the Parameters Influencing Bond Cracking," ACI Journal, *Proceedings* Vol. 76, No. 1, Jan., pp. 47-71.

Keuser, M. and Mehlhorn, G. (1987). "Finite Element Model for Bond Problems," *Journal of Structural Engineering*, ASCE, Vol. 113, No. 10, October, pp. 2160-2173.

Kimura, Hideka, and Jirsa, James O. (1992). "Effects of Bar Deformation and Concrete Strength on Bond of Reinforcing Steel to Concrete," PMFSEL *Report* No. 92-4, Phil M. Ferguson Structural Engineering Laboratory, University of Texas at Austin, Sep., 78 pp.

Leibengood, L.; Darwin, D.; and Dodds, R. H. (1984). "Finite Elements Analysis of Concrete Fracture Specimens," *SM Report* No. 11, University of Kansas Center for Research, Inc., Lawrence, KS, May, 120 pp.

Leibengood, L.; Darwin, D.; and Dodds, R. H. (1986). "Parameters Affecting Finite Element Analysis of Concrete Structures," *Journal of Structural Engineering*, Vol. 112, No. 2, February, pp. 326-341.

Lopez, L. A.; Dodds, R. H. Jr.; Rehak, D. R.; and Schmidt, R. J. (1992). *Polo-Finite: A Structural Mechanics System for Linear and Nonlinear Analysis.* A technical report by the University of Illinois at Urbana-Champaign.

Losberg, Anders, and Olsson, Per-Ake. (1979). "Bond Failure of Deformed Reinforcing Bars Based on Longitudinal Splitting Effect of the Bars," ACI Journal, *Proceedings* Vol. 76, No. 1, Jan., pp. 5-18.

Lutz, L. A.; Gergely, P.; and Winter, G. (1966). "The Mechanics of Bond and Slip of Deformed Reinforcing Bars in Concrete," *Report* No. 324, Department of Structural Engineering, Cornell University, August, 306 pp.

Lutz, L.A., and Gergely, P. (1967). "Mechanics of Bond and Slip of Deformed Bars in Concrete," ACI Journal, *Proceedings* Vol. 64, No. 11, Nov., pp. 711-721.

Lutz, L.A. (1970). "Analysis of Stresses in Concrete Near a Reinforcing Bar Due to Bond and Transverse Cracking," ACI Journal, *Proceedings* Vol. 67, Detroit, MI, pp. 778-787.

Masaki, M.; Shunsuke, O.; and Hiroyuki, A. (1991). "Bond Splitting Strength in Reinforced Concrete Members," *Transactions of the Japan Concrete Institute*, Vol. 13, pp. 581-588.

Mazars, Jacky; Pijaudier-Cabot, Gilles; and Pulikowski, Jacek. (1989). "Steel-Concrete Bond Analysis with Non-Local Continuous Damage." *Report* No. 96, Laboratoire de Mechanique et Technologie, Universite Paris, 35 pp.

McCabe, S.L.; Darwin, D.; Choi, O.C.; and Hadje-Ghaffari, H. (1992). "Application of Fracture Mechanics to Steel-Concrete Bond Analysis," *Concrete Design Based on Fracture Mechanics* (ACI SP-134), American Concrete Institute, Detroit, MI, pp. 101-114.

Menzel, Carl A. (1939). "Some Factors Influencing Results of Pull-Out Bond Tests," ACI Journal, *Proceedings* Vol. 35, No. 10, June, pp. 517-542.

Menzel, Carl A. (1952). "Effect of Settlement of Concrete on Results of Pullout Tests," *Research Department Bulletin* 41, Research and Development Laboratories of the Portland Cement Association, Nov., 49 pp.

Niwa, Junichiro. (1991). Unpublished finite element study of beam-end specimens. University of Kansas.

Orangun, C.O.; Jirsa, J.O.; and Breen, J.E. (1975). "The Strength of Anchored Bars: A Reevaluation of Test Data on Development Length and Splices," *Research Report* No. 154-3F, Center for Highway Research, Univ. of Texas at Austin, Jan., 78 pp.

PATRAN-II Modeling Software. PDA Engineering, 1560 Brookhollow Drive, Santa Ana, CA 92705.

Petersson, P. E. (1979). "Fracture Energy of Concrete: Method of Determination," *Cement and Concrete Research*, Vol. 10, No. 1, January, pp. 78-89.

Petersson, P. E. (1981). "Crack Growth and Development of Fracture Zones in Plain Concrete and Similar Materials," *Report* TVBM-1006, Div. of Bldg. Materials, University of Lund, Sweden, 174 pp.

Rehm, G. (1957). "The Fundamental Law of Bond," *Proceedings* Symposium on Bond and Crack Formation in Reinforced Concrete (Stockholm, RILEM, Paris, (published by Tekniska Hogskolans Rotaprinttrychkeri, Stockholm, 1958).

Rehm, G. (1961). "Uber die Grunlagen des Verbundes Zwischen Stahl und Beton." *Deutscher Ausschuss fur Stahlbeton.* No. 1381, pp. 59, (C&CA Library Translation No. 134, 1968. "The Basic Principle of the Bond between Steel and Concrete.").

Rots, J.G. (1988). "Computational Modeling of Concrete Fracture," Dissertation, Delft University of Technology, Dept. of Civil Engineering, Delft, 132 pp.

Rots, J.G. (1989). "Bond of Reinforcement," *RILEM-Fracture Mechanics of Concrete Structures--From Theory to Applications*, Stockholm, pp. 245-250.

Saouma, Victor. (1980). "Automated Nonlinear Finite Element Analysis of Reinforced Concrete: A Fracture Mechanics Approach," Ph.D. Thesis, Cornell University, Ithaca, NY.

Skorbogatov, S.M., and Edwards, A.D. (1979). "The Influence of the Geometry of Deformed Steel Bars on Their Bond Strength in Concrete," *The Institute of Civil Engineers*, Proceedings, Vol. 67, Part 2, June, pp. 327-339.

Soretz, S., and Holzenbein, H. (1979). "Influence of Rib Dimensions of Reinforcing Bars on Bond and Bendability," ACI Journal, *Proceedings* Vol. 76, No. 1, Jan., pp. 111-127.

Treece, Robert A. and Jirsa, James O. (1989). "Bond Strength of Epoxy-Coated Reinforcing Bars," *ACI Materials Journal*, Vol. 86, No. 2, Mar.-Apr., pp. 167-174.

Wilhelm, W.J.; Kemp, E.L.; and Lee, Y.T. (1971). "Influence of Deformation Height and Spacing on the Bond Characteristics of Steel Reinforcing Bars," *Civil Engineering Report* No. 2013, West Virginia Univ., 1971.

Table 2.1 Finite Element Models--1/2 in. Lead Lengths

EMBED. LENGTH* (No. of Ribs)	SUBSTRUCTURE	1 in. Cover		2 in. Cover		3 in. Cover	
		No. of Nodes	No. of Elements	No. of Nodes	No. of Elements	No. of Nodes	No. of Elements
0.82 in.							
(1 RIB)	concrete	1620	1194	1860	1390	1980	1488
	rein. steel	210	80	210	80	210	80
	crack rods	220	220	260	260	280	280
	interface	10	10	10	10	10	10
	total	2060	1504	2340	1740	2480	1858
1.44 in.							
(2 RIBS)	concrete	1743	1290	2001	1502	2130	1608
	rein. steel	230	88	230	88	230	88
	crack rods	231	231	273	273	294	294
	interface	20	20	20	20	20	20
	total	2224	1629	2524	1883	2674	2010
2.10 in.							
(3 RIBS)	concrete	1771	1325	2033	1543	2164	1652
	rein. steel	240	92	240	92	240	92
	crack rods	231	231	273	273	294	294
	interface	30	30	30	30	30	30
	total	2272	1678	2576	1938	2728	2068
4.02 in.							
(6 RIBS)	concrete	2288	1761	2626	2051	2795	2196
	rein. steel	320	124	320	124	320	124
	crack rods	286	286	338	338	364	364
	interface	60	60	60	60	60	60
	total	2954	2231	3344	2573	3539	2744
7.86 in.							
(12 RIBS)	concrete	3998	3147	4588	3665	4883	3924
	rein. steel	560	220	560	220	560	220
	crack rods	484	484	572	572	616	616
	interface	120	120	120	120	120	120
	total	5162	3971	5840	4577	6179	4880

* includes 1/2 in. lead length

Table 2.2 Finite Element Models--Multi-angle Rib Faces

EMBED. LENGTH* (No. of Ribs)	SUBSTRUCTURE	1 in. Cover		2 in. Cover		3 in. Cover	
		No. of Nodes	No. of Elements	No. of Nodes	No. of Elements	No. of Nodes	No. of Elements
0.82 in.							
(1 RIB)	concrete	1500	1103	1722	1285	1833	1376
	rein. steel	210	80	210	80	210	80
	crack rods	198	198	234	234	252	252
	interface	20	20	20	20	20	20
	total	1928	1401	2186	1619	2315	1728
1.44 in.							
(2 RIBS)	concrete	2059	1552	2363	1808	2515	1936
	rein. steel	290	112	290	112	290	112
	crack rods	253	253	299	299	322	322
	interface	40	40	40	40	40	40
	total	2642	1957	2992	2259	3167	2410
2.10 in.							
(3 RIBS)	concrete	2107	1613	2417	1879	2572	2012
	rein. steel	300	116	300	116	300	116
	crack rods	231	231	273	273	294	294
	interface	60	60	60	60	60	60
	total	2698	2020	3050	2328	3226	2482

* includes 1/2 in. lead length

Table 2.3 Finite Element Models--2 in. Lead Lengths

EMBED. LENGTH* (No. of Ribs)	SUBSTRUCTURE	2 in. Cover No. of Nodes	No. of Elements
2.32 in. (1 RIB)	concrete	1376	1016
	rein. steel	165	64
	crack rods	204	204
	interface	10	10
	total	1755	1294
2.96 in. (2 RIBS)	concrete	1683	1338
	rein. steel	210	80
	crack rods	234	234
	interface	20	20
	total	2147	1672
3.60 in. (3 RIBS)	concrete	1863	1416
	rein. steel	220	84
	crack rods	247	247
	interface	30	30
	total	2360	1777
5.52 in. (6 RIBS)	concrete	2751	2152
	rein. steel	330	128
	crack rods	351	351
	interface	60	60
	total	3492	2691

* includes 2 in. lead length

Table 3.1 Bond Force (Peak Load) and Corresponding Values of Loaded End Slip for the Finite Element Models in this Study

No. of Ribs	Rib Height (in.)	Lead Length (in.)	1 in. Cover Load (lbs)	1 in. Cover Loaded End Slip (in.)	2 in. Cover Load (lbs)	2 in. Cover Loaded End Slip (in.)	3 in. Cover Load (lbs)	3 in. Cover Loaded End Slip (in.)
1 RIB	0.06	1/2	18146	0.014401	20644	0.021401	24026	0.017401
1 RIB	0.06*	1/2	18436	0.017401	20882	0.018401	23736	0.019901
1 RIB	0.06	2	-	-	25928	0.017401	-	-
1 RIB	0.09	1/2	17886	0.013401	20782	0.013901	23556	0.014901
2 RIBS	0.06	1/2	19188	0.010901	21824	0.011401	24756	0.012301
2 RIBS	0.06*	1/2	19218	0.012401	21620	0.012401	24706	0.013901
2 RIBS	0.06**	1/2	-	-	42143	0.027301	-	-
2 RIBS	0.06	2	-	-	27466	0.012901	-	-
2 RIBS	0.09	1/2	19368	0.009901	21910	0.010401	24892	0.010901
2 RIBS	0.09**	1/2	-	-	43041	0.002359	-	-
3 RIBS	0.06	1/2	19880	0.008901	23034	0.009901	26414	0.010401
3 RIBS	0.06*	1/2	20336	0.010401	23024	0.010401	26500	0.013901
3 RIBS	0.06	2	-	-	29178	0.011401	-	-
3 RIBS	0.09	1/2	20582	0.008901	23254	0.008901	26552	0.009401
6 RIBS	0.06	1/2	24696	0.008601	27730	0.009401	31286	0.009501
6 RIBS	0.06	2	-	-	34632	0.010901	-	-
6 RIBS	0.09	1/2	24992	0.007701	28122	0.008201	32016	0.008201
12 RIBS	0.06	1/2	29516	0.008201	37076	0.009201	41496	0.010101
12 RIBS	0.09	1/2	29700	0.007901	37034	0.008901	41836	0.009501

*indicates bars with multi-angle rib faces

**indicates models with stirrups

Table 3.2 Lateral Displacements at the Front Face of the Model Coinciding with the Peak Loads for the Finite Element Models in this Study

No. of Ribs	Rib Height (in.)	Lead Length (in.)	1 in. Cover Lateral Displacement (in.)	2 in. Cover Lateral Displacement (in.)	3 in. Cover Lateral Displacement (in.)
1 RIB	0.06	1/2	0.003042	0.002754	0.001957
1 RIB	0.06*	1/2	0.003047	0.002759	0.001961
1 RIB	0.06	2	0.00321	0.002826	0.002008
1 RIB	0.09	1/2	0.003127	0.002831	0.002012
2 RIBS	0.06	1/2	0.003743	0.003388	0.002647
2 RIBS	0.06*	1/2	0.003739	0.003382	0.002649
2 RIBS	0.06**	1/2	-	0.006133	-
2 RIBS	0.06	2	0.003745	0.00339	0.002441
2 RIBS	0.09	1/2	0.003873	0.003507	0.002492
2 RIBS	0.09**	1/2	-	0.006242	-
3 RIBS	0.06	1/2	0.003102	0.002808	0.002007
3 RIBS	0.06*	1/2	0.003103	0.002808	0.002006
3 RIBS	0.06	2	0.003107	0.002814	0.002013
3 RIBS	0.09	1/2	0.003174	0.002873	0.002053
6 RIBS	0.06	1/2	0.003273	0.002963	0.002298
6 RIBS	0.06	2	0.003327	0.003012	0.002169
6 RIBS	0.09	1/2	0.003365	0.003046	0.002193
12 RIBS	0.06	1/2	0.003421	0.003097	0.00223
12 RIBS	0.09	1/2	0.003517	0.003184	0.002324

*indicates bars with multi-angle rib faces

**indicates models with stirrups

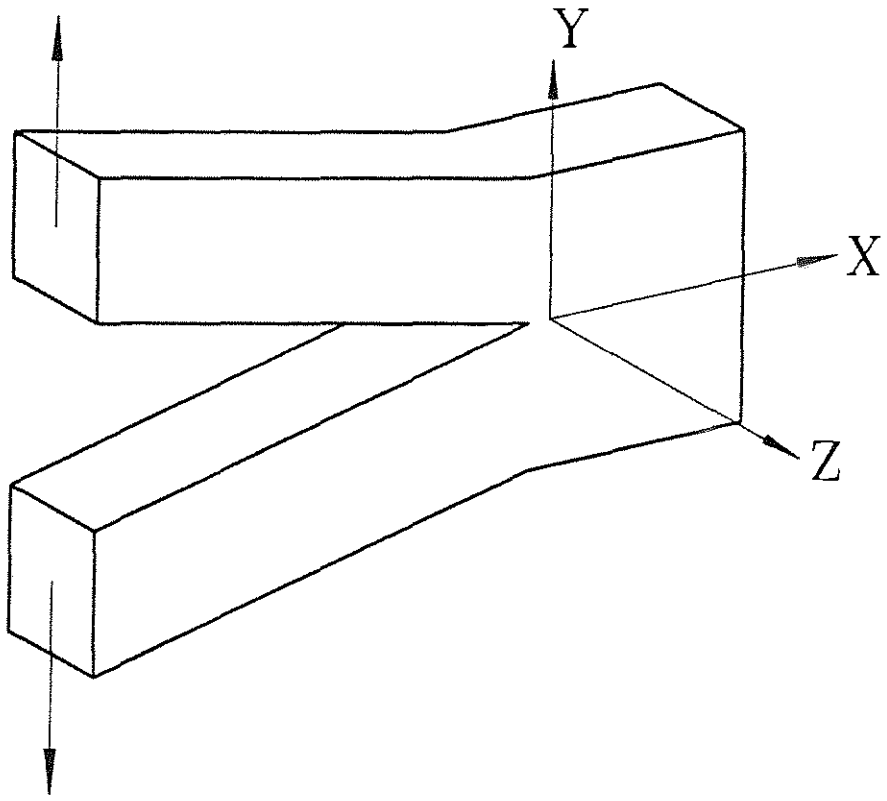

Fig. 1.1 Mode I Crack (after Barsom and Rolfe 1987)

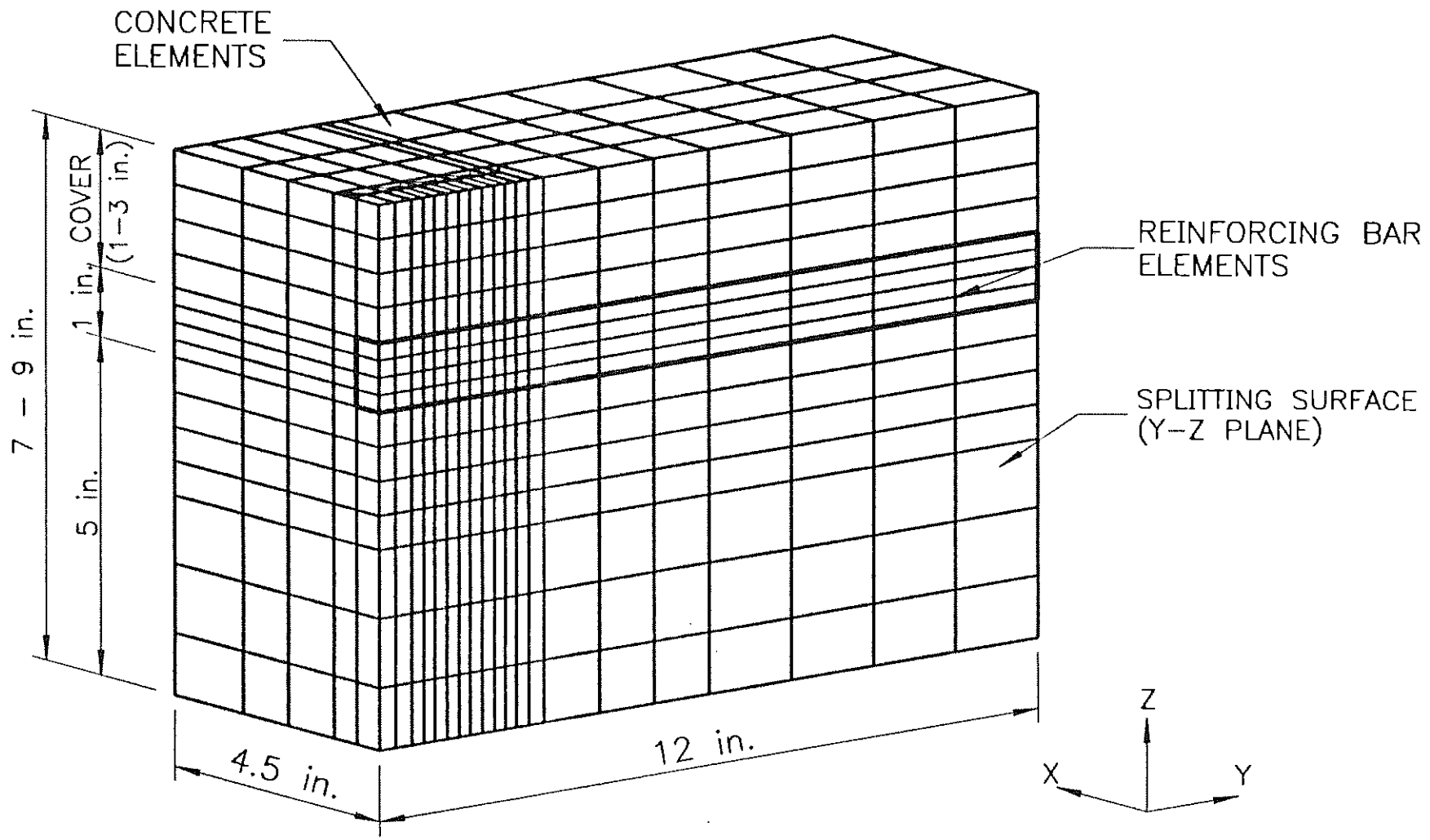

Fig. 2.1 Overall Finite Element Model (Model with 3 Ribs and 1/2 in. Lead Length)

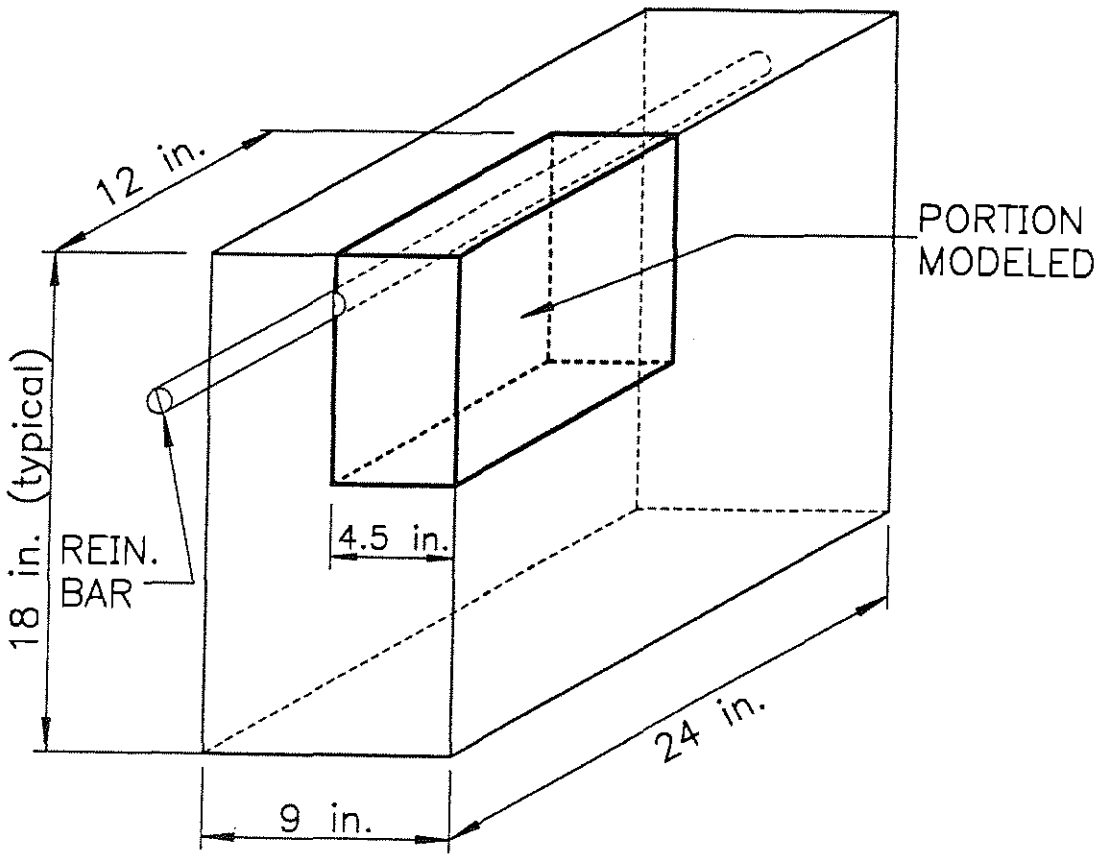

Fig. 2.2 Portion of Experimental Beam-end Specimen Represented by Finite Element Model

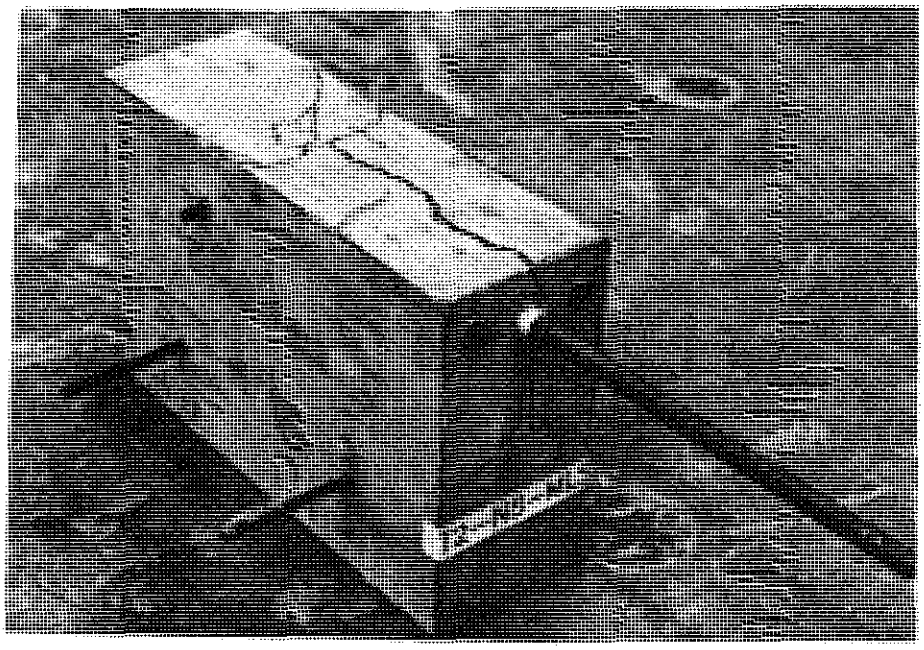

Fig. 2.3 Beam-end Specimen at Failure (Darwin and Graham 1993)

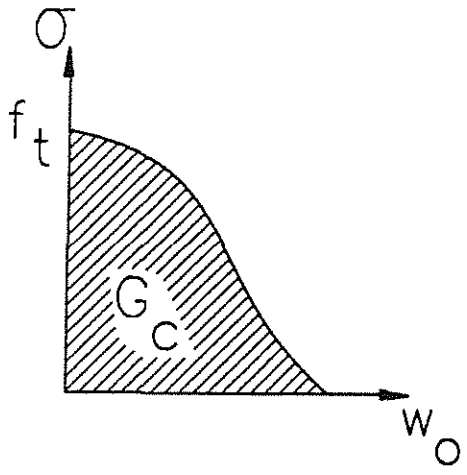

(a)

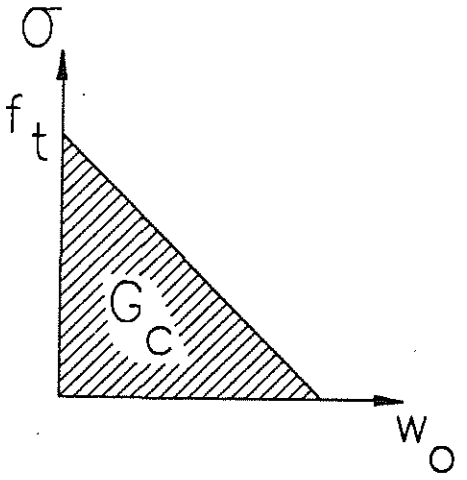

(b)

Fig. 2.4 Representation of Fracture Energy (Petersson 1979)
(a) Crack Opening Stress-displacement Relationship
(b) Straightline Approximation of Crack Opening Stress-displacement Relationship

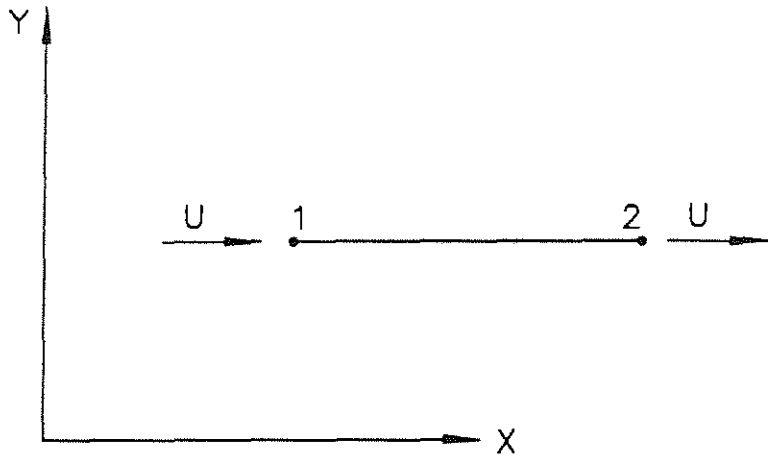

Fig. 2.5 Crack Rod and Stirrup Element (after Lopez et al. 1992)

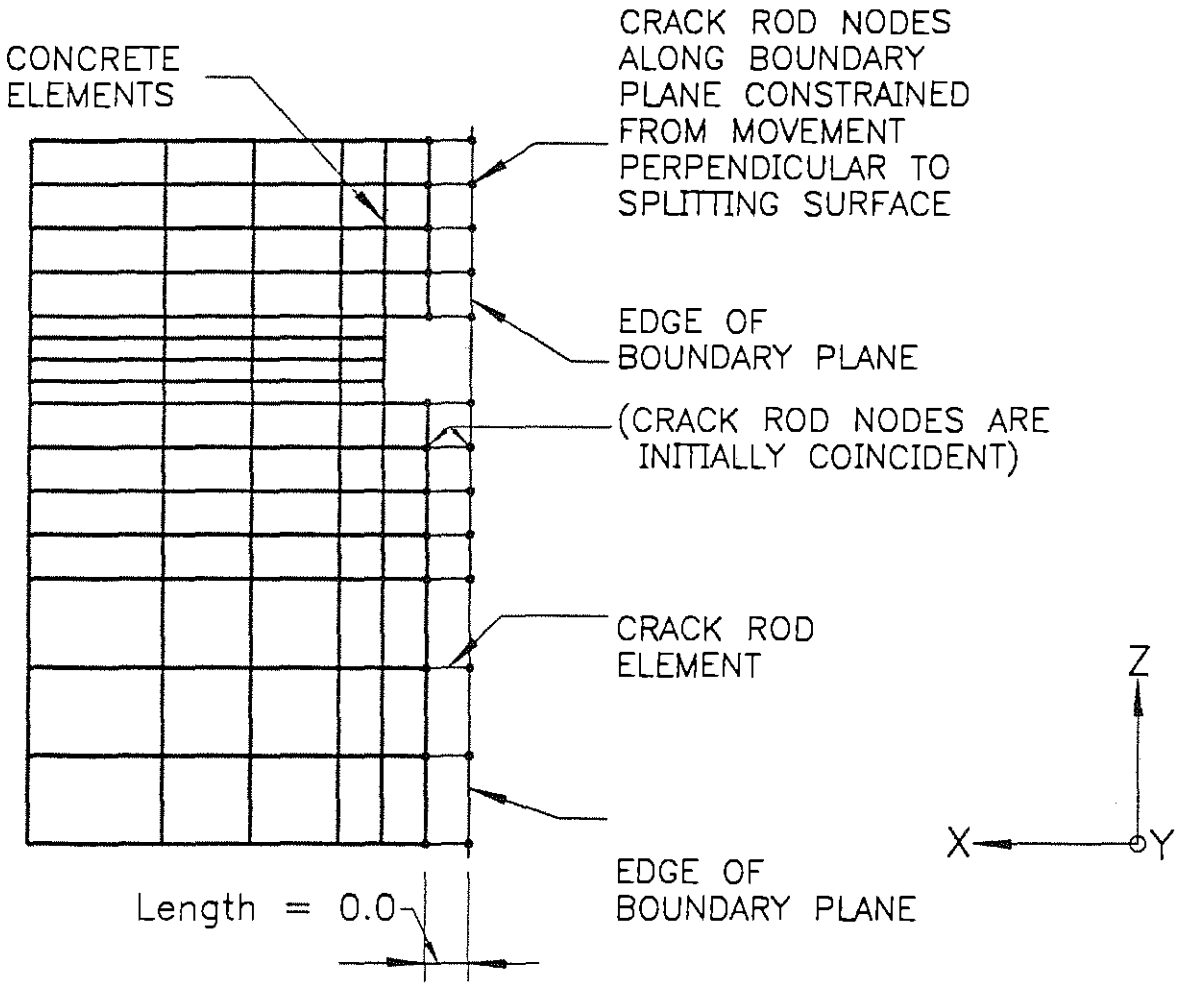

Fig. 2.6 Connection of Crack Rods to Concrete Substructure (End View)

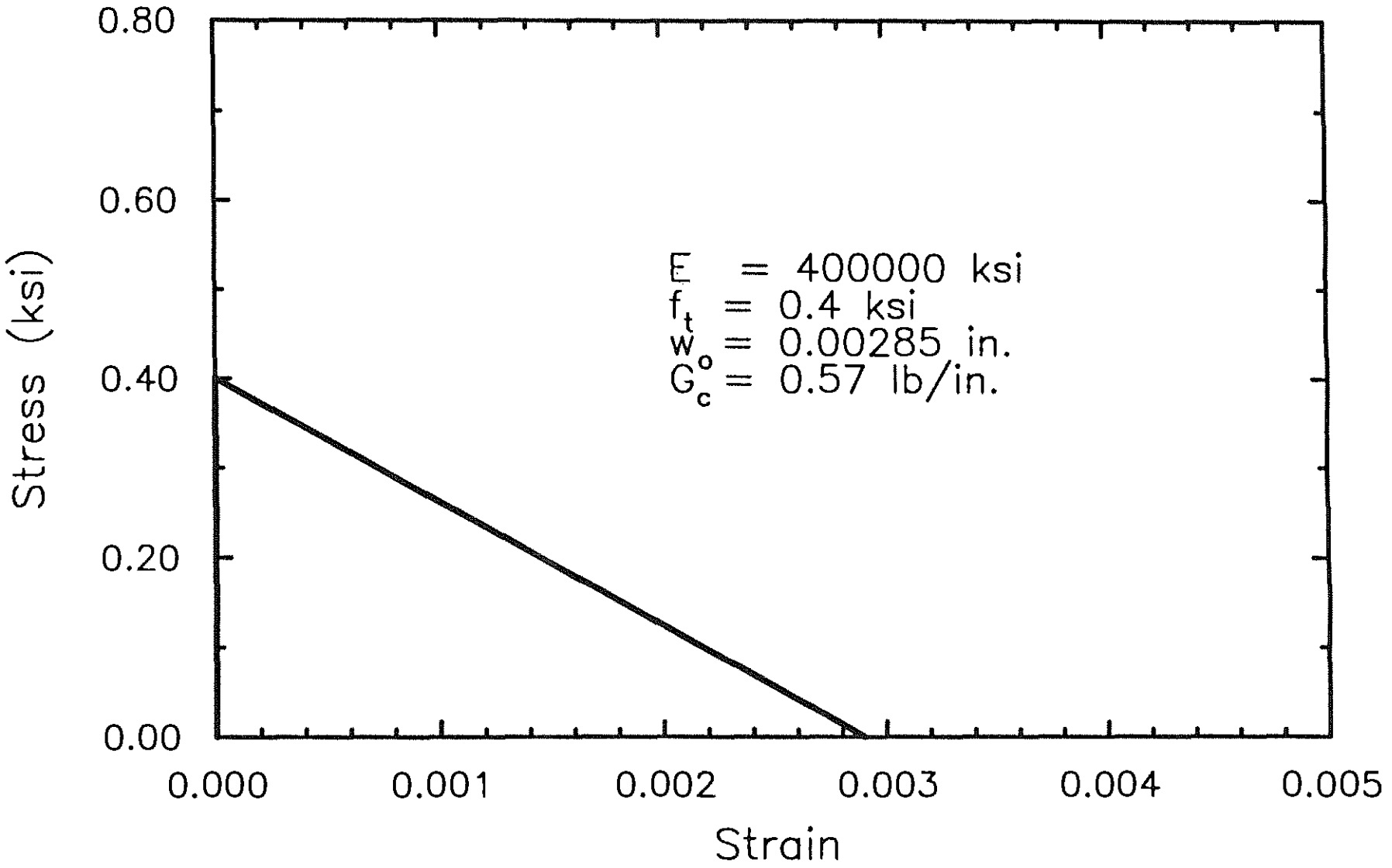

Fig. 2.7 Stress-Strain Curve for Crack Rod Elements

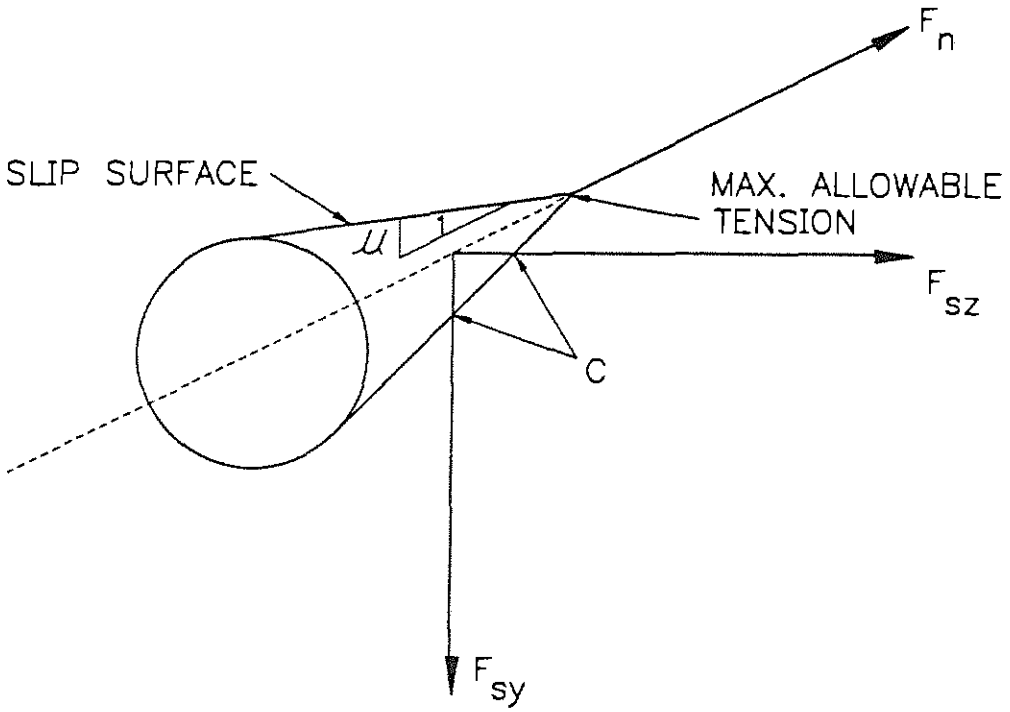

Fig. 2.8 Three-dimensional Mohr-Coulomb Failure Surface (after Lopez et al. 1992)

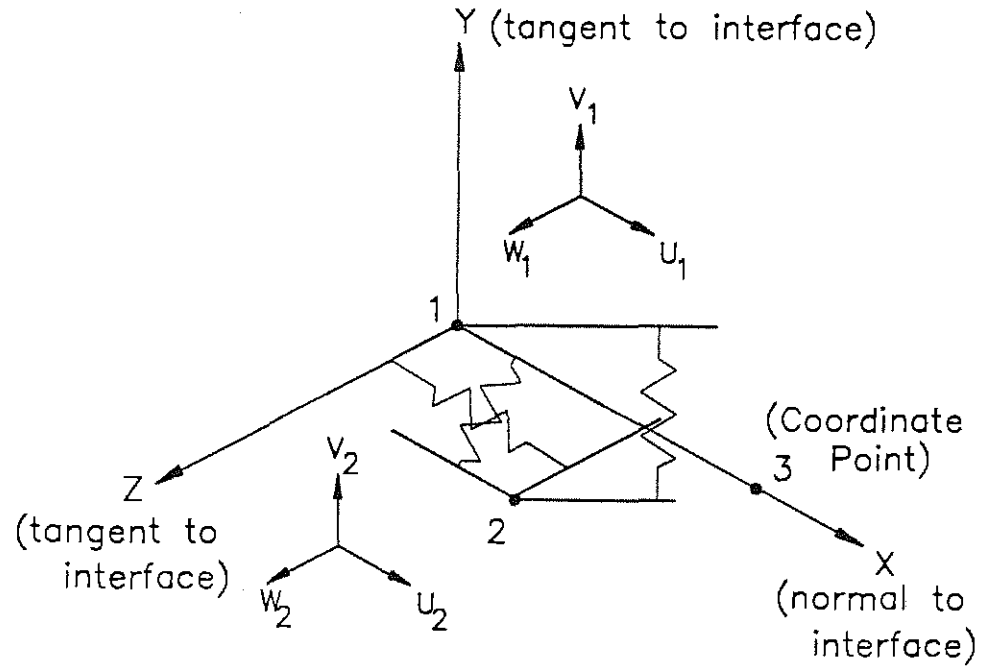

Fig. 2.9 Three-dimensional Link Element (after Lopez et al. 1992)

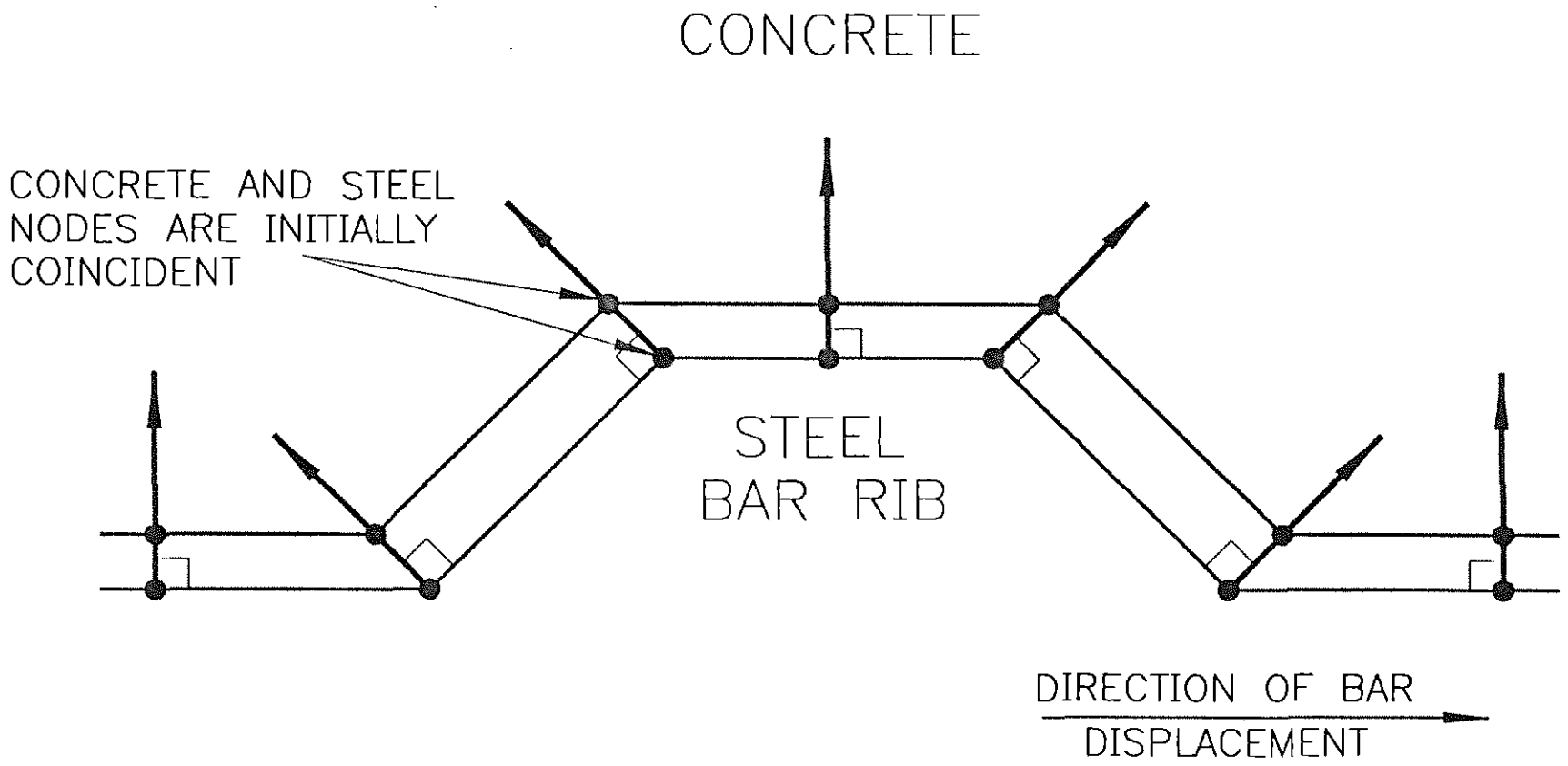

Fig. 2.10 Normal Directions for Interface Link Elements

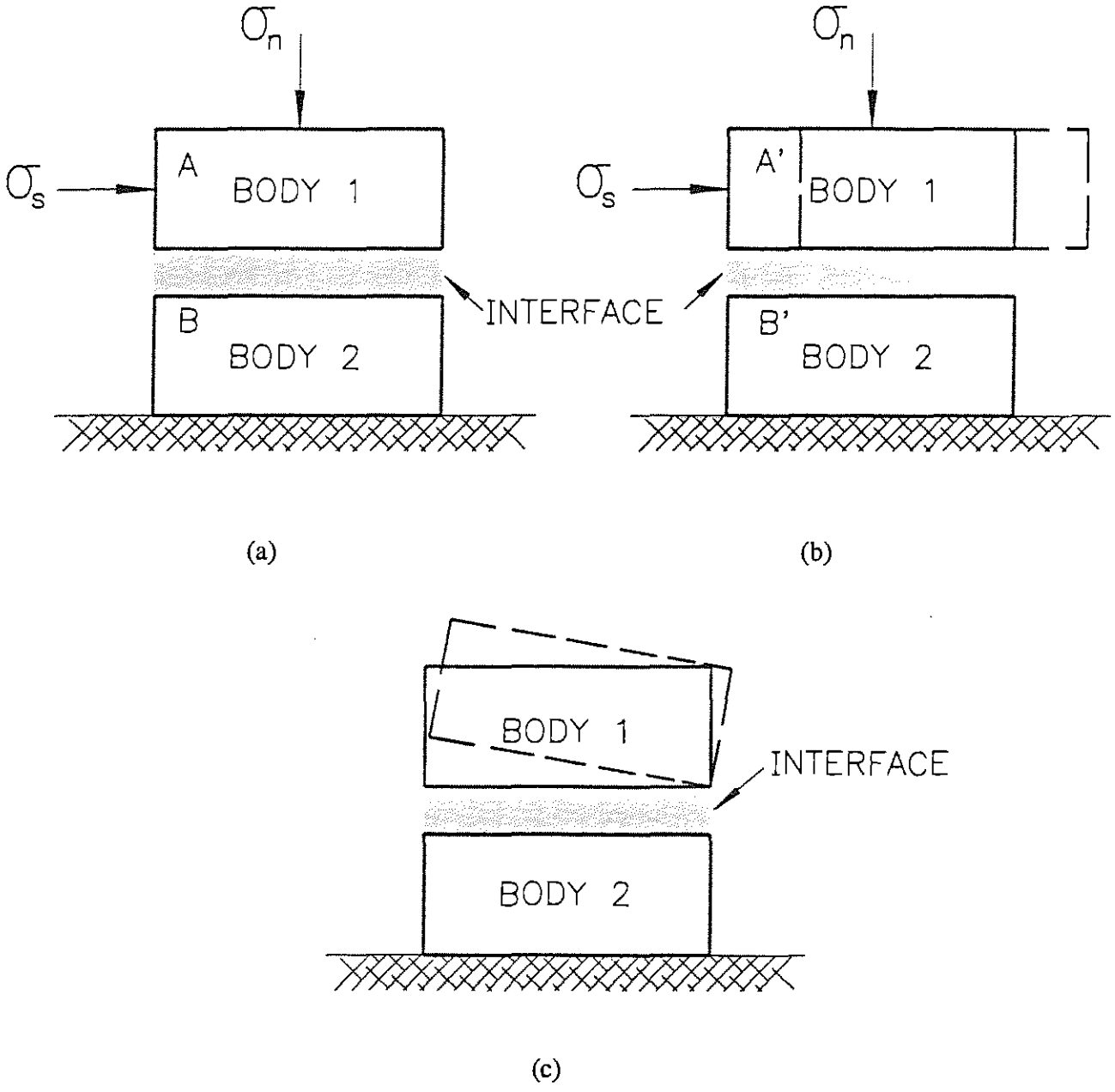

Fig. 2.11 Schematic of Interface Element Material States (after Desai and Nagaraj 1988)
(a) Contact/Stick
(b) Contact/Slip
(c) Separation

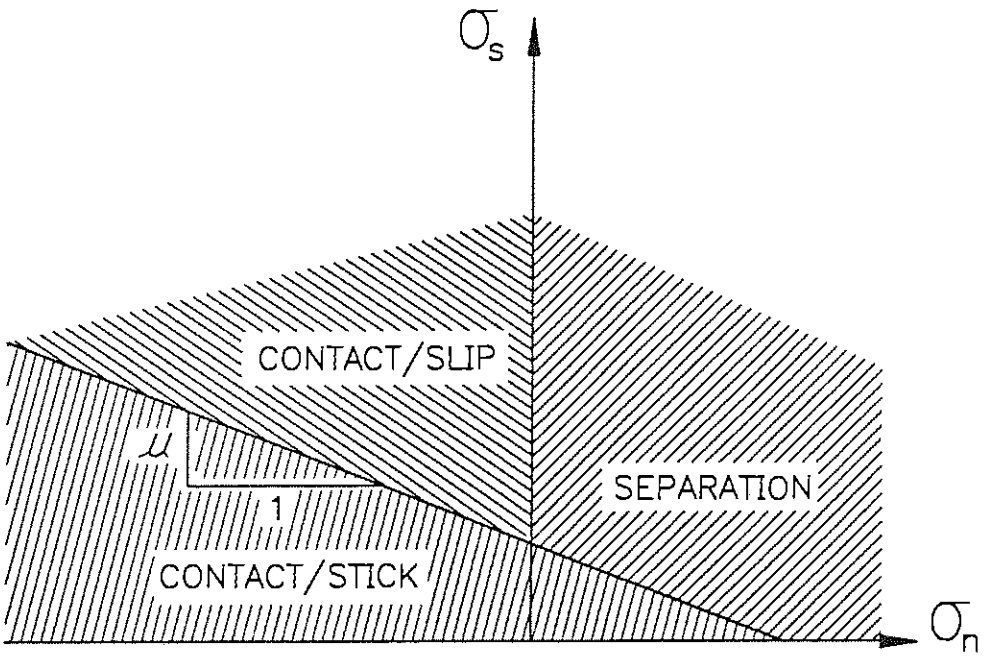

Fig. 2.12 Interface Element Material States on Mohr-Coulomb Surface

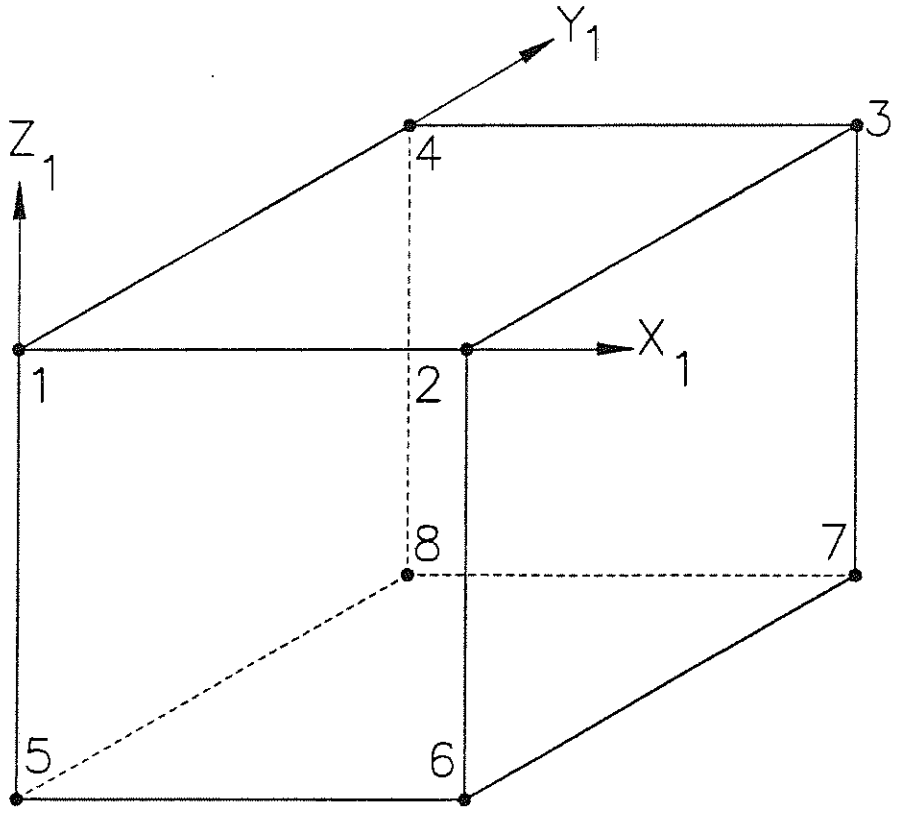

Fig. 2.13 Three-dimensional, 8-node, Linear, Isoparametric Brick Element (after Lopez et al. 1992)

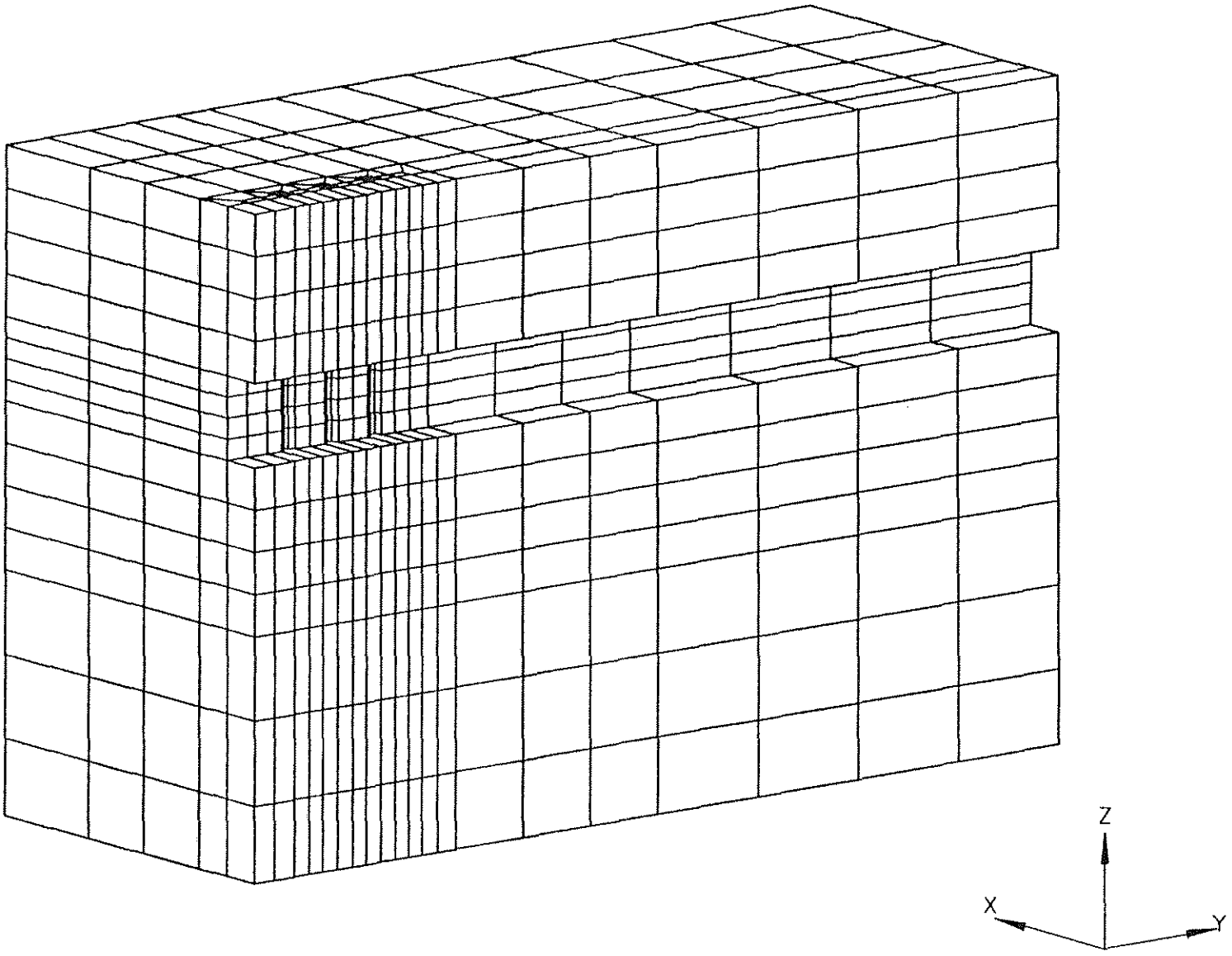

Fig. 2.11 Concrete Substructure (Model with 3 Ribs, 1/2 in. Lead Length, and 2 in. Cover)

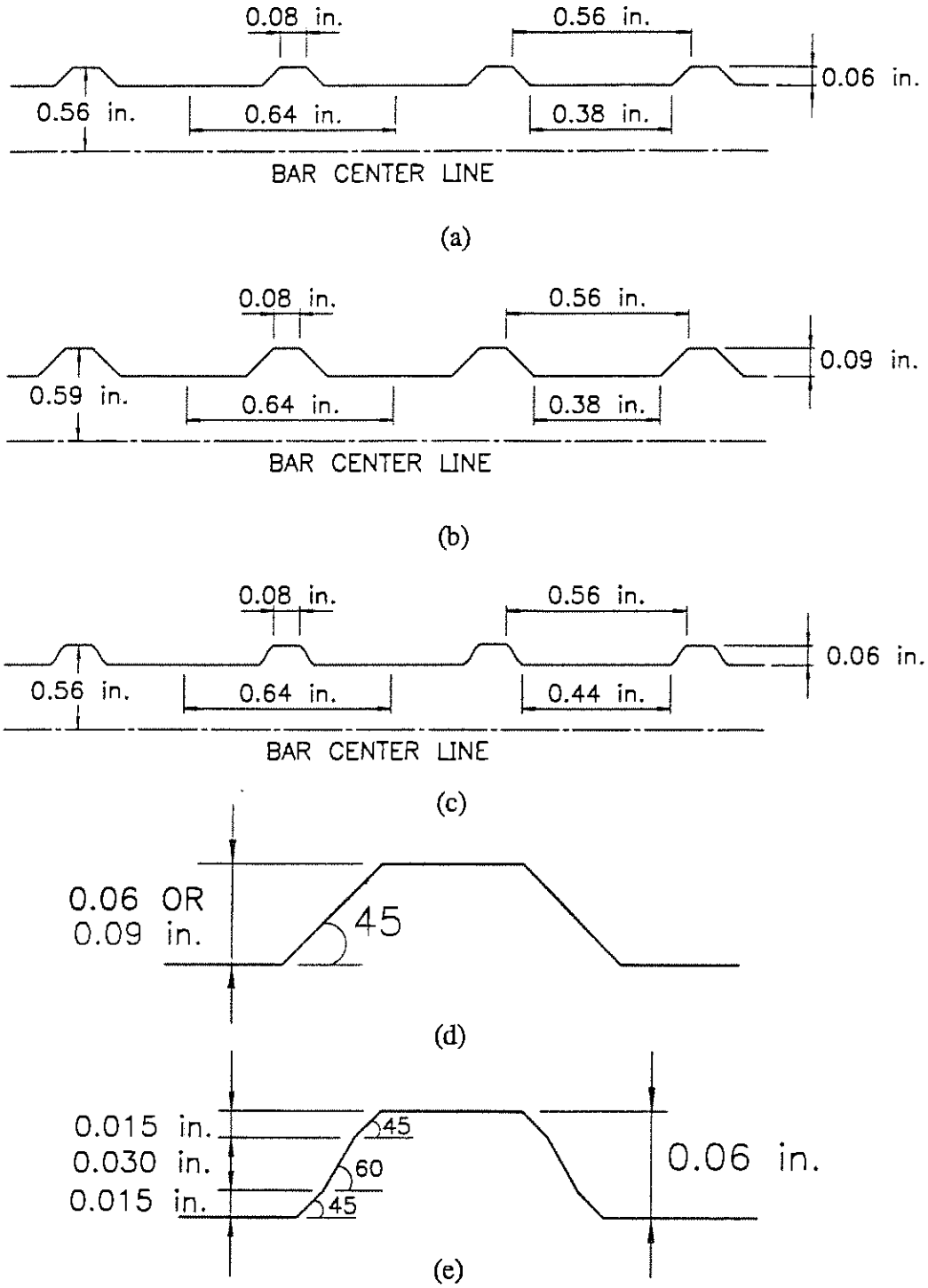

Fig. 2.15 Dimensions of Deformation Patterns Analyzed (Plan View)

(a) Rib Height = 0.06 in.
(b) Rib Height = 0.09 in.
(c) Multi-Angle Rib Face
(d) Detail of Rib Height of 0.06 in. and 0.09 in.
(e) Detail of Multi-Angle Rib Face

Fig. 2.16 Reinforcing Steel Substructure (Model with 3 Ribs and 1/2 in. Lead Length)

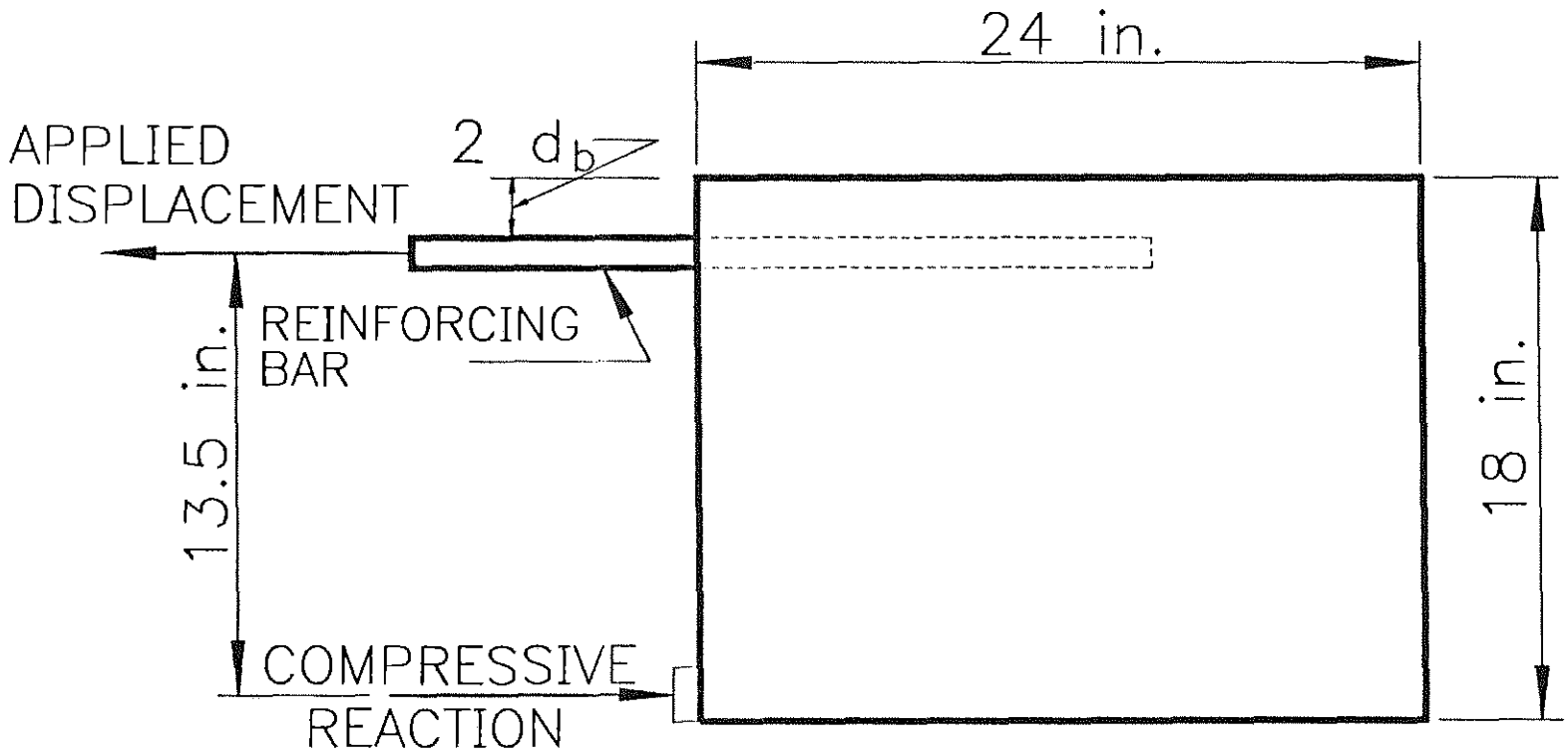

Fig. 2.17 Location of Compressive Reaction on Experimental Beam-end Specimen

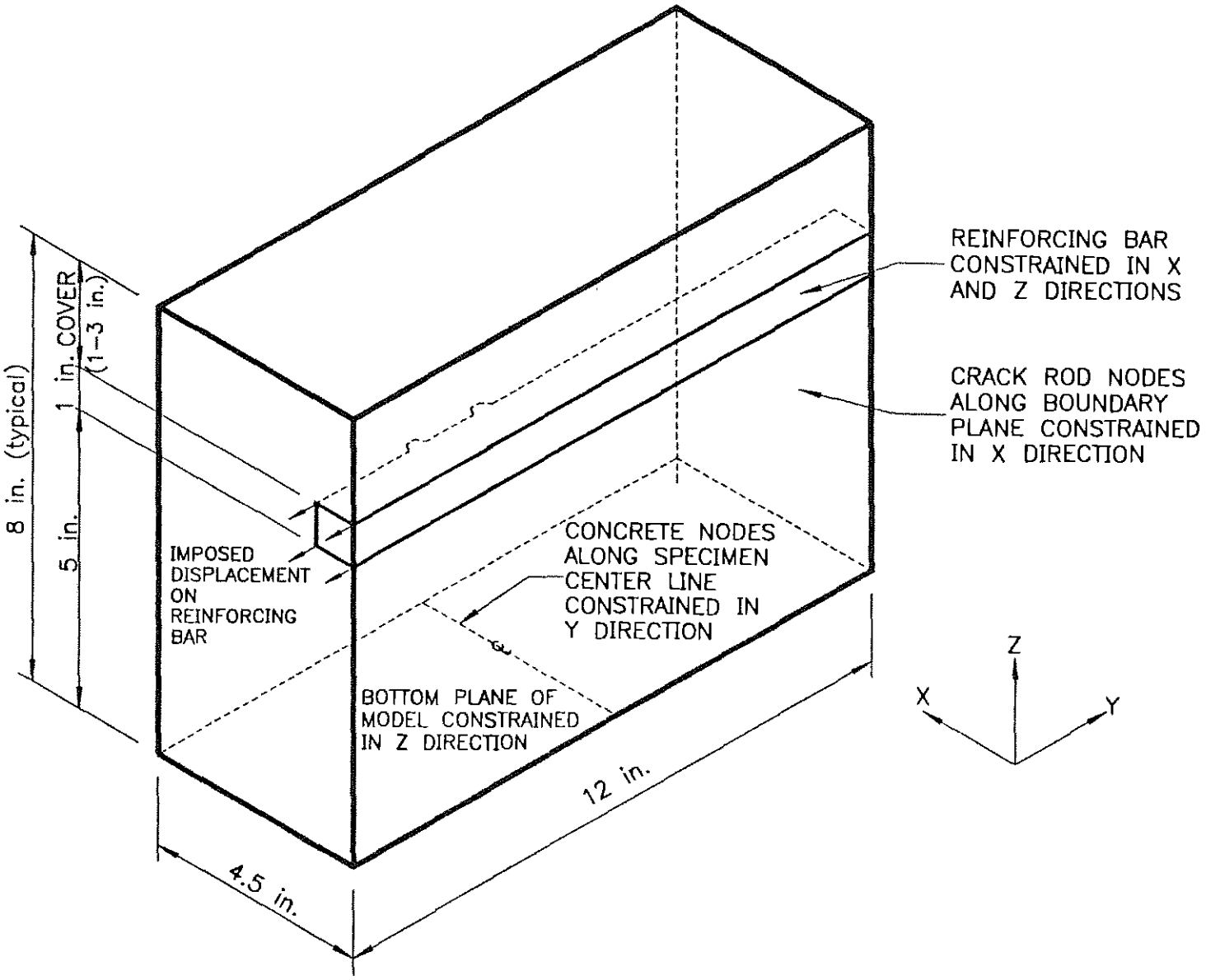

Fig. 2.18 Boundary Conditions on Finite Element Model

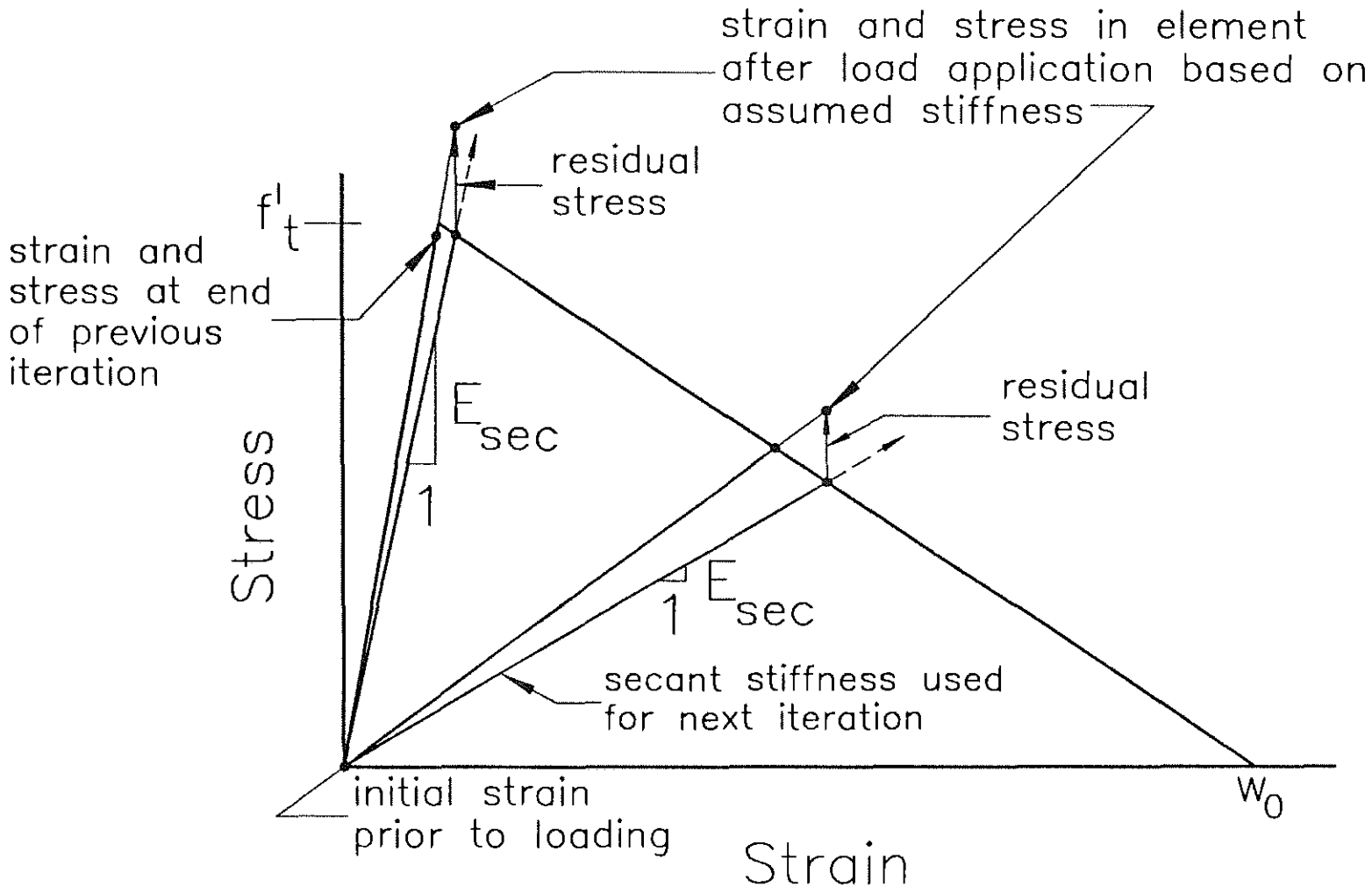

Fig. 2.19 Schematic of Secant Stiffness of Crack Rod Elements

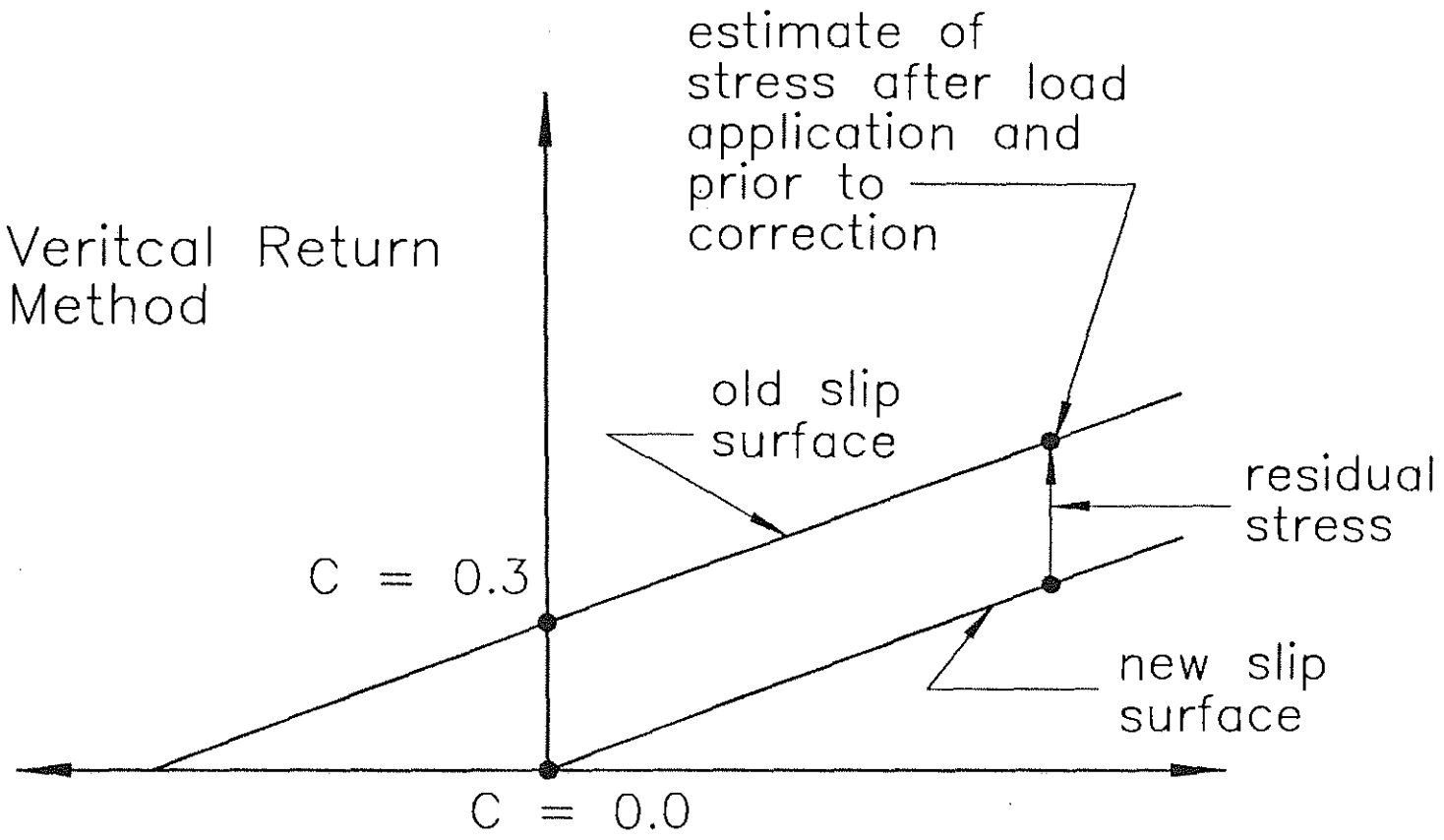

Fig. 2.20 Schematic of Stress Correction Back to Slip Surface (after Lopez et al. 1992)

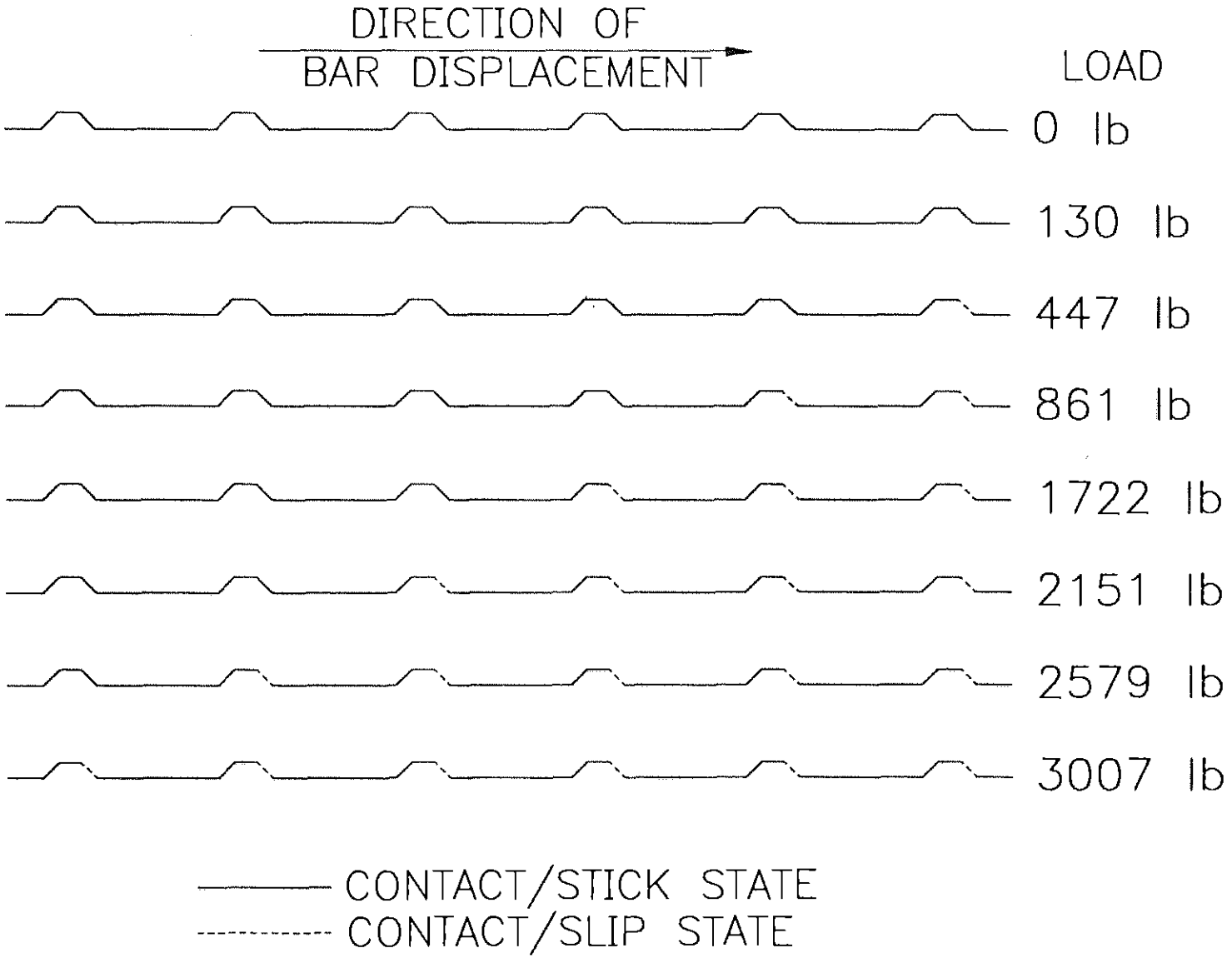

Fig. 3.1 Progressive Change of Interface Element Material State (Model with 6 Ribs, 1/2 in. Lead Length, and 2 in. Cover)

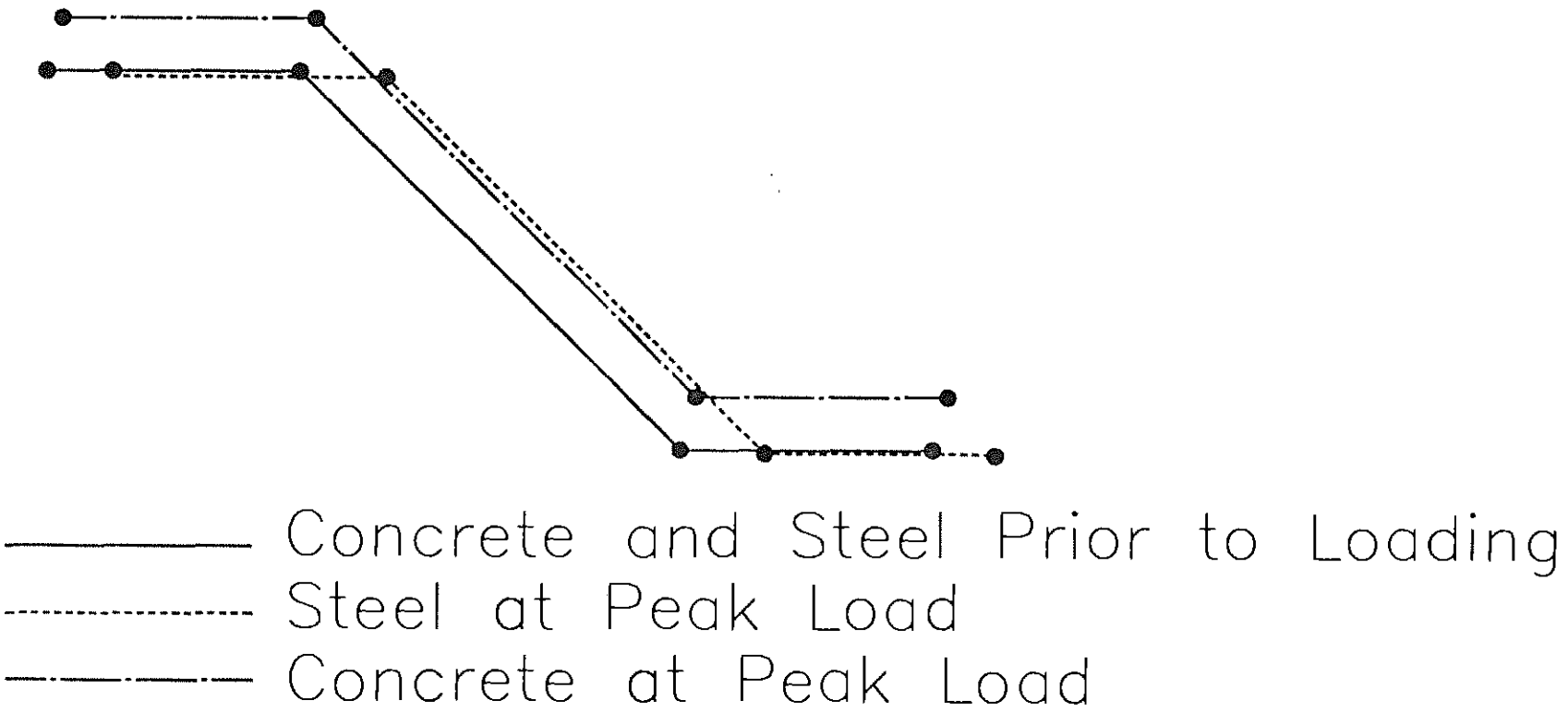

Fig. 3.2 Movement of Interface from Initial to Peak Load for Model with 6 Ribs, 1/2 in. Lead Length, and 2 in. Cover (after Choi et al. 1990)

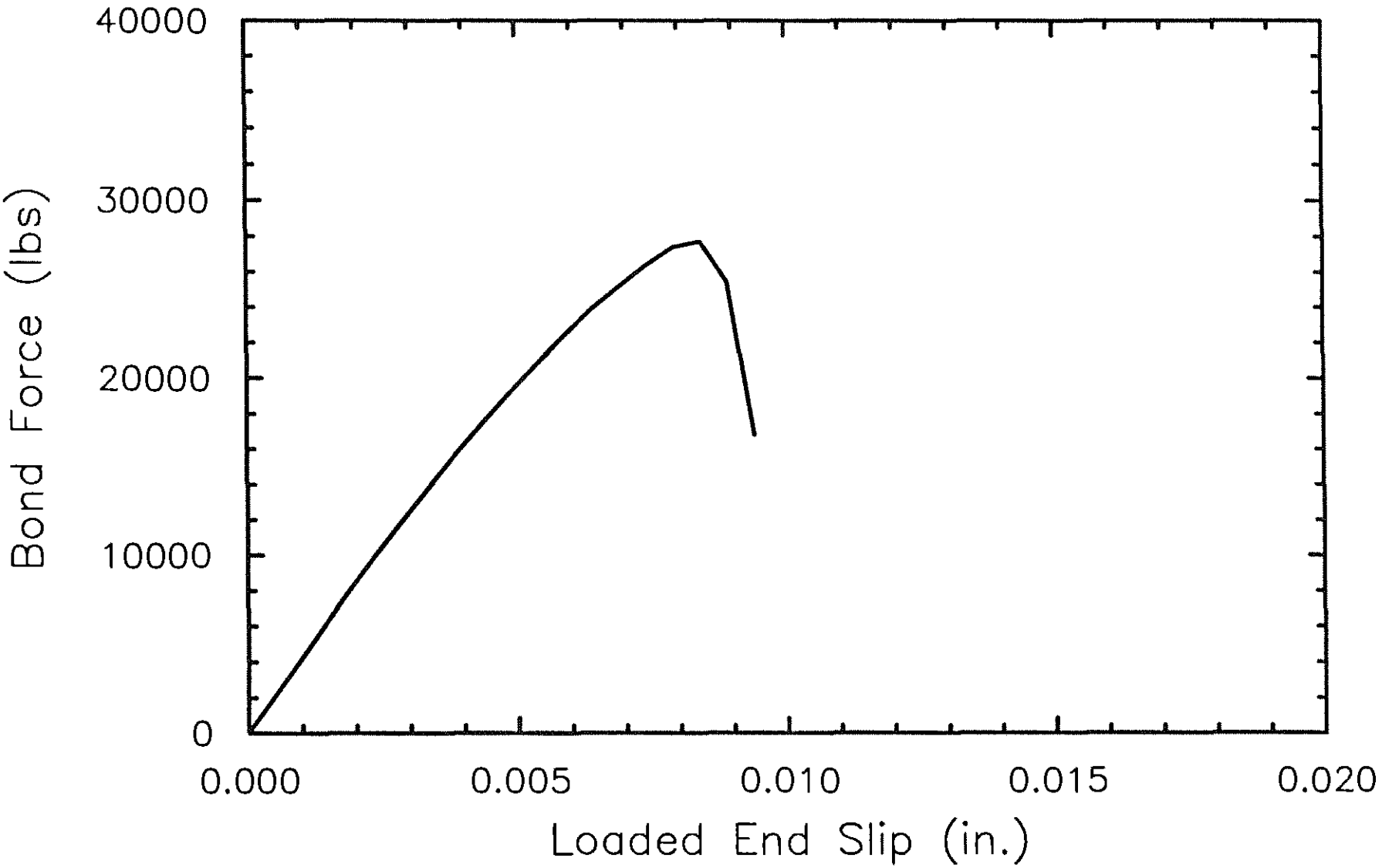

Fig. 3.3 Bond Force-Loaded End Slip Curve for Model with 6 Ribs, 1/2 in. Lead Length, and 2 in. Cover

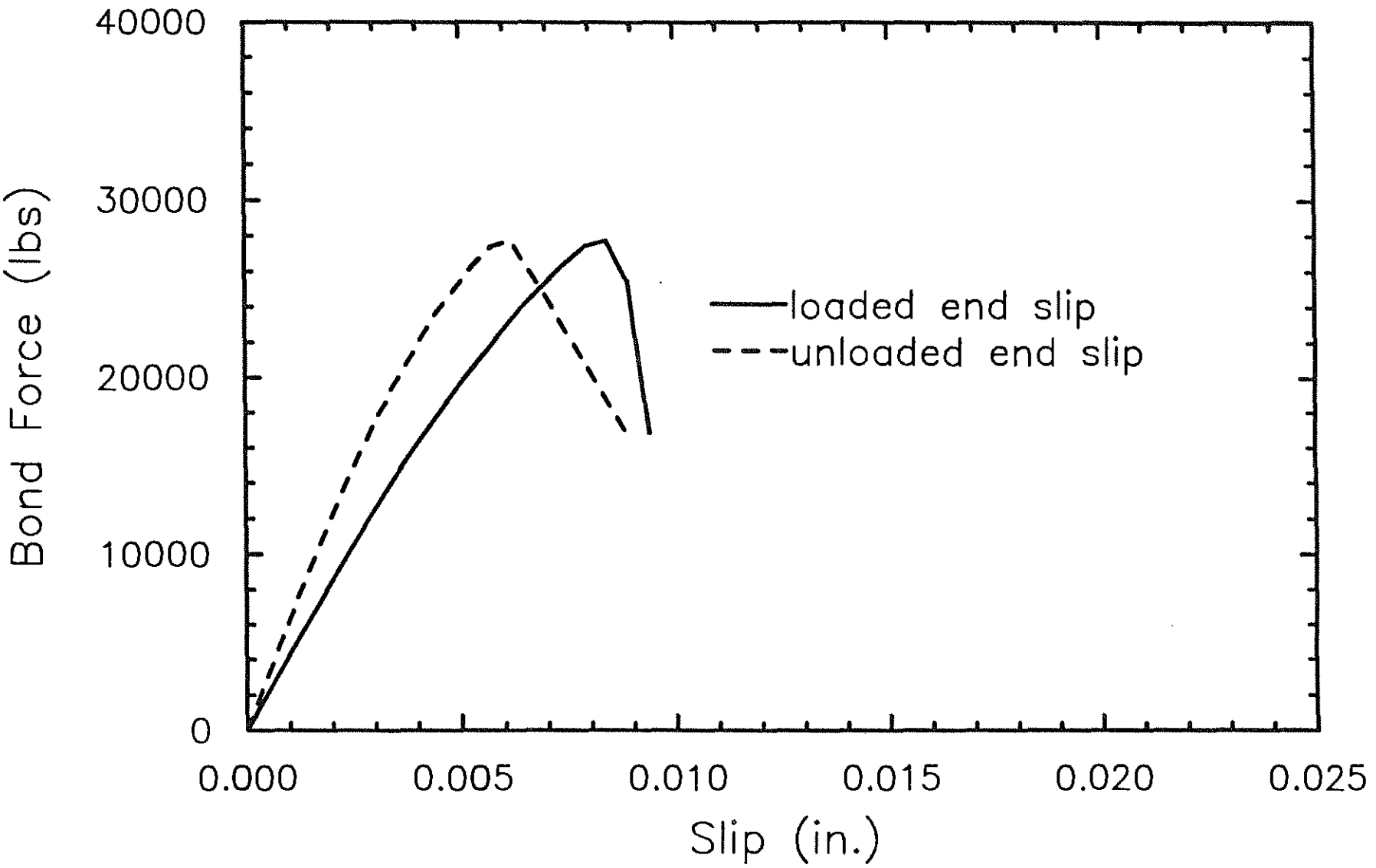

Fig. 3.4 Bond Force-Loaded End Slip and Bond Force-Unloaded End Slip Curves for Model with 6 Ribs, 1/2 in. Lead Length, and 2 in. Cover

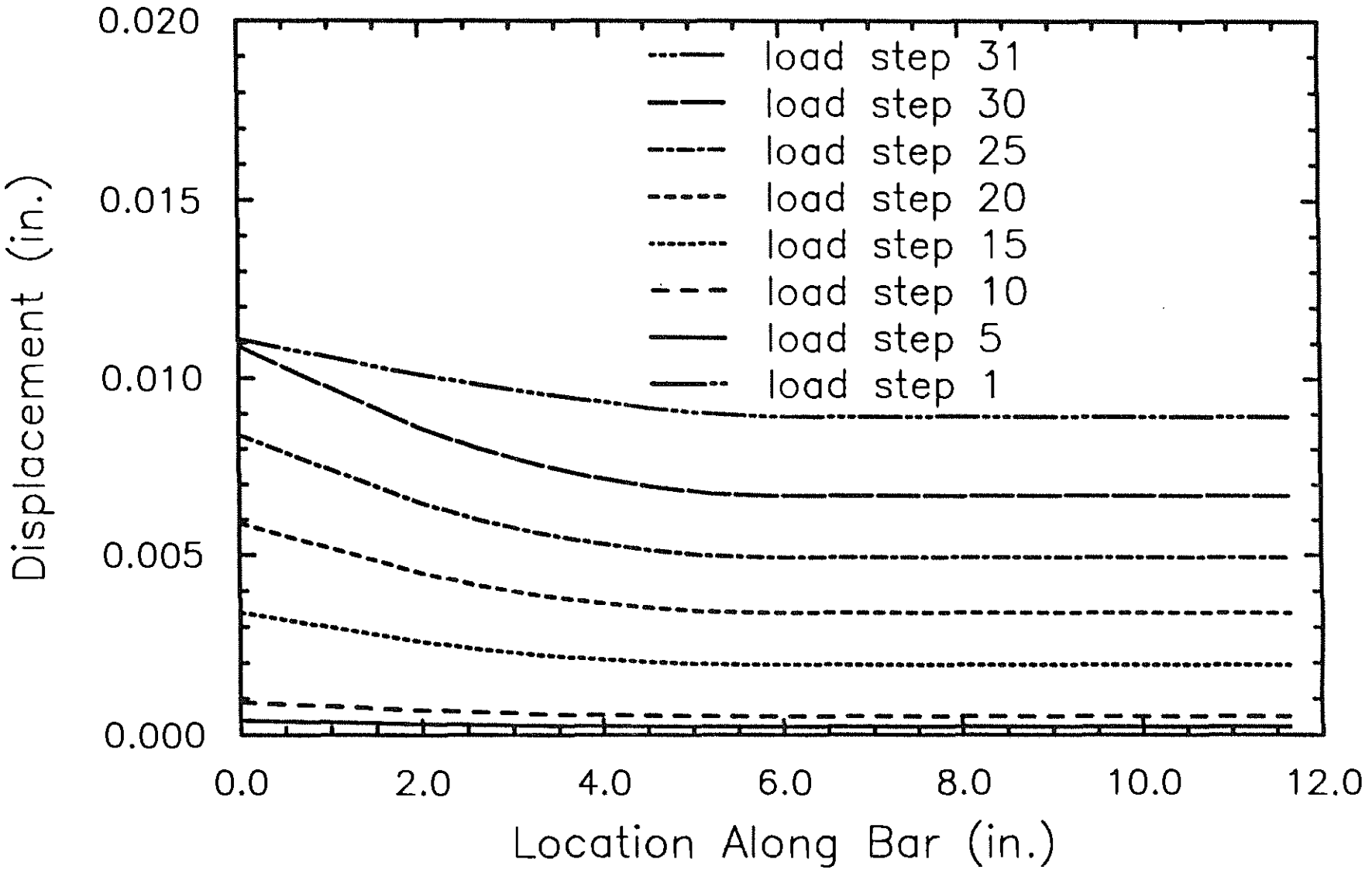

Fig. 3.5 Displacements Along Length of Bar from Initial to Peak Loading for 6 Rib Model (Embedded Length = 5.42 in.)

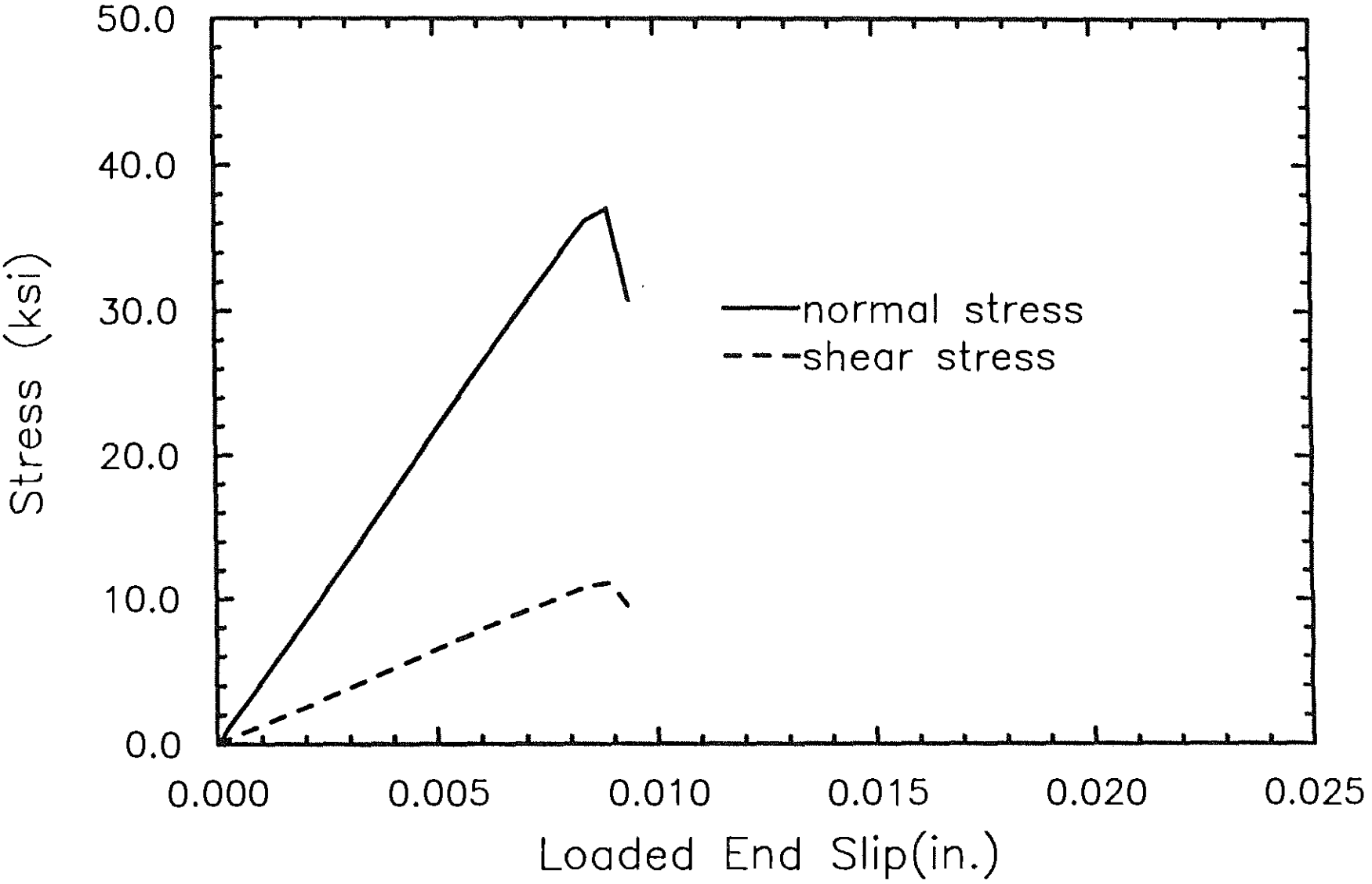

Fig. 3.6 Stresses on Interface Element closest to Imposed Displacement (Model with 6 Ribs, 1/2 in. Lead Length, and 2 in. Cover)

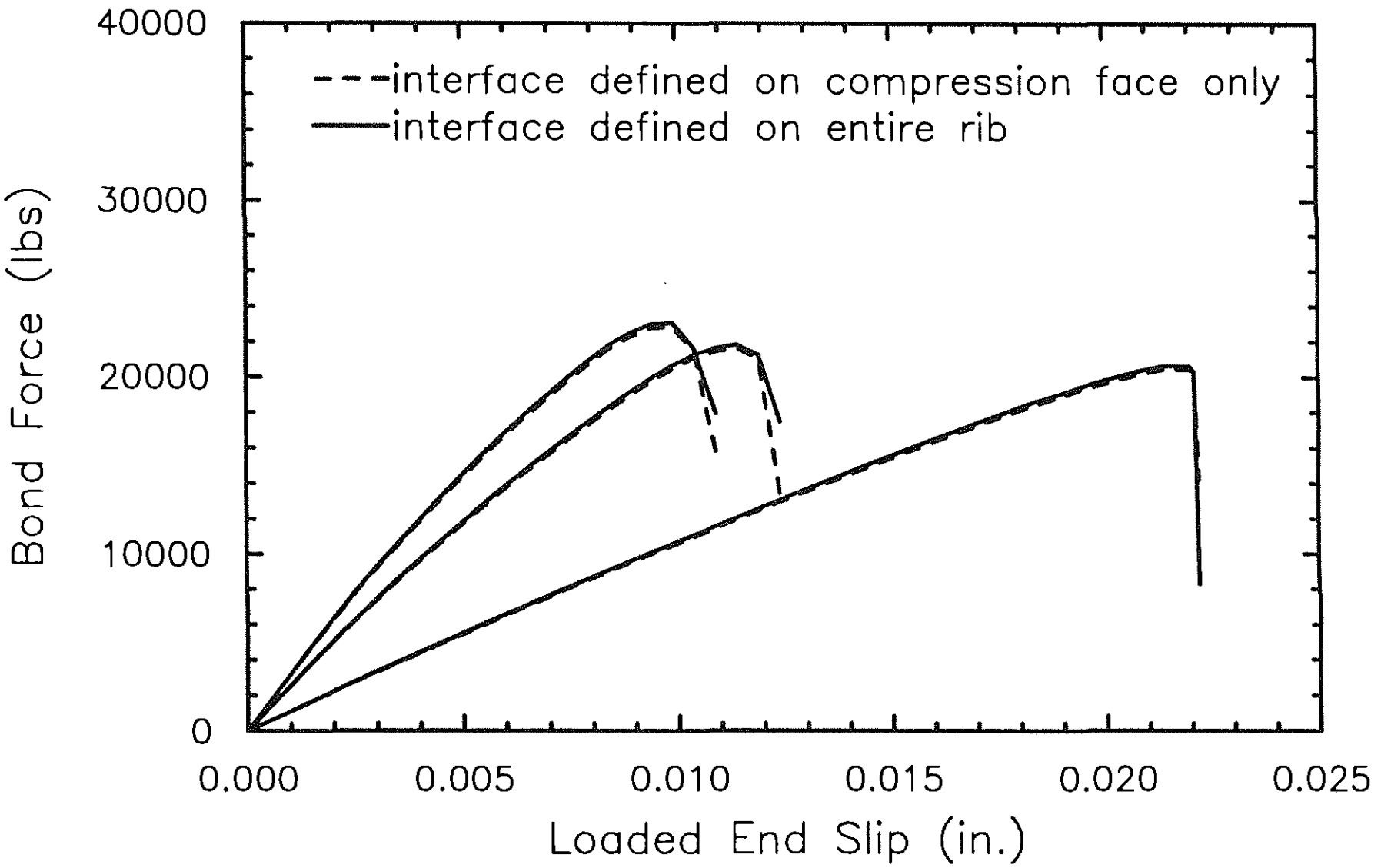

Fig. 3.7 Bond Force-Loaded End Slip Curves for 1, 2, and 3 Rib Models with Interface Elements on Compression Face of Rib and Interface Elements on Entire Rib

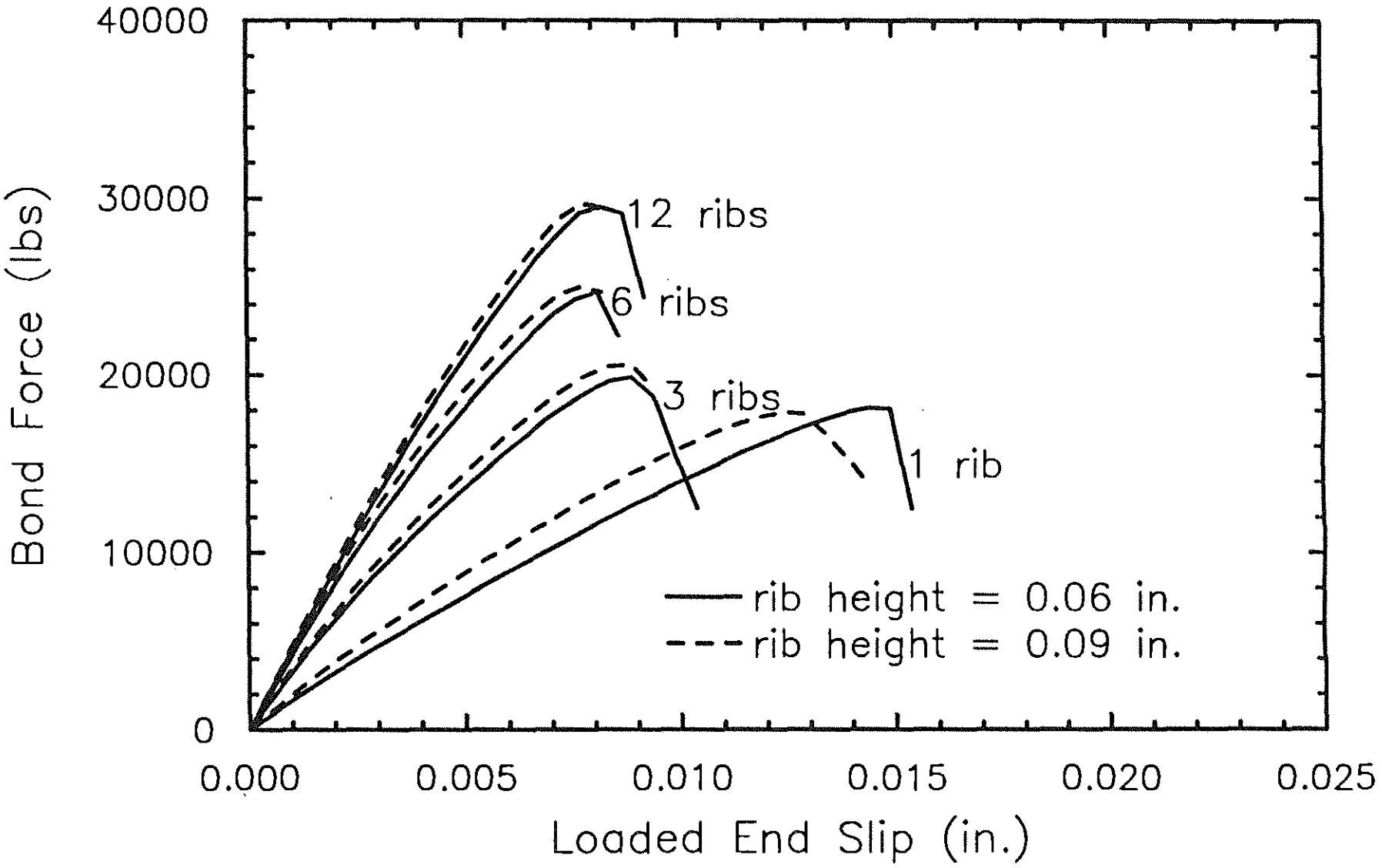

Fig. 3.8 Bond Force-Loaded End Slip Curves for Models with 1 in. Cover and Rib Heights of 0.06 in. and 0.09 in. (Lead Length = 1/2 in.)

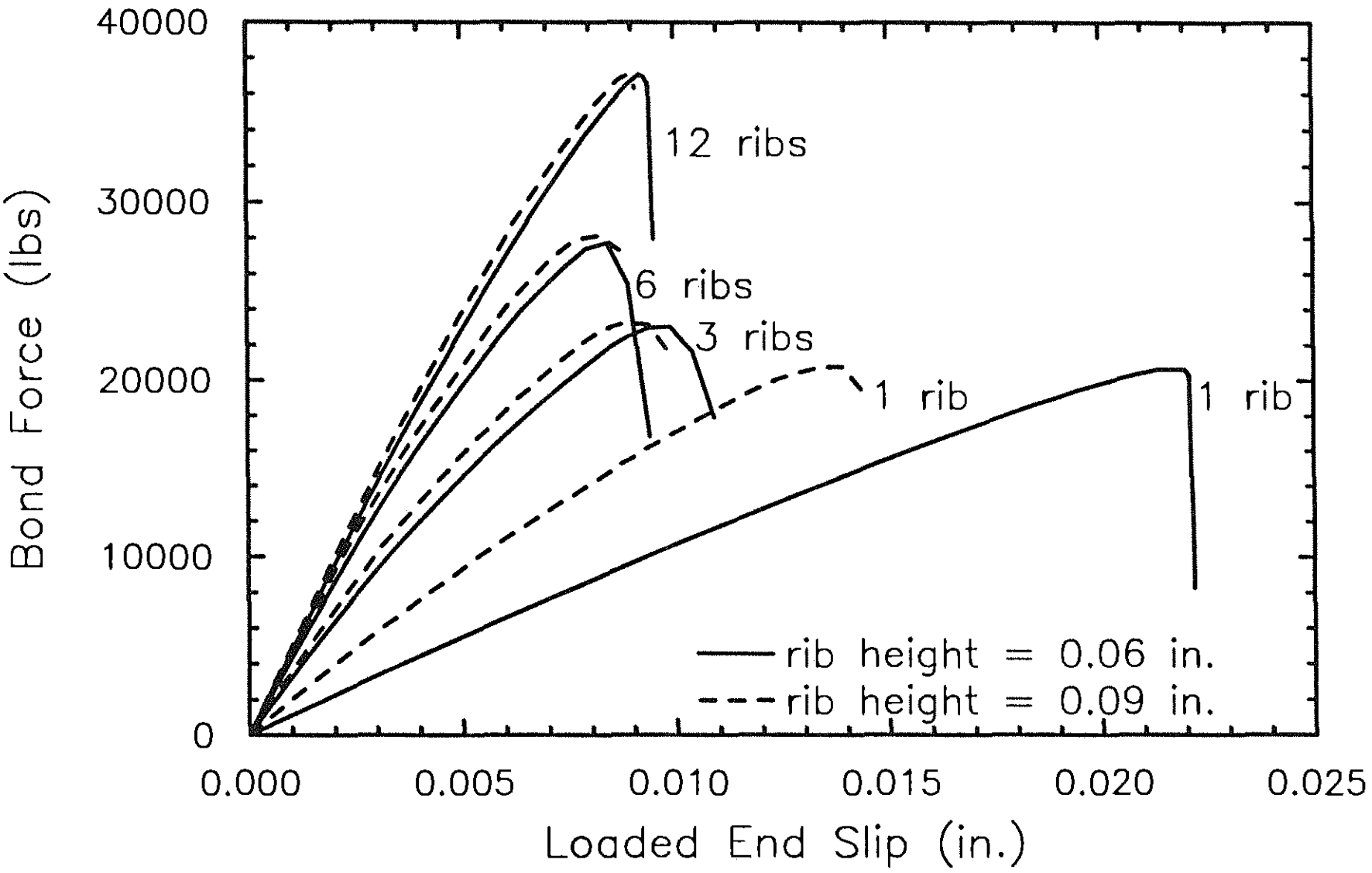

Fig. 3.9 Bond Force-Loaded End Slip Curves for Models with 2 in. Cover and Rib Heights of 0.06 in. and 0.09 in. (Lead Length = 1/2 in.)

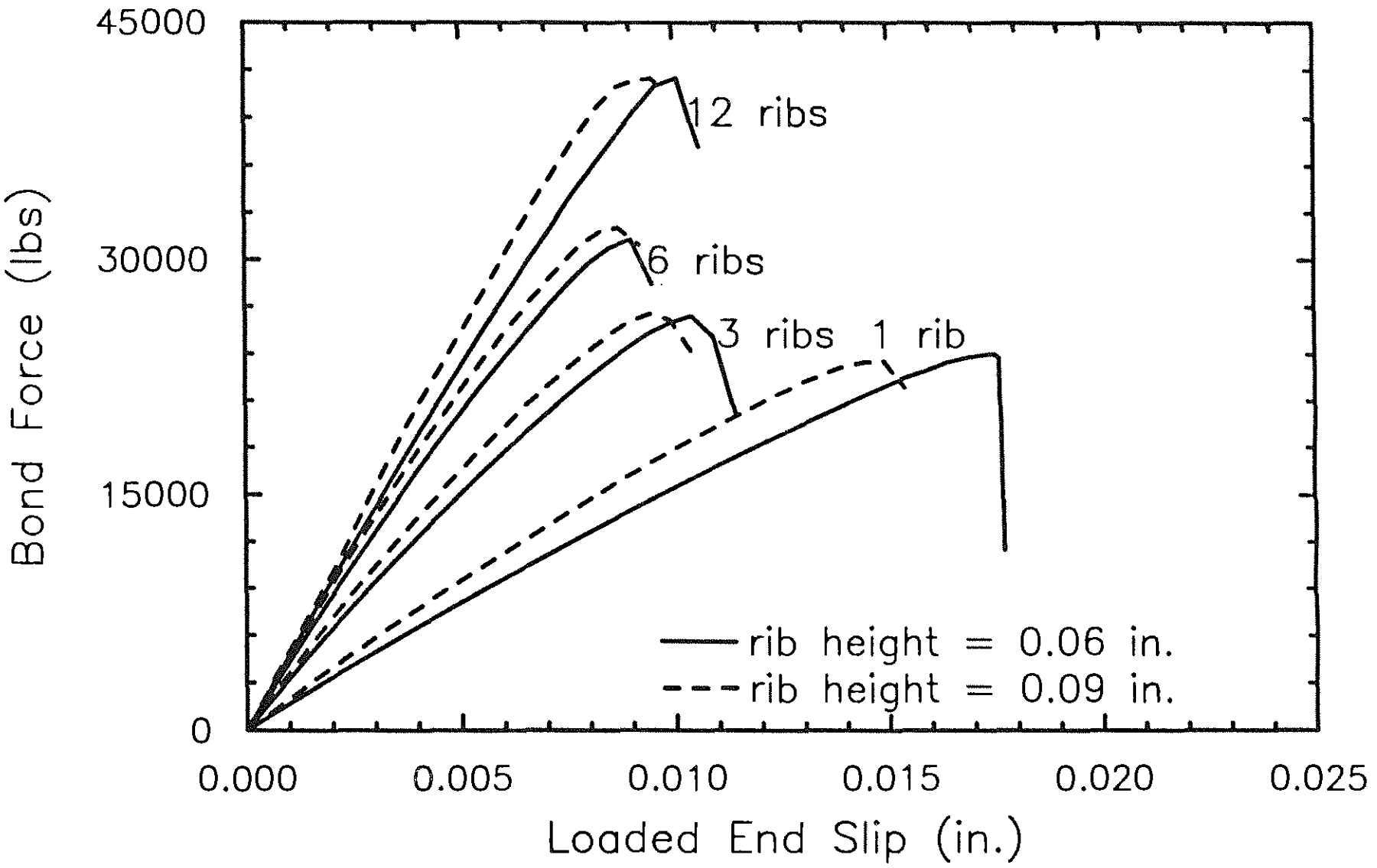

Fig. 3.10 Bond Force-Loaded End Slip Curves for Models with 3 in. Cover and Rib Heights of 0.06 in. and 0.09 in. (Lead Length = 1/2 in.)

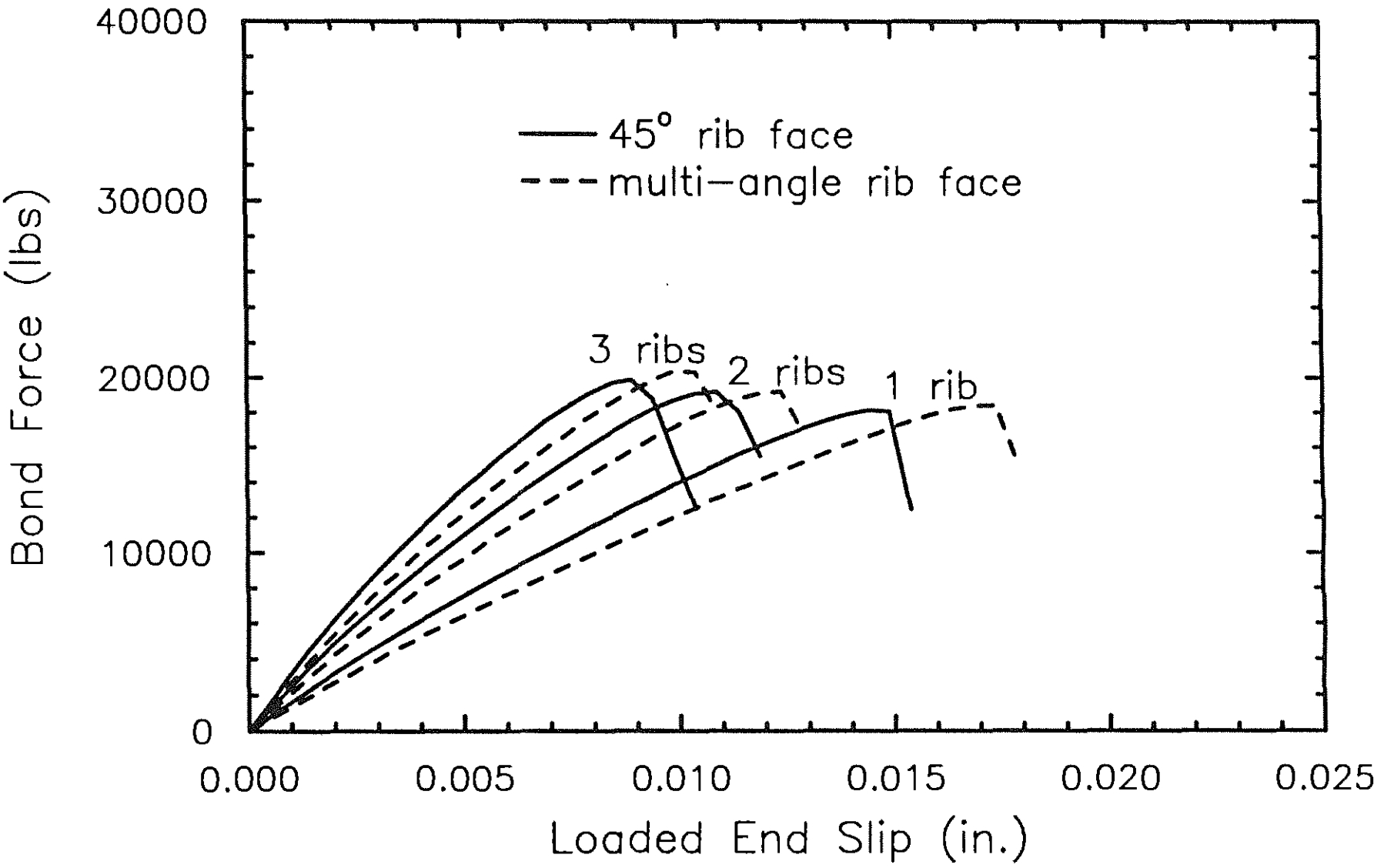

Fig. 3.11 Bond Force-Loaded End Slip Curves for Models with 45° Ribs and Multi-angle Ribs (Rib Height = 0.06 in., 1 in. Cover, 1/2 in. Lead Length)

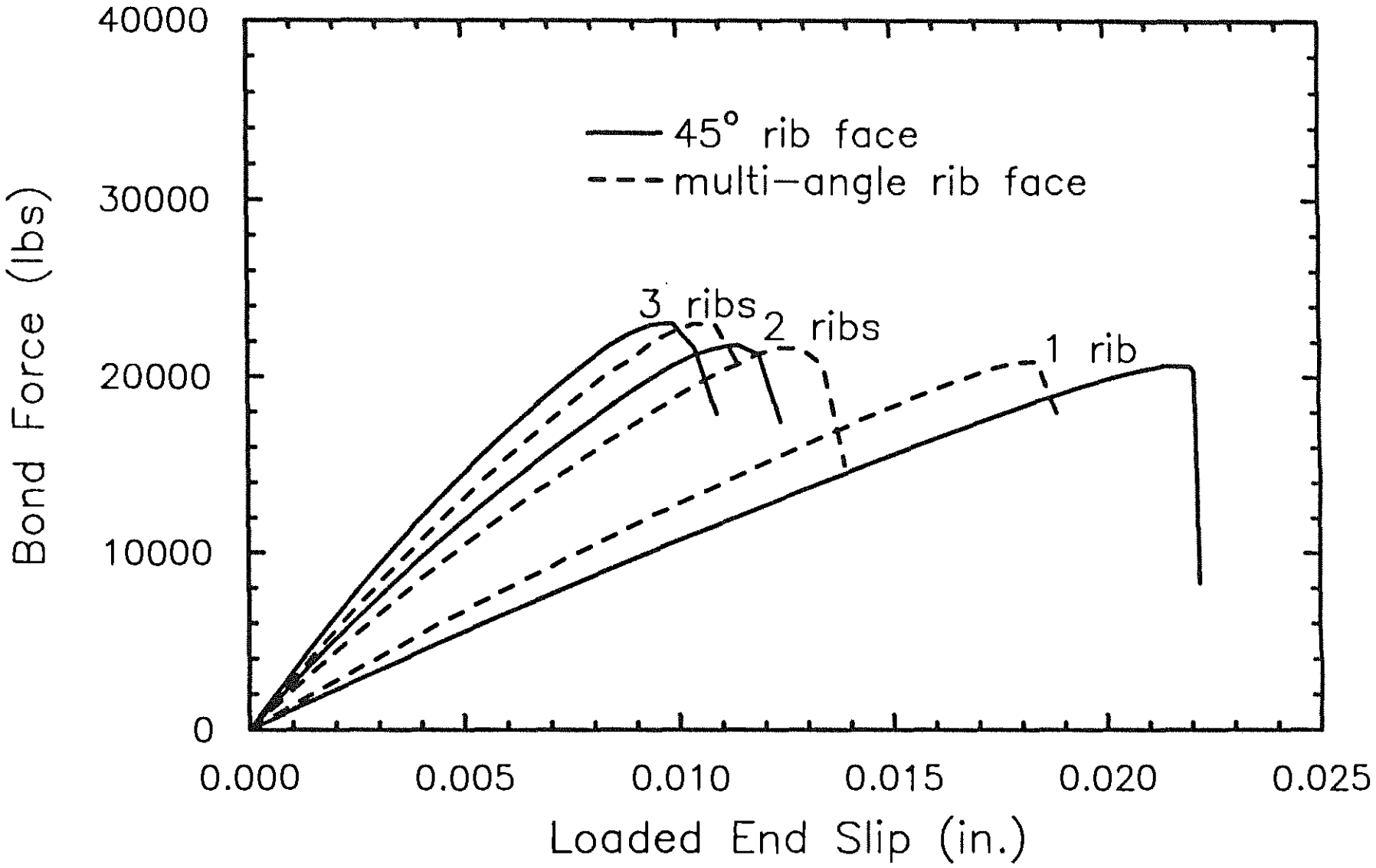

Fig. 3.12 Bond Force-Loaded End Slip Curves for Models with 45° Ribs and Multi-angle Ribs (Rib Height = 0.06 in., 2 in. Cover, 1/2 in. Lead Length)

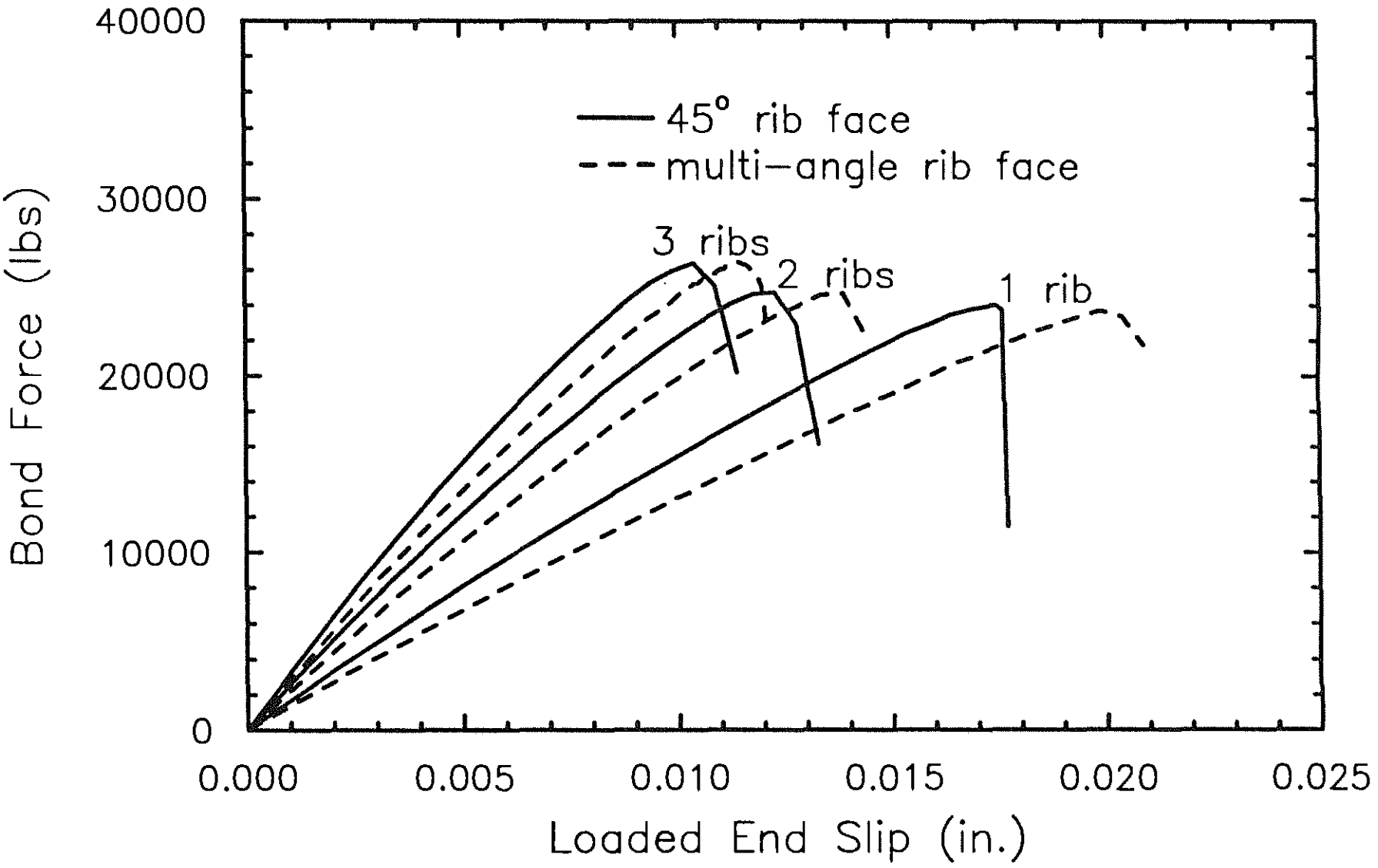

Fig. 3.13 Bond Force-Loaded End Slip Curves for Models with 45° Ribs and Multi-angle Ribs (Rib Height = 0.06 in., 3 in. Cover, 1/2 in. Lead Length)

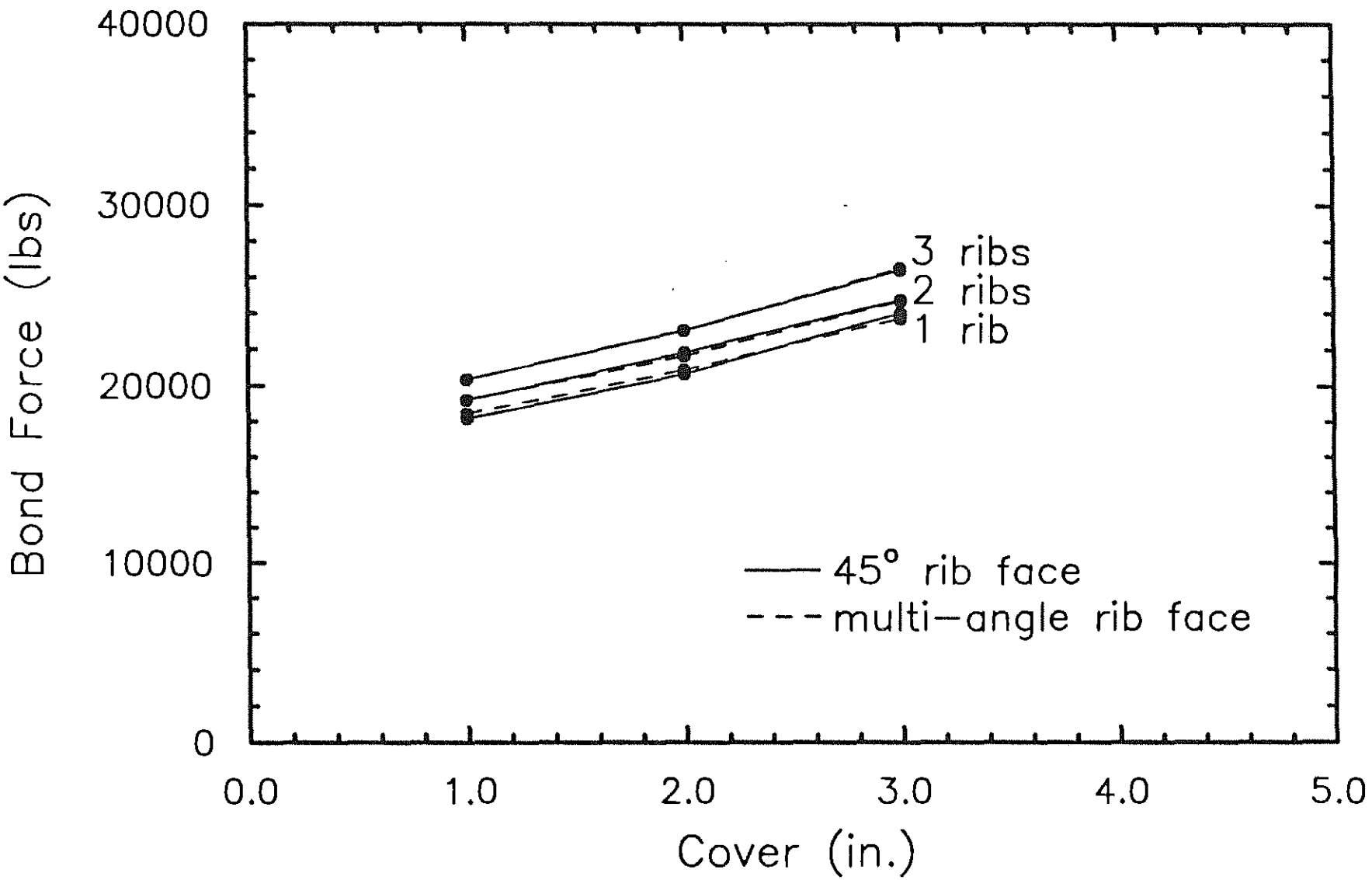

Fig. 3.14 Bond Force versus Cover for Models with 45° Ribs and Multi-angle Ribs (Rib Height = 0.06 in., 1/2 in. Lead Length)

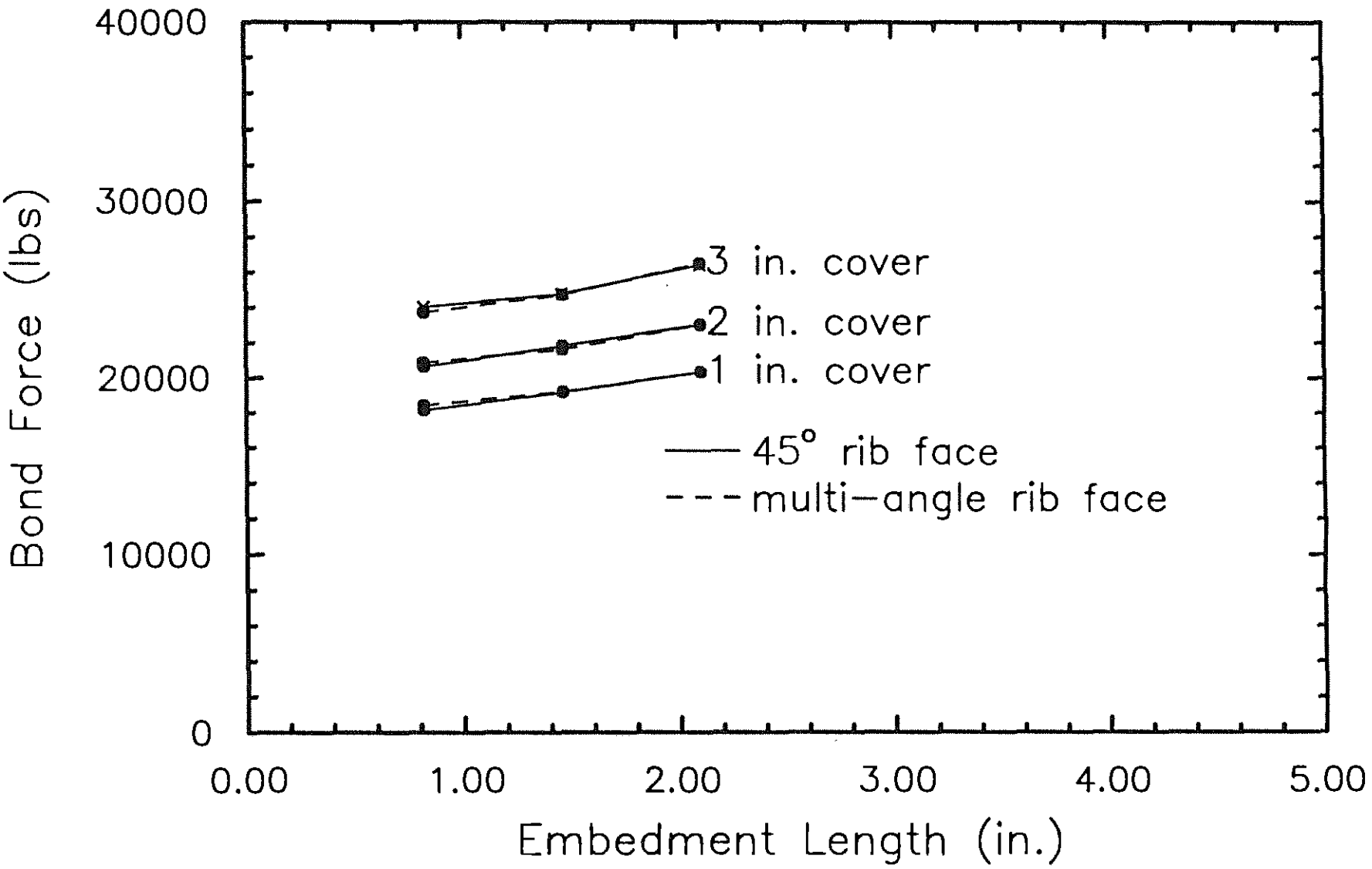

Fig. 3.15 Bond Force versus Embedded Length for Models with 45° Ribs and Multi-angle Ribs (Rib Height = 0.06 in., 1/2 in. Lead Length)

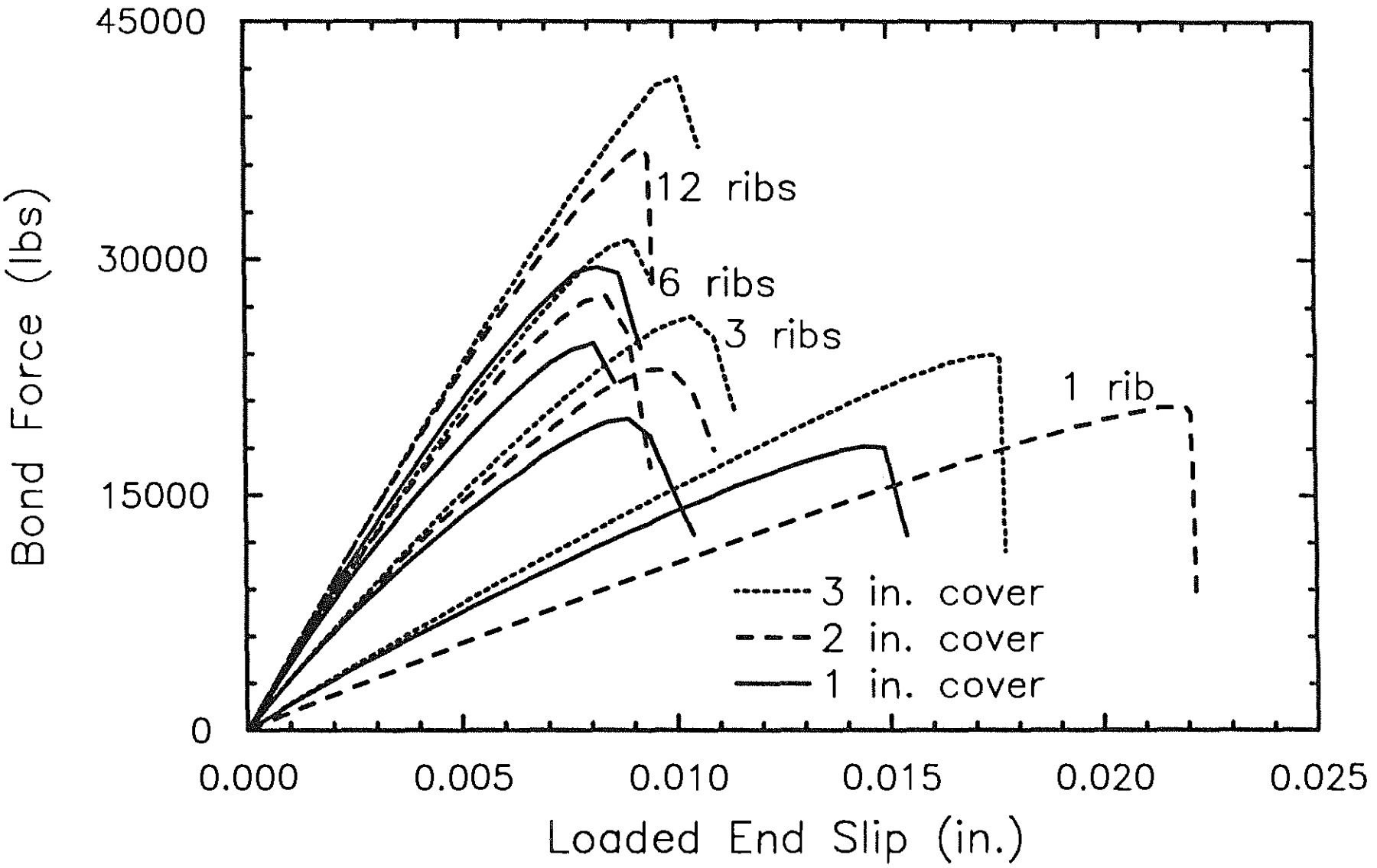

Fig. 3.16 Bond Force-Loaded End Slip Curves for Models with 1, 2, and 3 in. Covers (45° Rib, Rib Height = 0.06 in., 1/2 in. Lead Length)

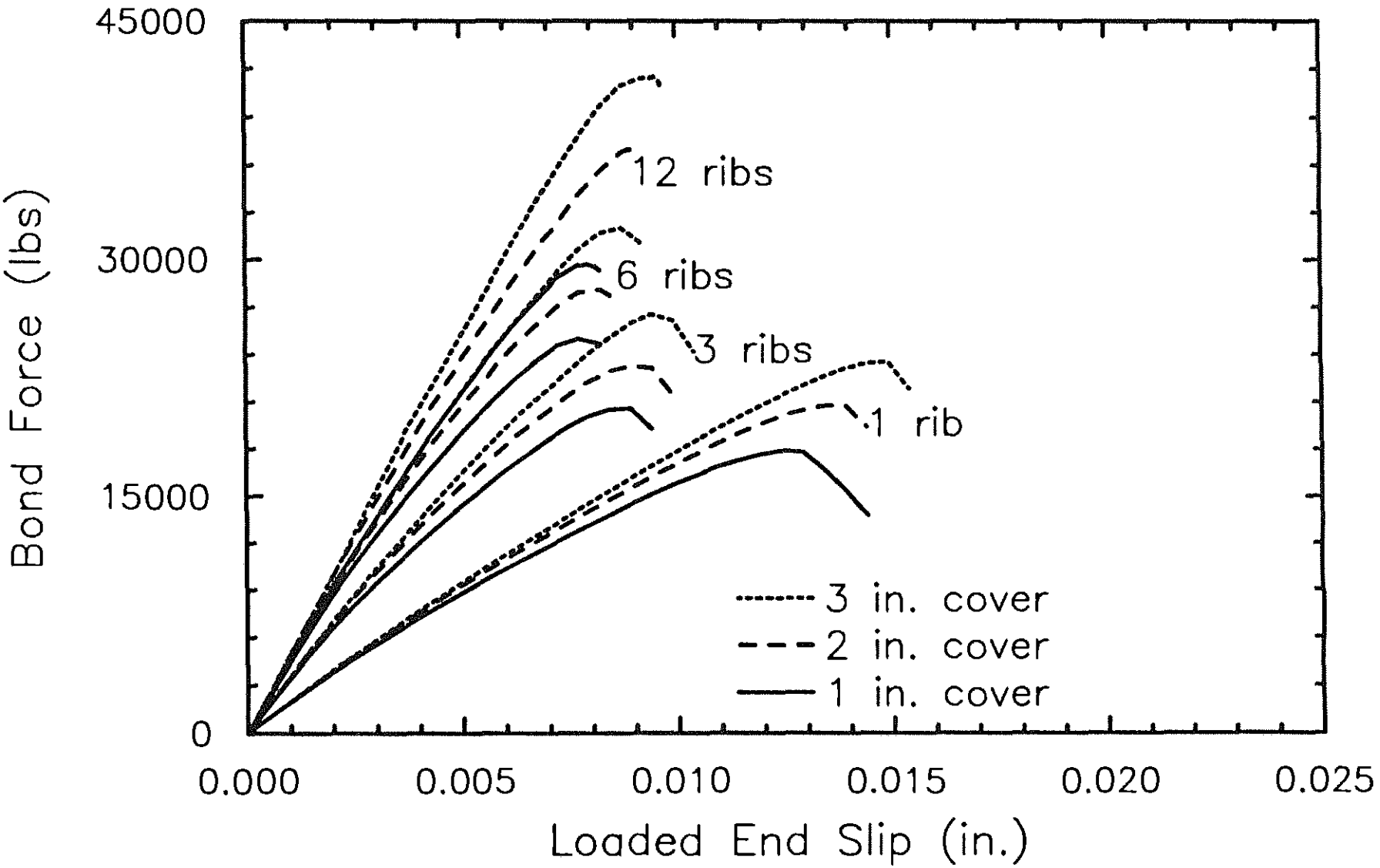

Fig. 3.17 Bond Force-Loaded End Slip Curves for Models with 1, 2, and 3 in. Covers (45° Rib, Rib Height = 0.09 in., 1/2 in. Lead Length)

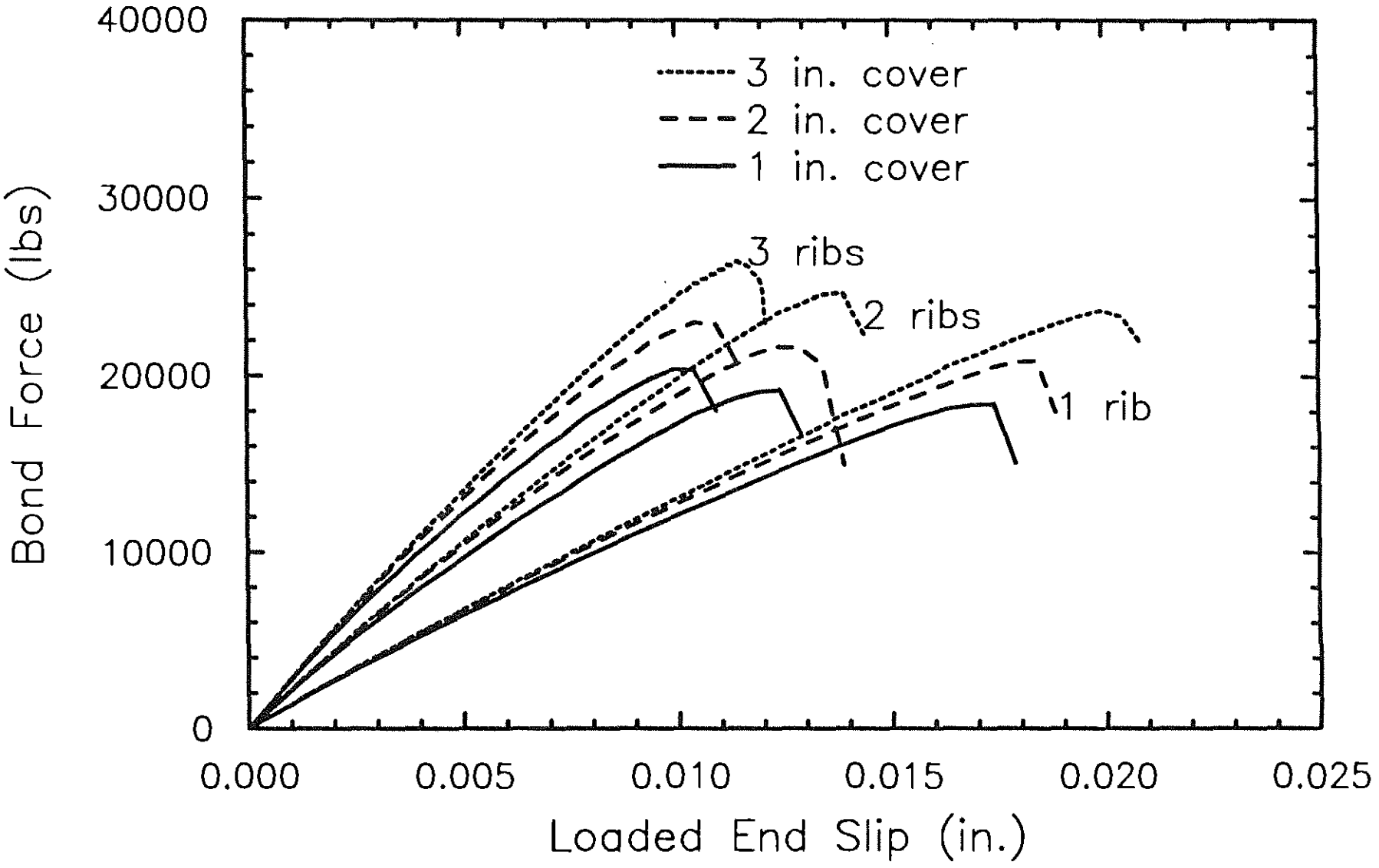

Fig. 3.18 Bond Force-Loaded End Slip Curves for Models with 1, 2, and 3 in. Covers (Multi-Angle Rib Faces, 1/2 in. Lead Length)

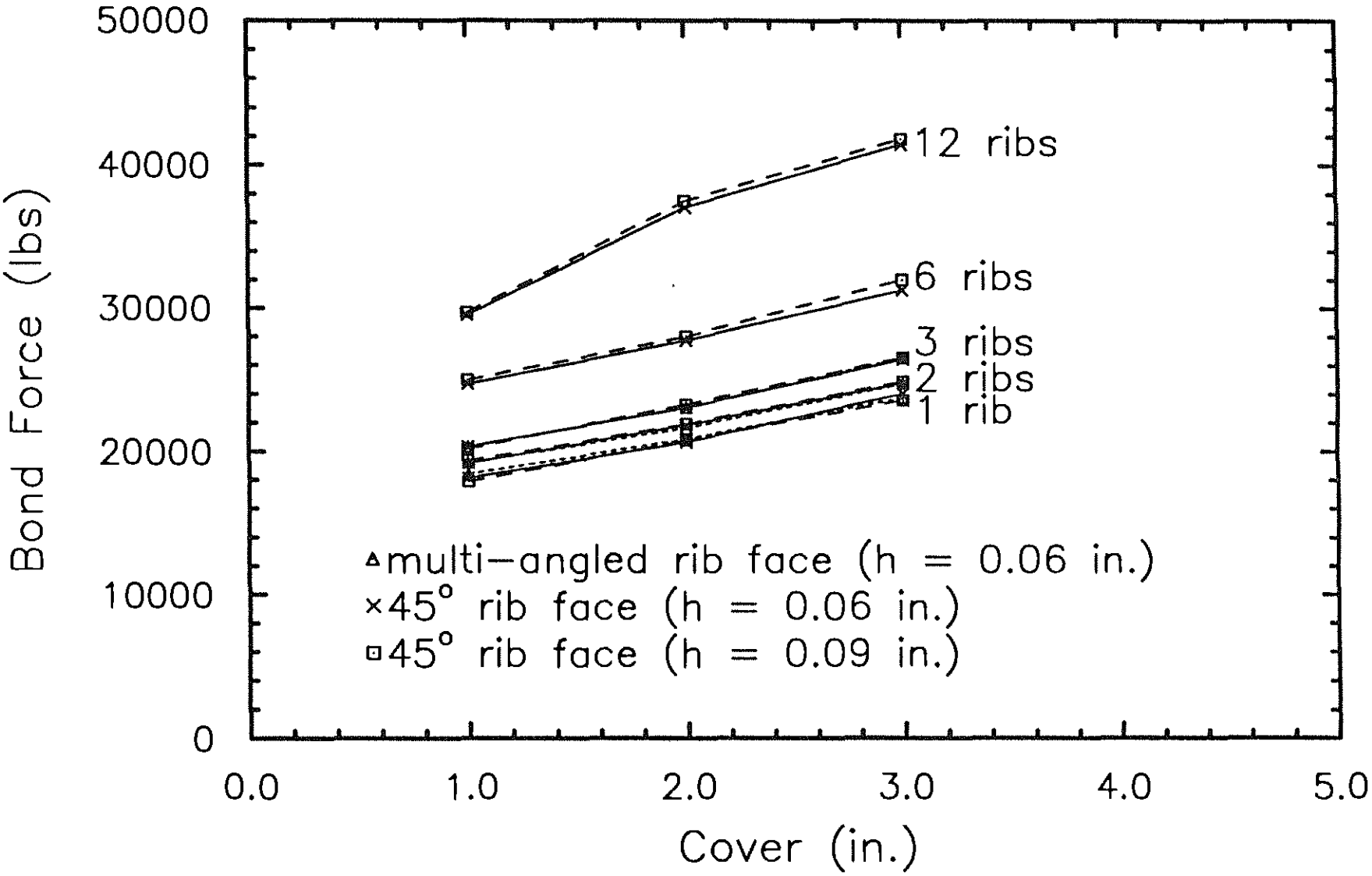

Fig. 3.19 Bond Force versus Cover (1/2 in. Lead Length, Rib Heights of 0.06 in. and 0.09 in.)

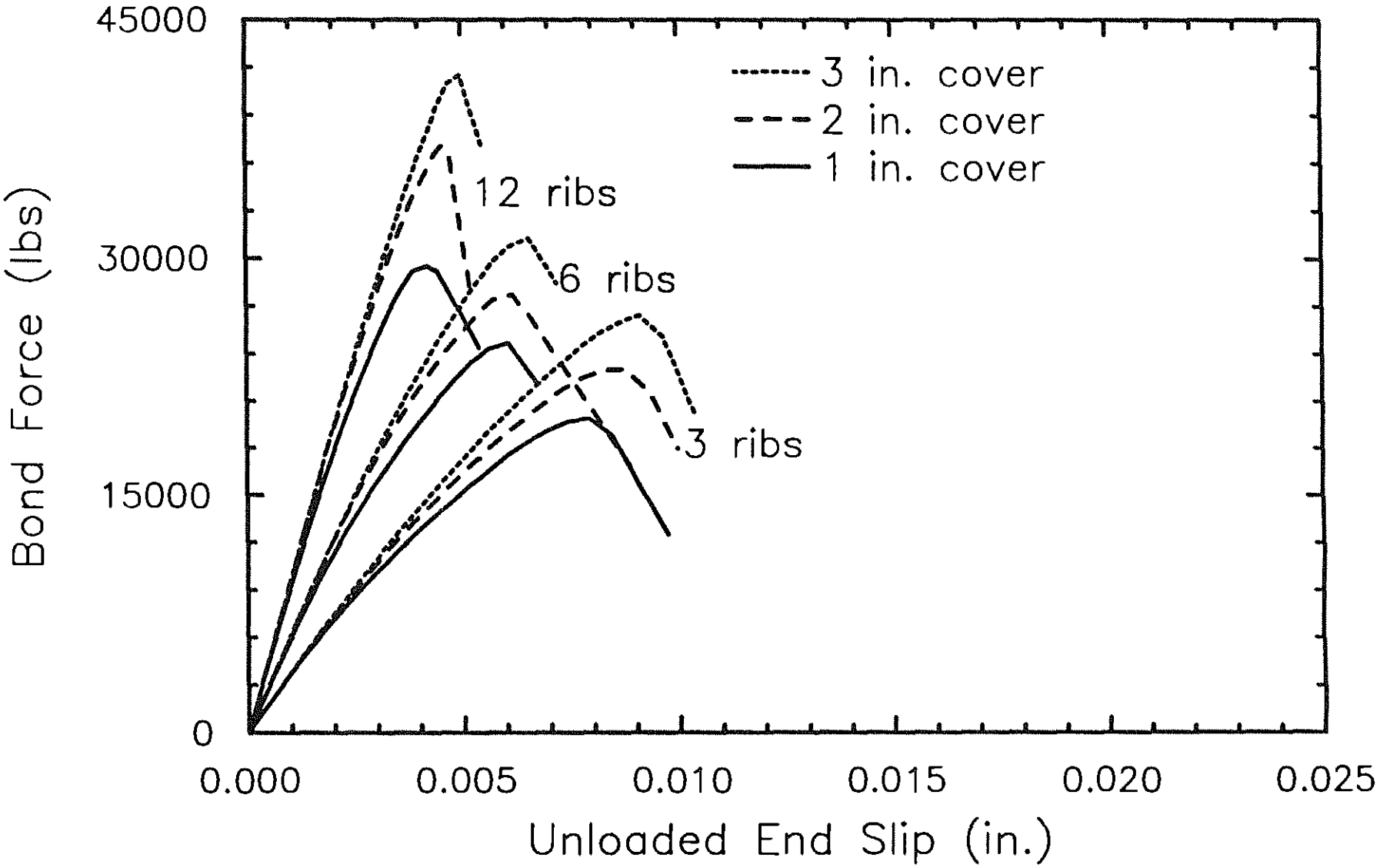

Fig. 3.20 Bond Force-Unloaded End Slip Curves for Models with 1, 2, and 3 in. Covers (45° Rib, Rib Height = 0.06 in., 1/2 in. Lead Length)

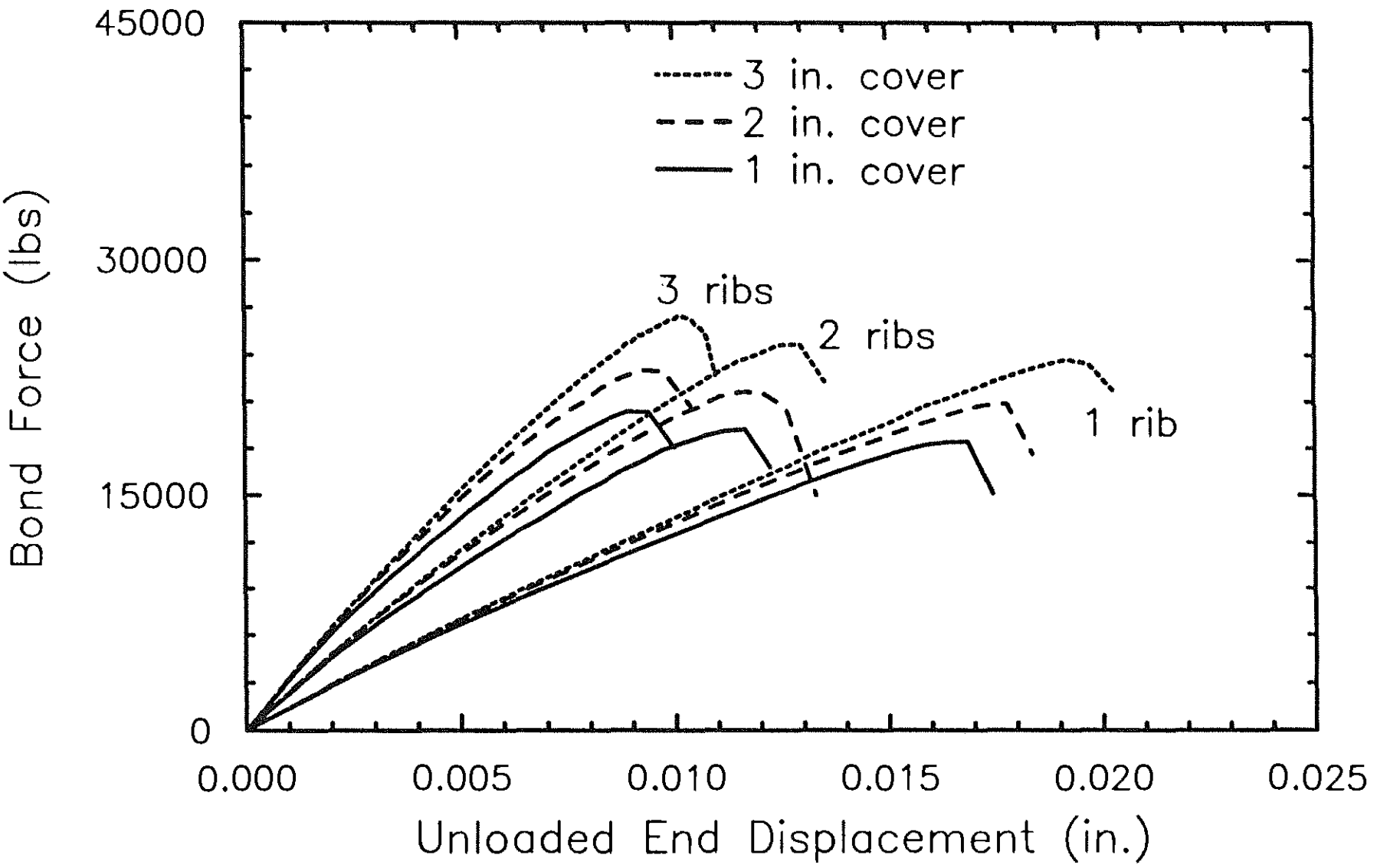

Fig. 3.21 Bond Force-Unloaded end Slip Curves for Models with 1, 2, and 3 in. Covers (Multi-Angle Rib Faces, 1/2 in. Lead Length)

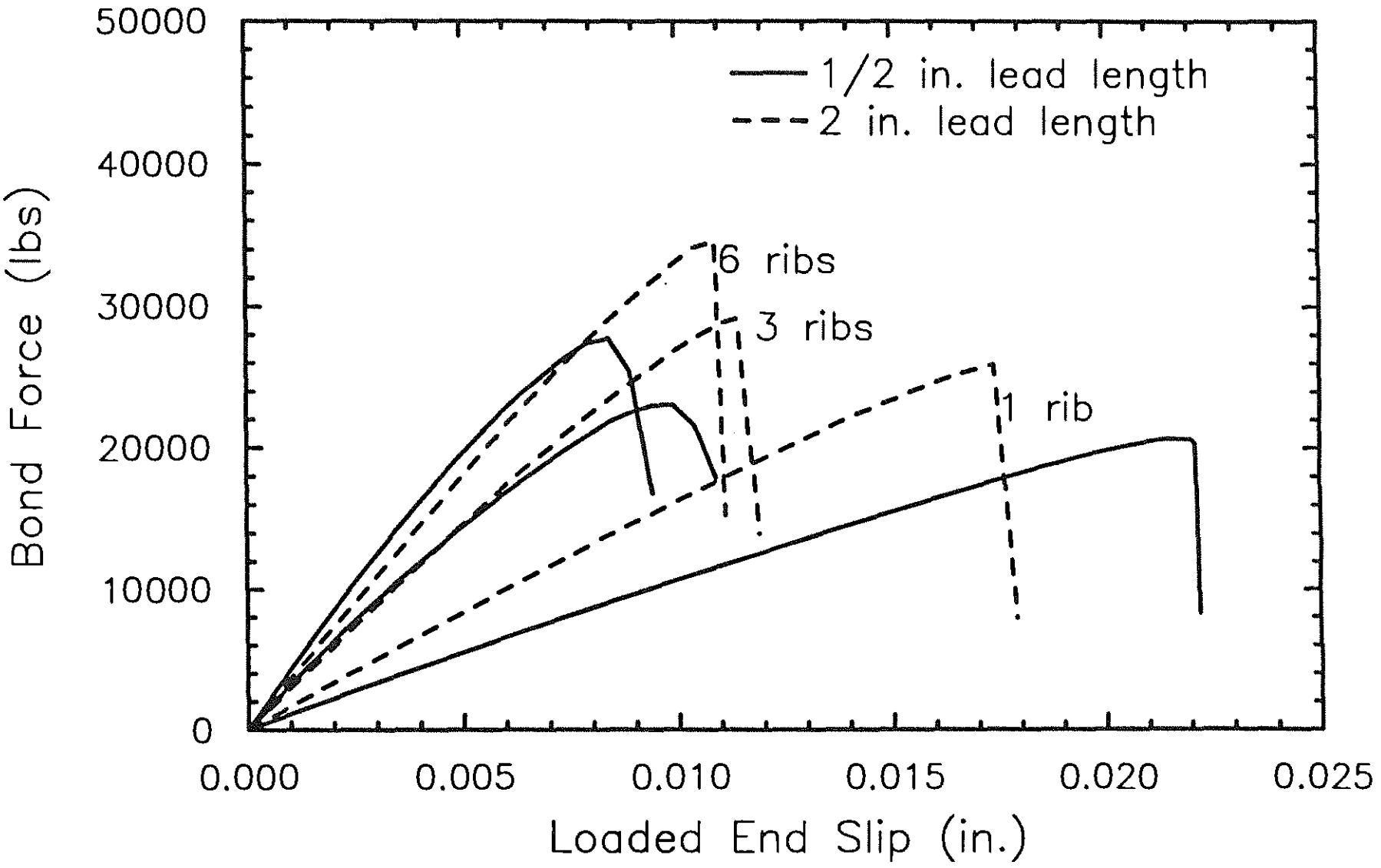

Fig. 3.22 Bond Force-Loaded End Slip Curves for Models with 1/2 in. and 2 in. Lead Lengths (45° Ribs, Rib Height = 0.06 in., 2 in. Cover)

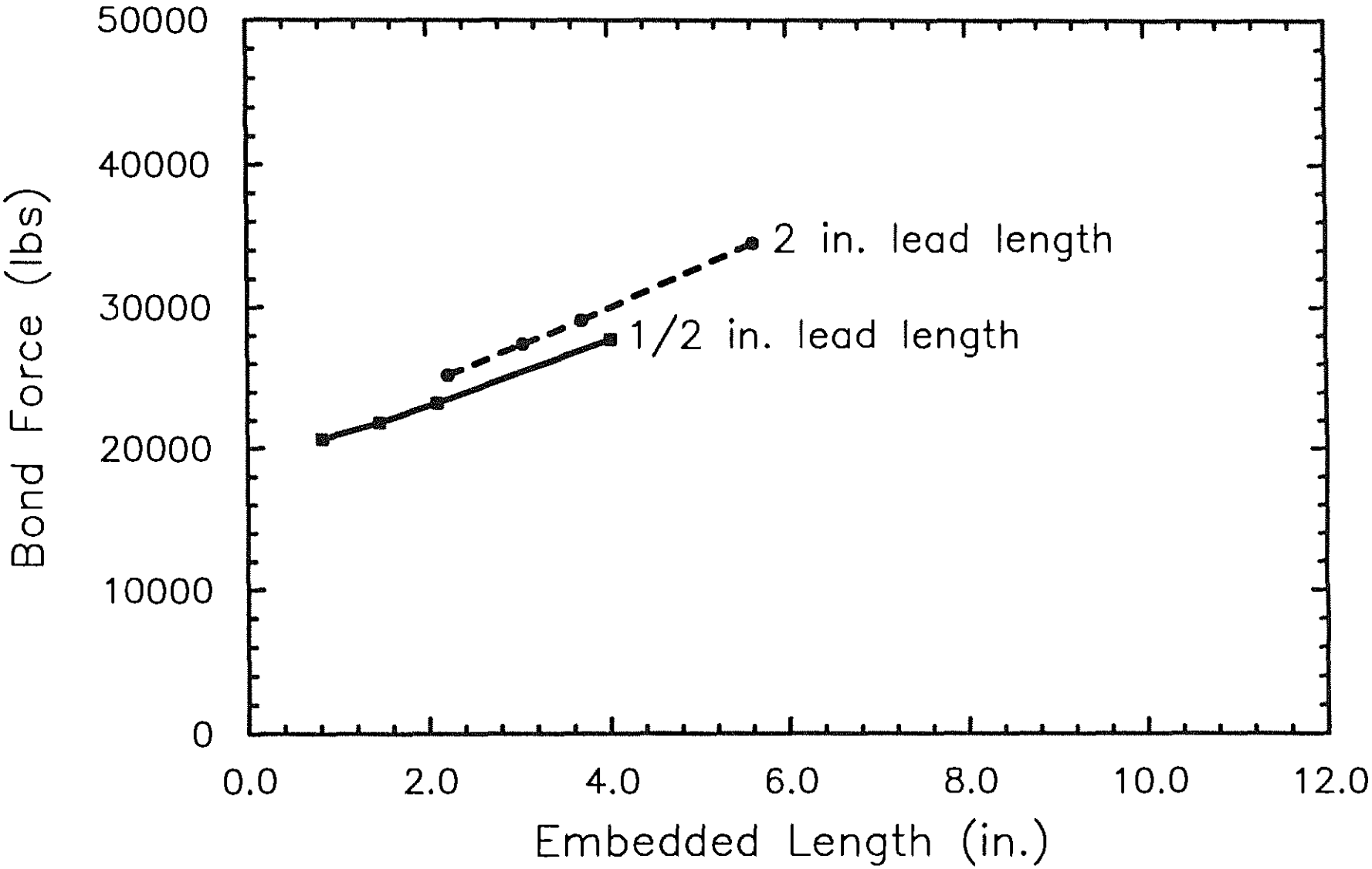

Fig. 3.23 Bond Force versus Embedded Length Curves for Models with 1/2 in. and 2 in. Lead Lengths (45° Ribs, Rib Height = 0.06 in., 2 in. Cover)

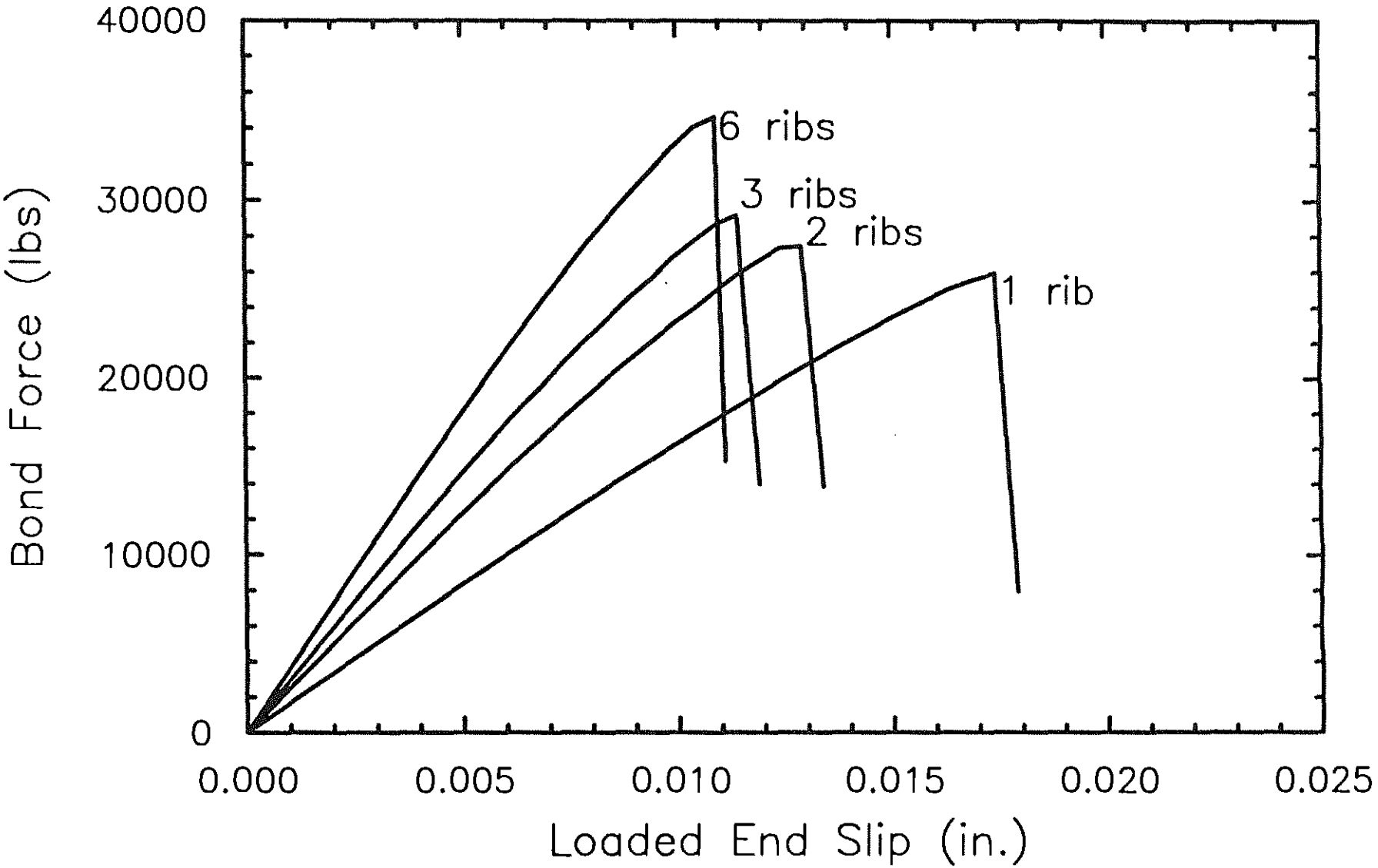

Fig. 3.24 Bond Force-Loaded End Slip Curves for Models with 2 in. Lead Lengths (45° Ribs, 2 in. Cover)

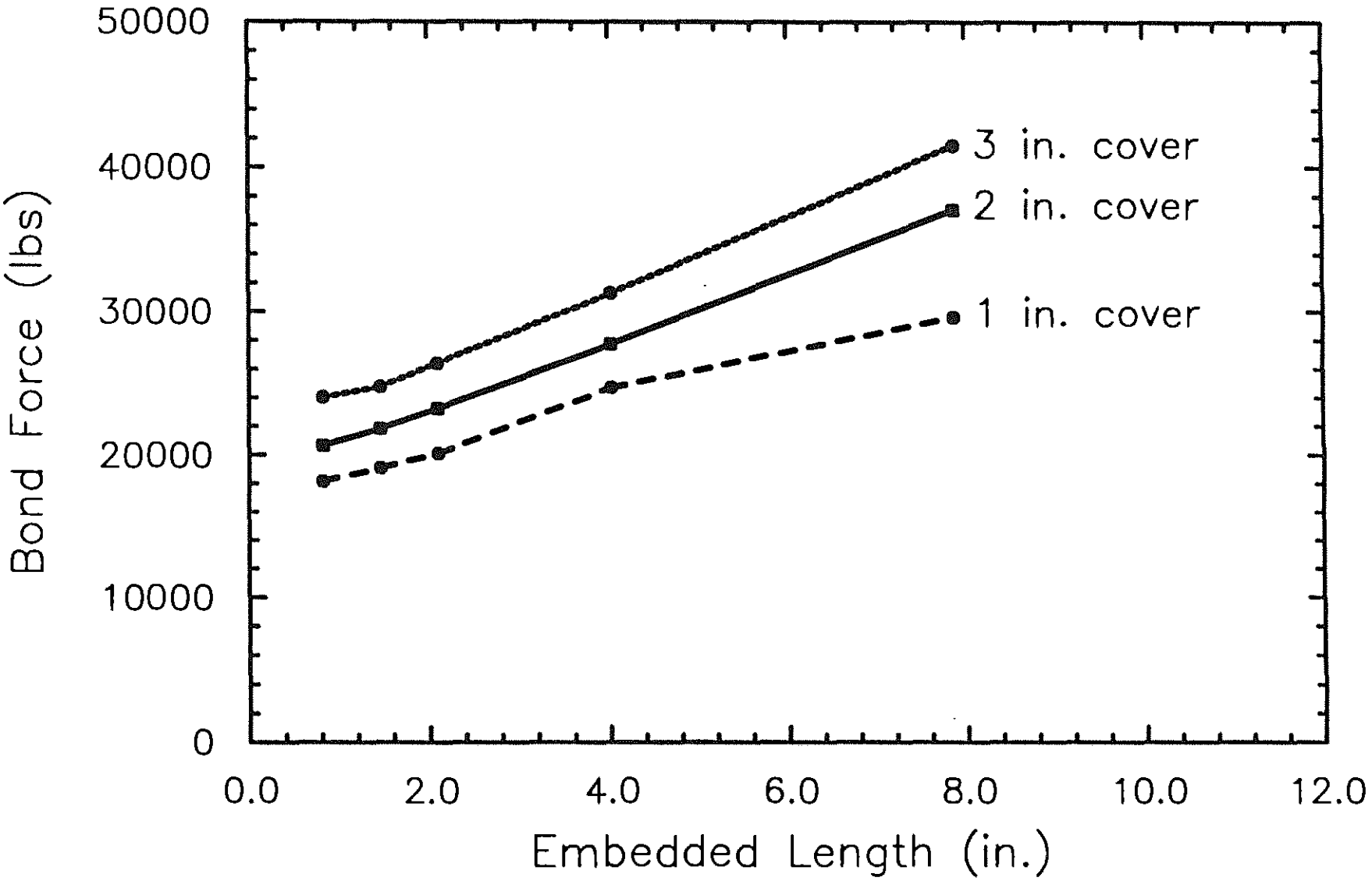

Fig. 3.25 Bond Force versus Embedded Length (45° Ribs, Rib Height = 0.06 in., 1/2 in. Lead Length)

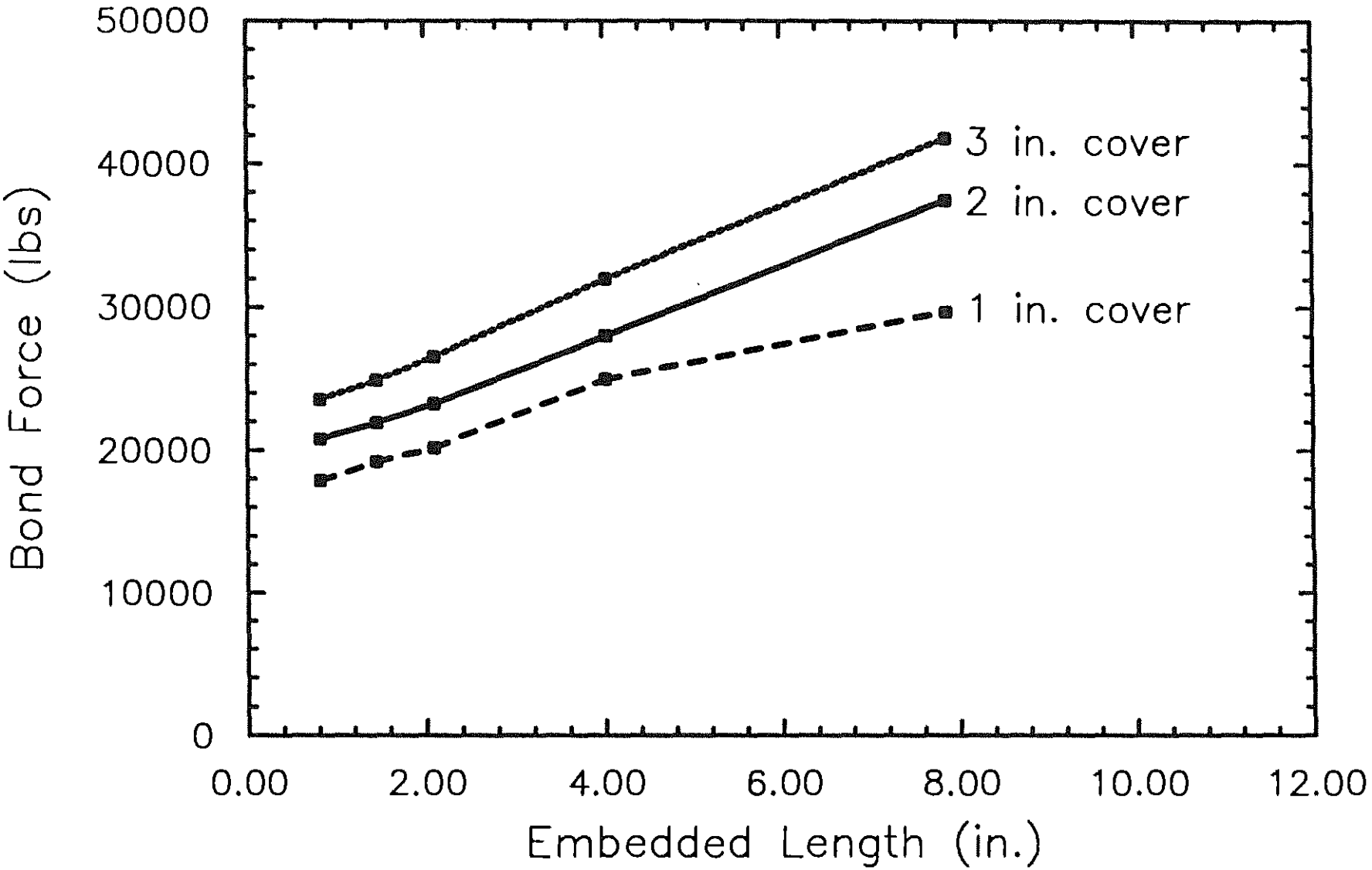

Fig. 3.26 Bond Force versus Embedded Length (45° Ribs, Rib Height = 0.09 in., 1/2 in. Lead Length)

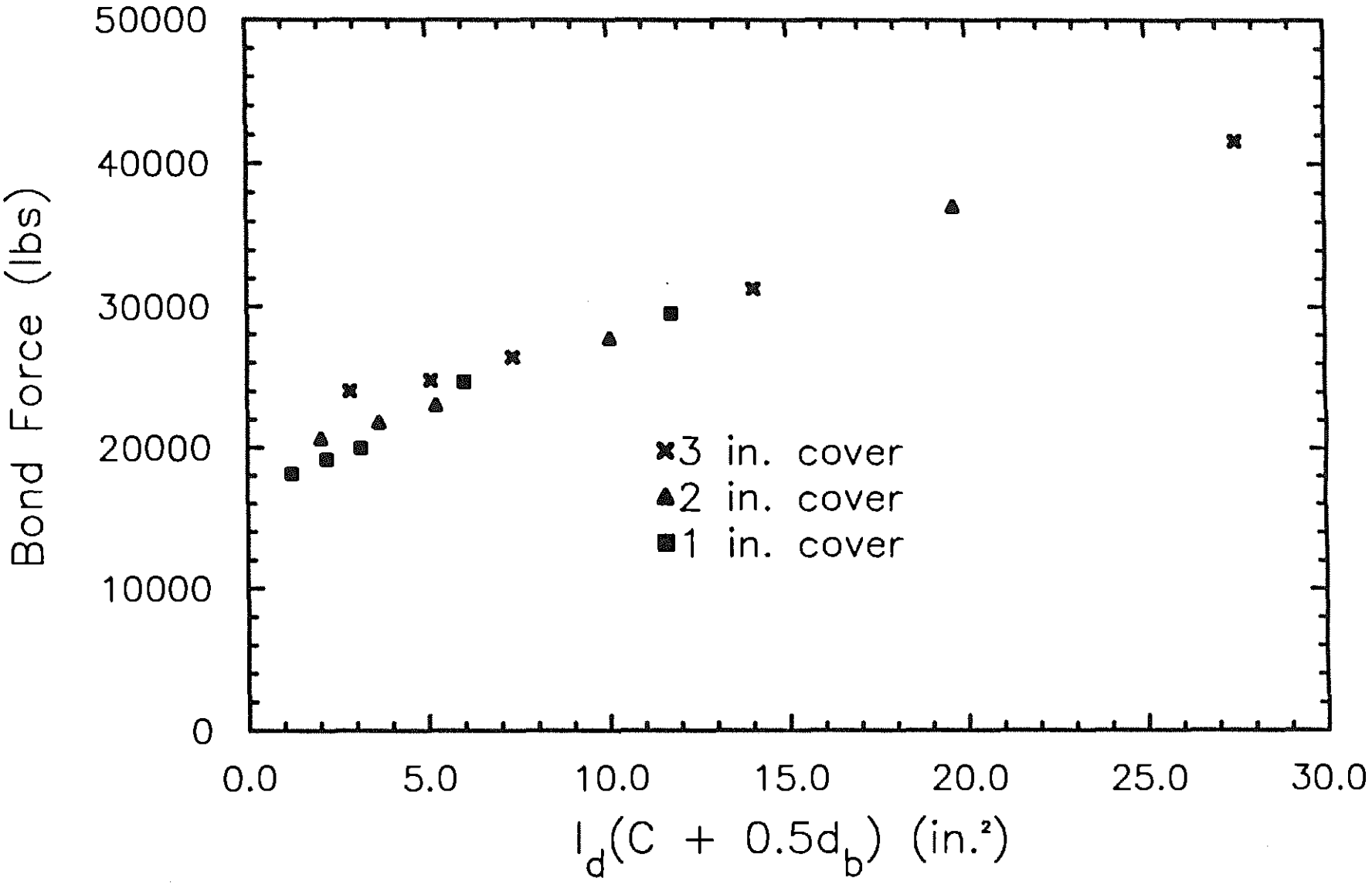

Fig. 3.27 Bond Force versus $l_d(C + 0.5d_b)$ for Models with 1/2 in. Lead Lengths (45° Ribs, Rib Height = 0.06 in.)

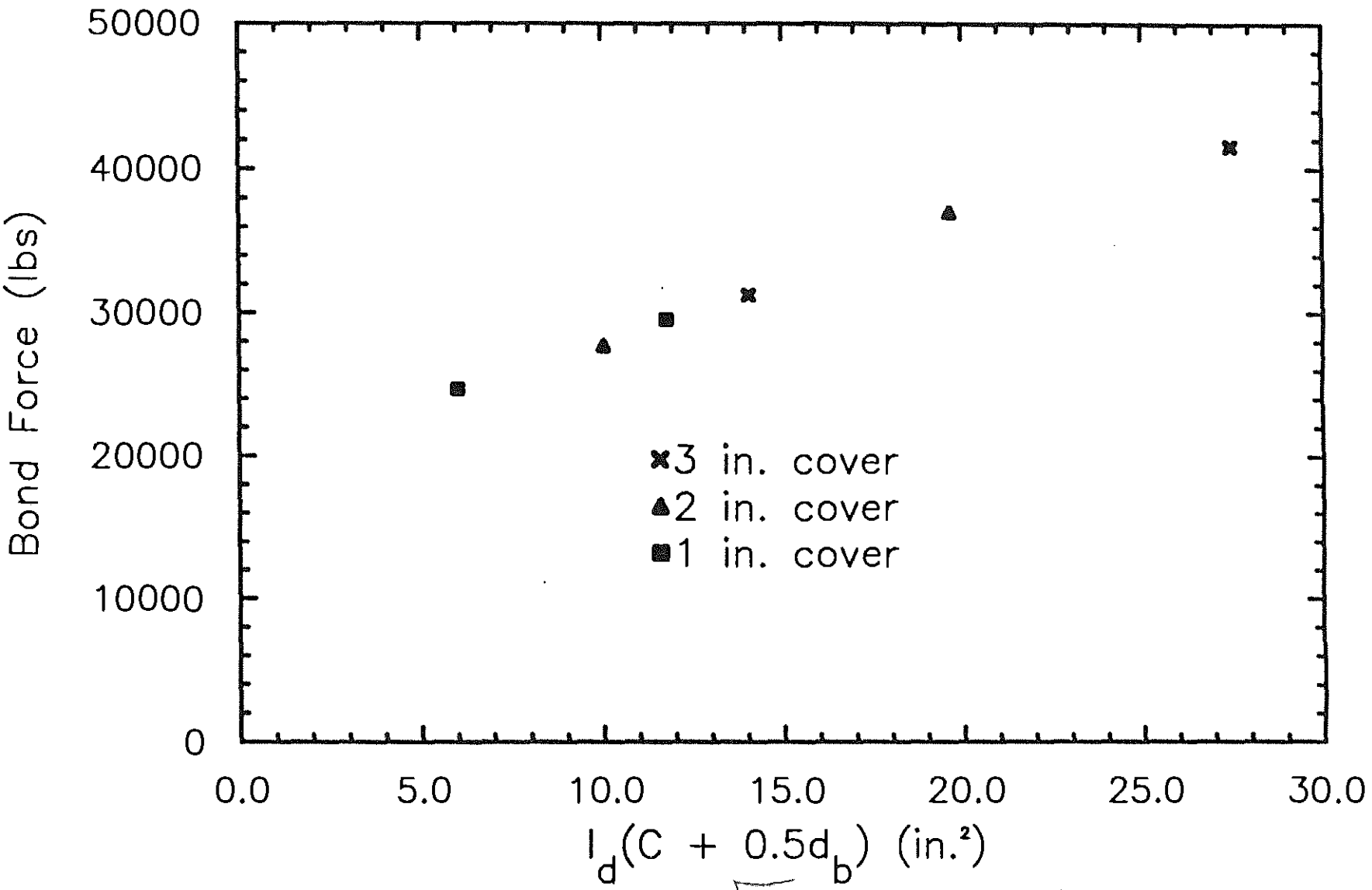

Fig. 3.28 Bond Force versus $l_d(C + 0.5d_b)$ for models with 6 and 12 Ribs (1/2 in. Lead Lengths, 45° Ribs, Rib Height = 0.06 in.)

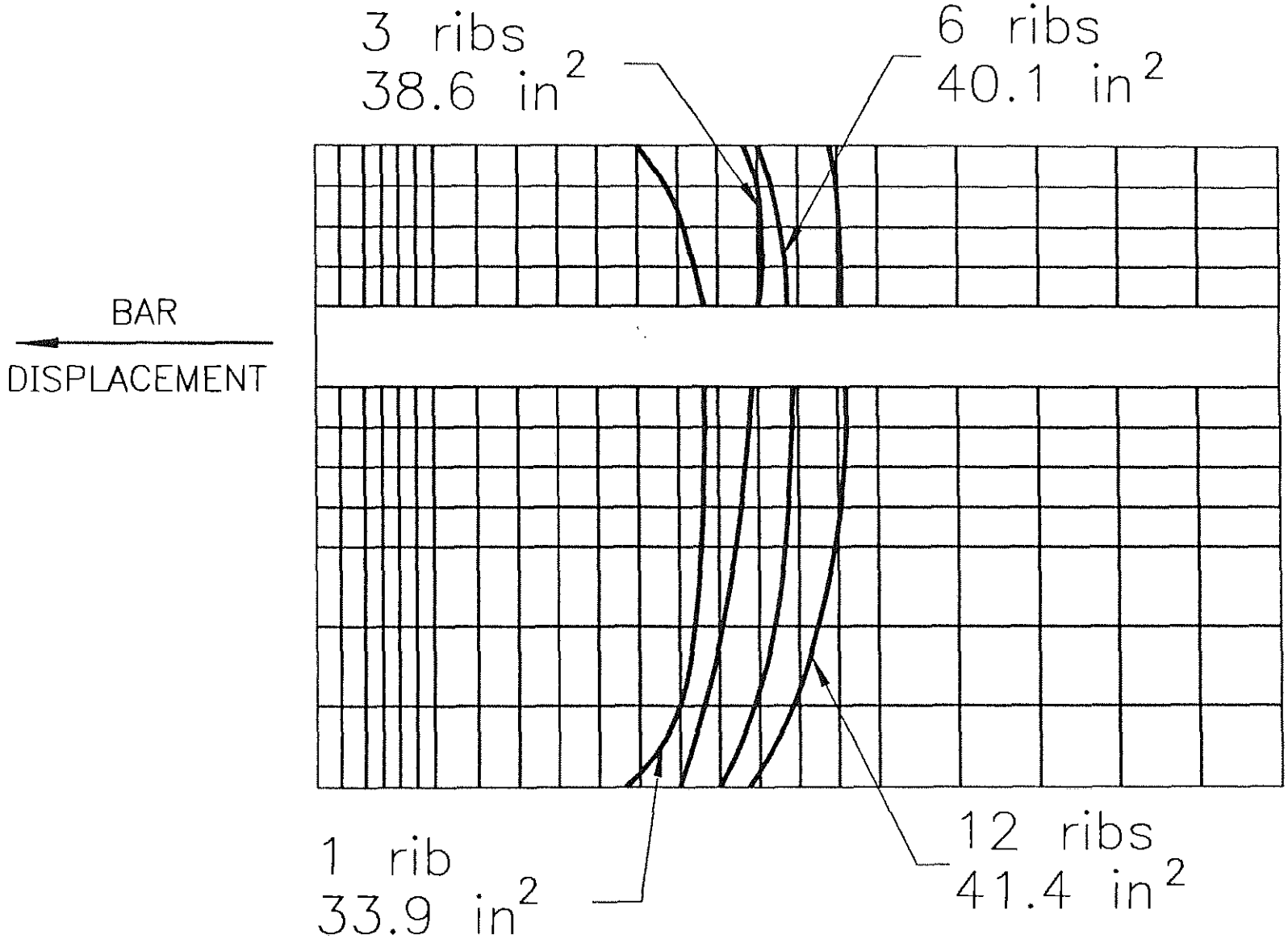

Fig. 3.29 Amount of Split Concrete for Models with 1, 3, 6, and 12 Ribs (Lead Length = 1/2 in., Rib Height = 0.06 in., Cover = 2.0 in.)

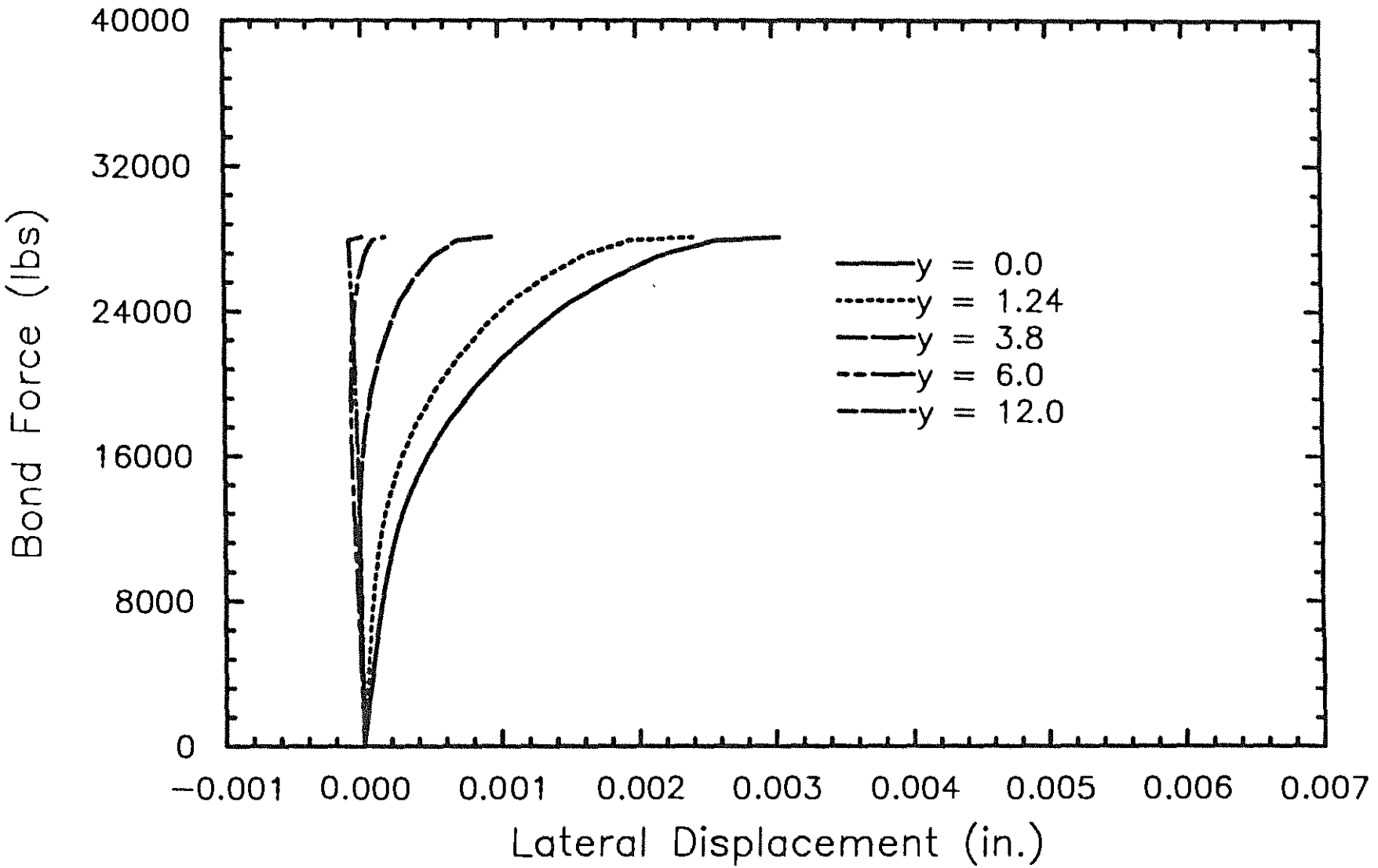

Fig. 3.30 Bond Force-Lateral Displacement Curves at Locations Along Length of Specimen for Model with 6 ribs, 2 in. cover, 1/2 in. lead length, 0.09 in. rib height (y is measured from front face of specimen)

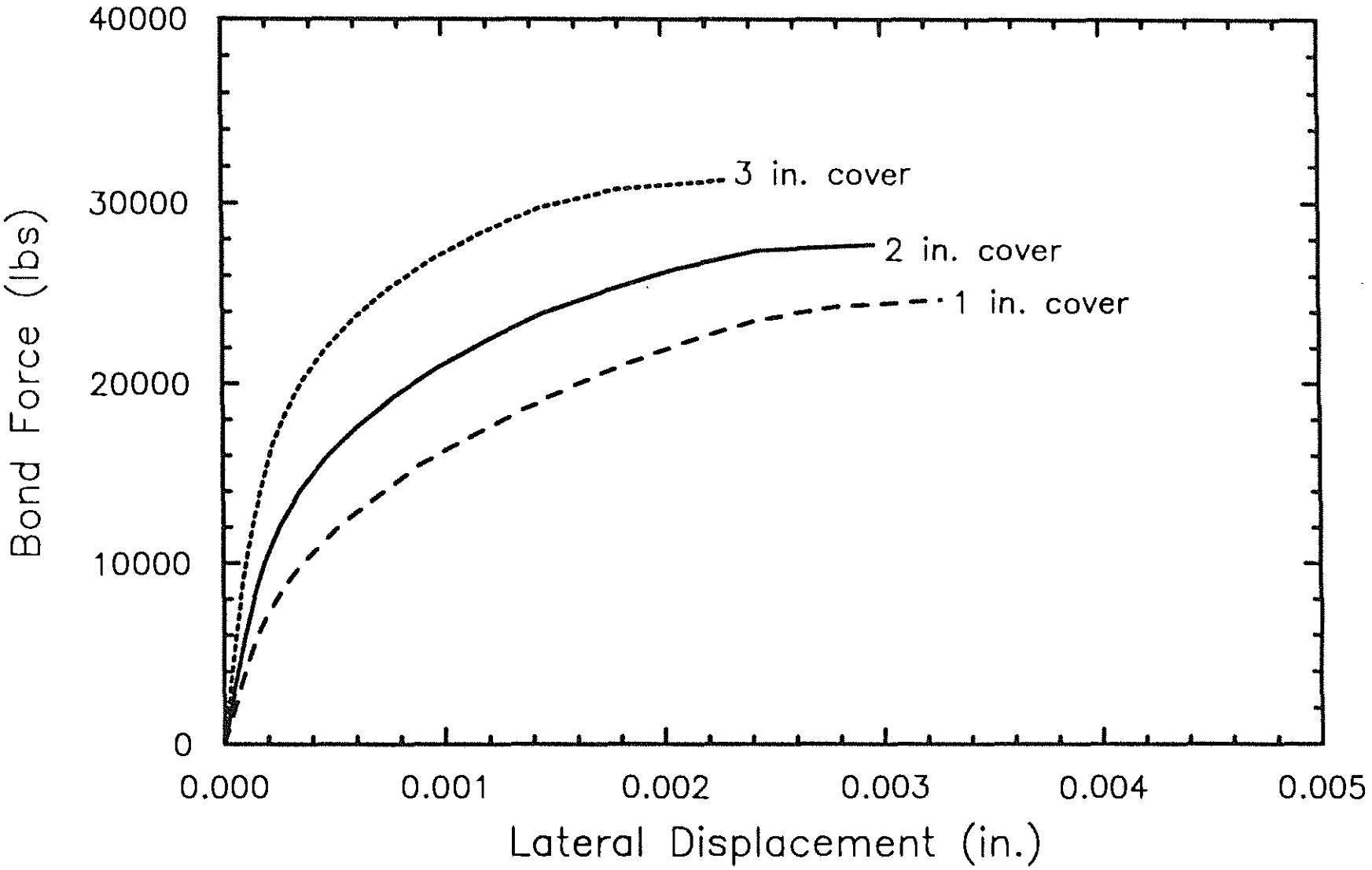

Fig. 3.31 Bond Force-Lateral Displacement Curves at Front Face of Model for 6 Rib Models with 1, 2, and 3 in. Covers (1/2 in. Lead Length, Rib Height = 0.06 in., 45° ribs)

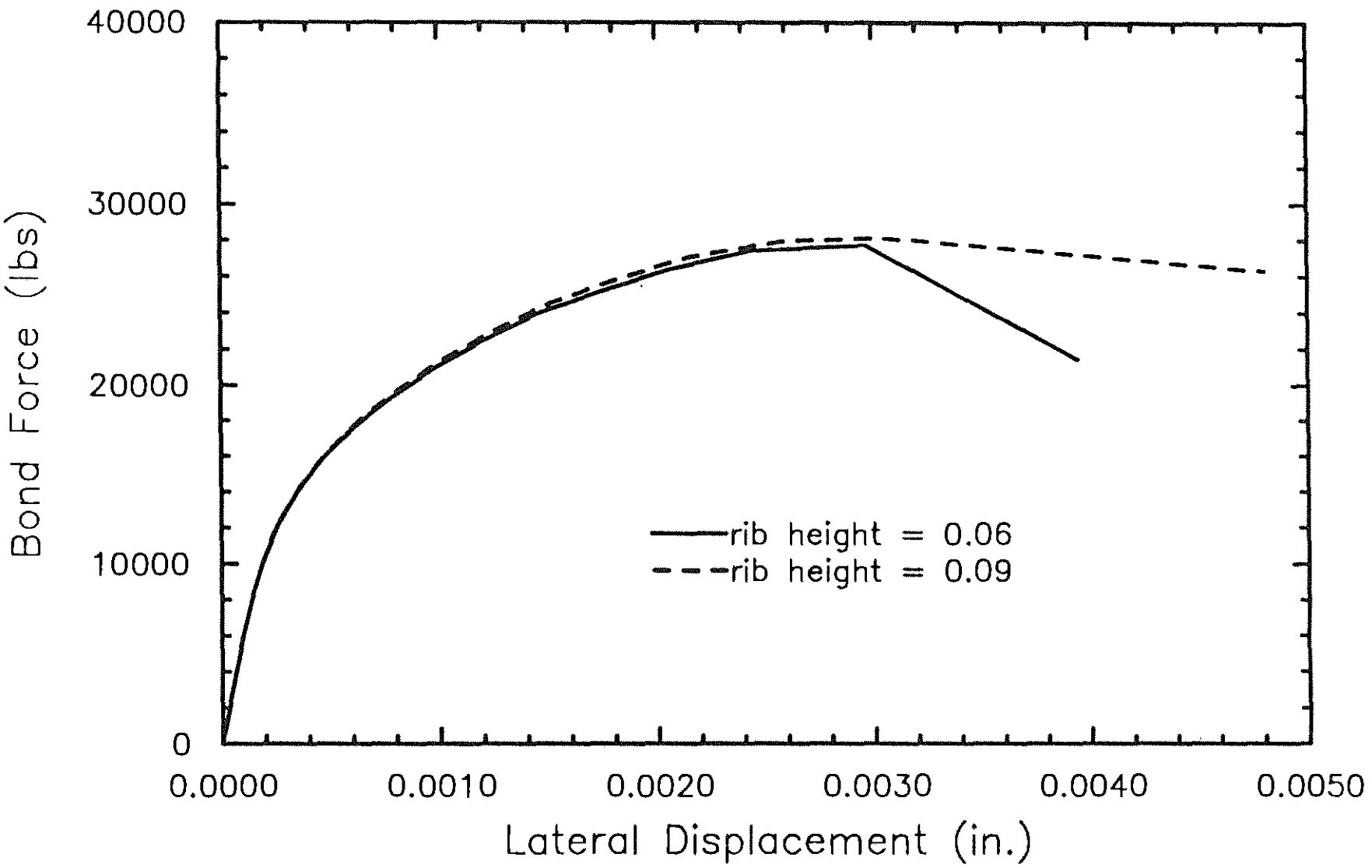

Fig. 3.32 Bond Force-Lateral Displacement Curves for Models with Rib Heights of 0.06 in. and 0.09 in. (6 ribs, 2 in. Cover)

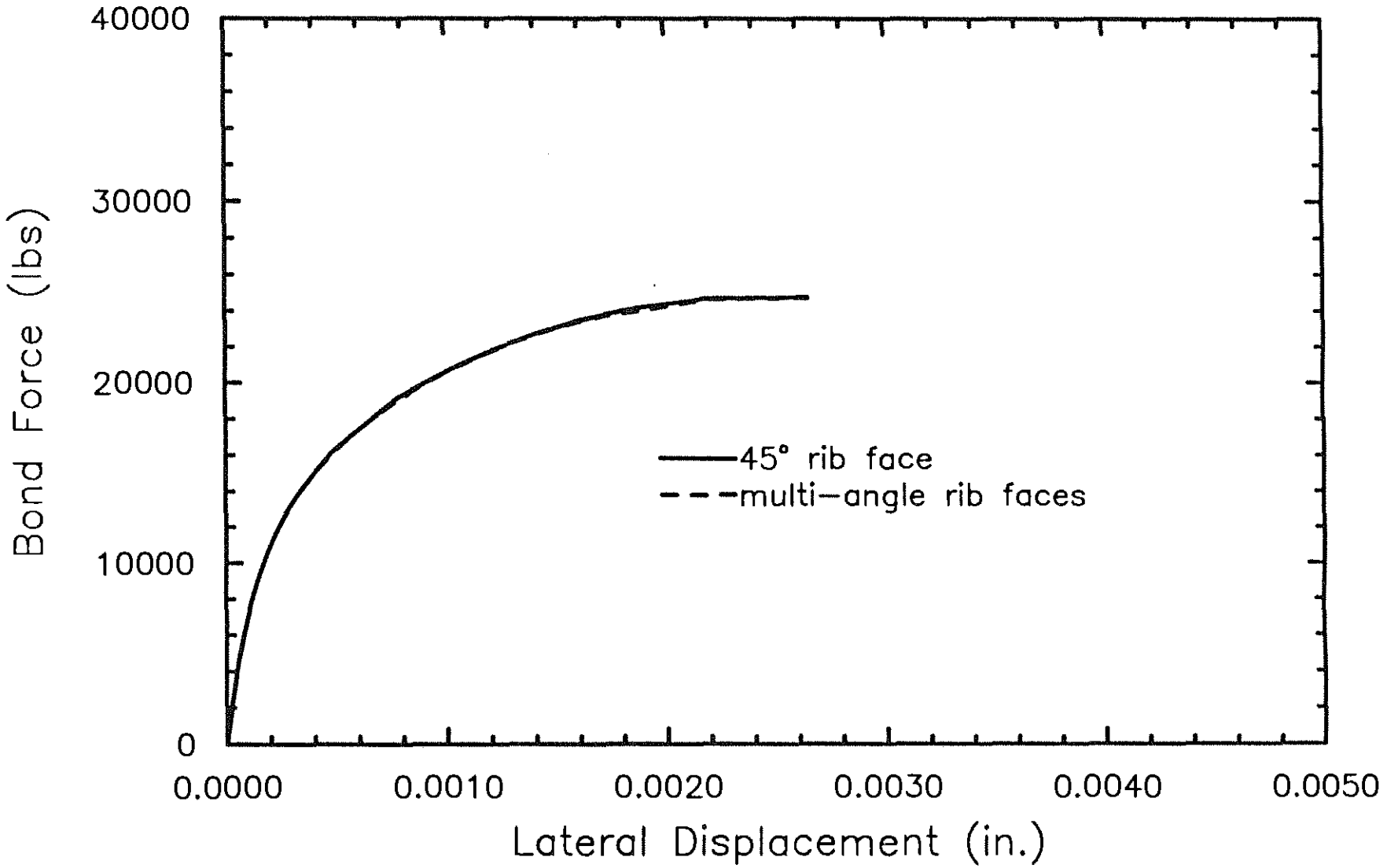

Fig. 3.33 Bond Force-Lateral Displacement Curves for Models with Multi-Angle Rib Faces and 45° Angle Rib Faces (2 ribs, 3 in. Cover)

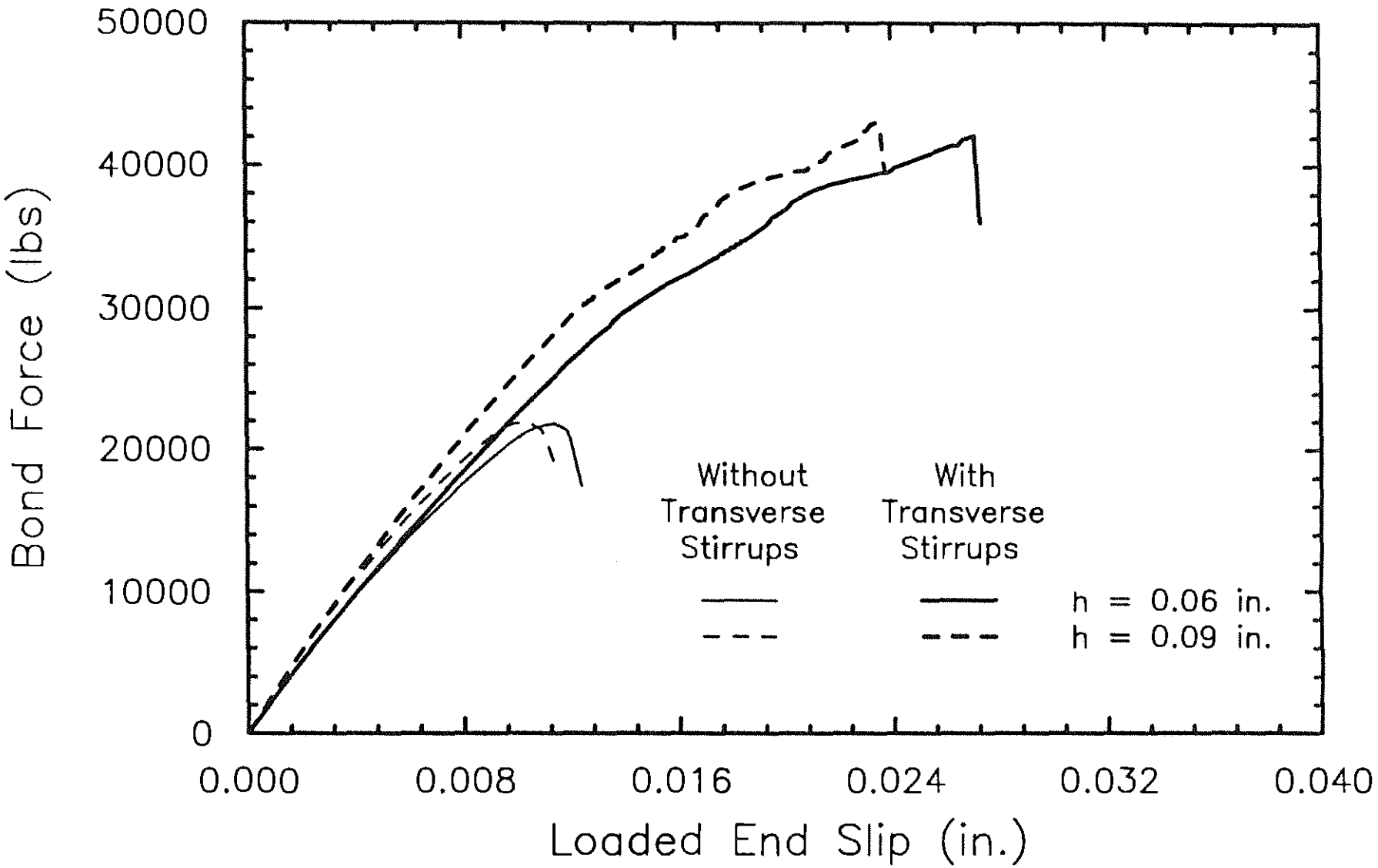

Fig. 3.34 Bond Force-Loaded End Slip Curves for 2 Rib Models With and Without Transverse Stirrups (45° Ribs, Rib Heights of 0.06 in. and 0.09 in., 2 in. Cover, 1/2 in. Lead Length)

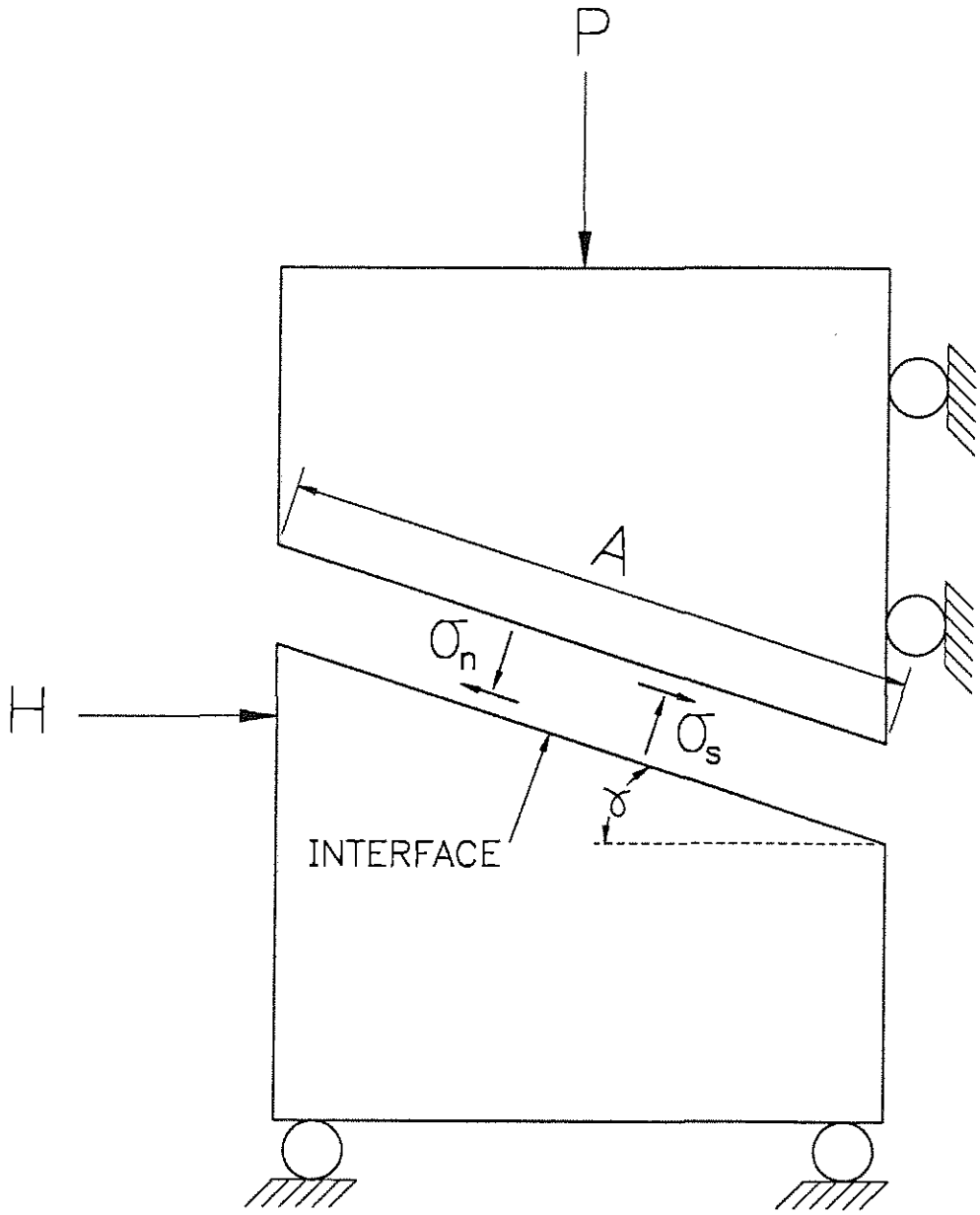

Fig 3.35 Statical Model (after Choi et al. 1990)